2020

PHYSICAL MODELING OF THE KRAUKLIS WAVES: INSIGHTS FROM TWO EXPERIMENTAL APPARATUSES

Haitao Cao
Michigan Technological University, haitaoc@mtu.edu

Recommended Citation
Cao, Haitao, "PHYSICAL MODELING OF THE KRAUKLIS WAVES: INSIGHTS FROM TWO EXPERIMENTAL APPARATUSES", Open Access Dissertation, Michigan Technological University, 2020.
https://digitalcommons.mtu.edu/etdr/1089

PHYSICAL MODELING OF THE KRAUKLIS WAVES: INSIGHTS FROM TWO EXPERIMENTAL APPARATUSES

By

Haitao Cao

A DISSERTATION

Submitted in partial fulfillment of the requirements for the degree of

DOCTOR OF PHILOSOPHY

In Geophysics

MICHIGAN TECHNOLOGICAL UNIVERSITY

2020

This dissertation has been approved in partial fulfillment of the requirements for the Degree of DOCTOR OF PHILOSOPHY in Geophysics.

Department of Geological and Mining Engineering and Sciences

Dissertation Advisor: *Roohollah Askari*

Committee Member: *Wayne D. Pennington*
Committee Member: *Gregory P. Waite*
Committee Member: *Vijaya V.N. Sriram Malladi*
Committee Member: *Seiji Nakagawa*
Department Chair: *Aleksey Smirnov*

Table of Contents

List of figures v

List of tables xi

Preface xii

Acknowledgements xiii

Abstract xv

1 Introduction 1

- 1.1 The background and motivation 1
- 1.2 Experimental studies 5

2 Experimental observation of Fluid-Filled Fractures Using the Dynamic Photoelasticity Technique 8

- 2.1 Abstract 8
- 2.2 Introduction 8
- 2.3 Method 12
  - 2.3.1 Dynamic photoelasticity technique 12
  - 2.3.2 Trilayer model 15
- 2.4 Experiments 17
- 2.5 Results 20
- 2.6 Repeatability 31
- 2.7 Discussion 32
- 2.8 Conclusion 37
- 2.9 Reference 37

3 Effect of Geometry and Fluid Viscosity on Dynamics of Fluid-Filled Cracks: Insights from Analogue Experimental Observations 42

- 3.1 Abstract 42
- 3.2 Plain Language Summary 42
- 3.3 Introduction 43
- 3.4 Method 46
  - 3.4.1 Experimental Setup 46
  - 3.4.2 Analogue Fracture – Trilayer Model 47

- 3.5 Experimental Results 50
- 3.6 Discussion 59
- 3.7 Conclusion 61
- 3.8 Acknowledgements and Data 62
- 3.9 Reference 63

4 Laboratory Measurements of the Impact of Fracture and Fluid Properties on the Propagation of Krauklis Waves 68

- 4.1 Abstract 68
- 4.2 Introduction 69
- 4.3 Method 72
  - 4.3.1 Experimental Setup 72
  - 4.3.2 Processing 75
  - 4.3.3 Boundary Conditions 76
- 4.4 Experimental Results 76
  - 4.4.1 Crack Stiffness (Thickness) 76
    - 4.4.1.1 Phase velocity 76
    - 4.4.1.2 Resonant frequencies 80
    - 4.4.1.3 Quality factor 85
  - 4.4.2 Viscous fluid 87
  - 4.4.3 Crack roughness and geometry 90
  - 4.4.4 Fracture compliance 95
- 4.5 Discussion 100
  - 4.5.1 Open-end fracture 100
  - 4.5.2 Closed-end fracture 101
  - 4.5.3 Application 103
- 4.6 Conclusion 104
- 4.7 Reference 105

5 Conclusion 109

List of figures

Figure 1-1. Standard crack model. L is the length, W width, d aperture, and α P-wave velocities in the matrix and fluid respectively, and ρ_s and ρ_s the matrix and fluid density respectively.........3

Figure 2-1. Schematic diagram of our optical apparatus. The specimen is placed between two L-shaped steel support brackets mounted on an optical table. The focal lengths *f* of each lens and diameters Ø of each optical component are indicated. σ_1 and σ_2 are two principal stresses of the sample. Details of the lenses are shown in Table 2-1. 13

Figure 2-2. The (a) Transparent trilayer held by aluminum plate. (b) and (c) Cross-length and width views of the trilayer. (d) Flat smooth fracture model in the middle layer. (e) Saw-tooth fracture model with enlarged saw-tooth geometry details. In (d) and (e), the circles along the edges of the plates are the locations of screws. The pressure pulse is initiated by striking a hammer to the aluminum piston with a rubber O-ring in a bronze tube. (a) (c) and (d) are the view in *xy* plane. The area in the red rectangular are the locations of images to be analyzed.........15

Figure 2-3**.** An example of a photoelastic image from the flat fracture filled with water. Two bright zones (superimpositions of fringes) are noticeable, highlighted by the box. These fringes indicate deformation associated with the Krauklis wave as it travelled along both solid-fluid interfaces from the source out of the image to the right. The points shown as bright squares are "receiver" locations at which we recorded the temporal stress field (waveform) by tracking the pixel values at one point using an image sequence. The overall image length (width) is about 5.715 cm (2.85 cm) and contains 512 pixels (256 pixels) in each dimension for a pixel size of 0.112 mm. 19

Figure 2-4**.** Pseudo-color photoelastic images of Experiment 1 (flat fracture filled with water), shown every 0.1 ms. The white dashed lines correspond to the areas with the maximum stress of the Krauklis wave. The color bar shows the pixel intensity value. 21

Figure 2-5. Pseudo-color photoelastic images of Experiment 2 (flat fracture filled with viscous shampoo). The stress is more concentrated along the fracture boundary than in Experiment 1. Some residual stress is noticeable at the lower part of the fracture that may be due to some experimental weakness: (i) inadequate or over-tightening of screws or (ii) manufacturing flaws in the fracture model. In spite of that residual stress, the propagation of the Krauklis wave is clearly defined.........22

Figure 2-6**.** Pseudo-color photoelastic images of Experiment 3 (saw-tooth fracture filled with shampoo). The red dashed lines correspond to the maximum stress field initiated by the Krauklis waves. Due to the residual stress (either from screwing or manufacturing) at the bottom of the frames, the identification of the stress field of the Krauklis wave at the lower part of the specimen is difficult. Internal reflections of the Krauklis wave are noticeable that cause perturbation in the stress field. It is clear that the wave is strongly disrupted by the saw-tooth nature of the fracture boundary. 23

Figure 2-7**.** The temporal stress field of the Krauklis wave of Experiments 1, 2, and 3, in (a), (b) and (c), respectively. The waveforms of Experiments 1 and 2 are obtained from the seven fixed points indicated in Figure 3 whereas those of Experiment 3 are from the six tooth of the saw-tooth fracture. The dashed arrow follows the maximum stress field of the Krauklis wave from which we estimate the group velocity. Comparing the first and last traces, we note that the duration of signals increases as the Krauklis wave travels, implying that the high frequencies are significantly attenuated. 24

Figure 2-8. The amplitude spectra of the first and last traces of the temporal stress fields of Experiments 1, 2, and 3, shown in (a), (b), and (c), respectively, from the traces in Figures 7a-c. As the Krauklis wave travels, the high frequencies are attenuated. The Krauklis wave from Experiment 1 (a) is richer in high frequencies than Experiments 2 and 3, due to the lower viscosity of water (Experiment 1). Note that the data from Experiment 3 (shampoo in saw-tooth fracture, shown in c) contains higher frequencies (> 1000 Hz) than present in Experiment 2 (shampoo in flat fracture, shown in b), which likely implies the effect of the large-scale geometric heterogeneities. 25

Figure 2-9. Dispersion curves extracted by high-resolution linear Radon transform for Experiments 1, 2, and 3 in (a), (b), and (c), respectively. The black markers represent the picked dispersion curves. The poor resolution at frequencies below 500 Hz is due to the short length of the array over which the dispersion analysis is conducted. In addition, we note that the dispersion curve is not continuous in (c) due to the large-scale perturbation of the stress field in Experiment 3. Due to the lack of high frequencies in Experiment 2 (see Figure 9b), no velocity trend at frequencies higher than 900 Hz was obtained for that experiment.......................27

Figure 2-10**.** Spectral decomposition of the waveforms from Experiment 3 as shown in Figure 7c. The dashed lines correspond to the general trend of the stress field of the Krauklis waves. We note that high frequencies arrive earlier, which is consistent with the theory. Some perturbation has been highlighted by arrows. The first three traces show that the high-frequency contents attenuate faster than the low frequency contents. 29

Figure 2-11**.** The dispersion curve of the Krauklis wave for the three experiments. Note that the flat water filled fracture has the highest velocity. The velocity significantly increased in the saw-tooth fracture filled with shampoo (Experiment 3 compared to

Experiment 2), which implies the possible effect of the geometry on the dispersion of the Krauklis wave. 30

Figure 2-12**.** The photoelastic images of a manually repeated Experiment 1 (flat fracture filled with water). The white dashed lines correspond to the areas with the maximum stress of the Krauklis wave. 31

Figure 2-13**.** (a) The temporal waveform of the Krauklis wave of the repeated Experiment 1. The dashed arrow shows the maximum stress field of the Krauklis wave of the image sequence. (b) The dispersion curve extracted by high-resolution linear Radon transform for the repeated Experiment 1. 32

Figure 3-1. Four stages of cavity collapse in a dike. (a) The magma pushes the rock at the tip of the dike. (b) Once the rock is opened, a pressure pulse drop is initiated at the tip and travels down through the dike. The pressure drop creates small cavity bubbles within the dike. (c) The bubbles continue to grow until reaching their maximum sizes, and (d) They collapse quickly, and shock waves are created. 44

Figure 3-2. Schematic diagram of the combined high-speed shadowgraph imaging system and linear polarizer setup. The specimen is placed between two steel L-shaped support brackets that are mounted on an optical table. Ø is the lens diameter and *f* the focal length. σ_1 and σ_2 are principal stresses of the sample. 46

Figure 3-3. (a) The trilayer model and its schematic side view, which consists of one polycarbonate and two acrylic plates, fastened by two aluminum plates. The pressure pulse is produced by applying a sudden load to the aluminum piston. (b) Flat fracture model in the middle layer used as a reference. (c) Saw-tooth fracture model and enlarged details of its geometry. The circles along the edges of plates are the locations for clamping bolts. 49

Figure 3-4. The fracture models used to study the fluid-filled fracture dynamics in the plastic zone. (a) Single narrow tip with 1 cm length and 2 mm width. (b) Double narrow tips with 1 cm length and 2 mm width each. (c) Triangle tip with 1 cm side length. In fracture propagation linear elasticity is valid far from the tip, it breaks down near the tip, where one has a highly nonlinear plastic zone........................50

Figure 3-5. The photoelastic image of the reference smooth flat fracture used to show the solid-fluid interaction due to the input pressure pulse on the liquid phase under no surface irregularities. The bright dashed line trend represents direction of the stress wave propagation, which is the result of the photoelastic effect on the polycarbonate layer. The bright patterns near the crack tip are due to the residual stress, caused by clamping bolts. The color bar shows the pixel intensity value of the images. Stressed area is in white and unstress is in black. 51

Figure 3-6. Image sequence of the bubbles expansion and collapse for the saw-tooth fracture model. (a) Before the bubble initiation, there is no stress on the saw-tooth.

(b-f) As the pressure on the liquid decreases, the small-scale bubbles expand and photoelastic fringes (bright patterns) appear on the fracture surface, implying that the fracture surface is subjected to a tensile stress due to the bubble expansion. (g) The photoelastic fringes and the associated stress on the fracture surface disappear after the pressure in the fluid recovered. (h) The tracked pixel brightness intensity at the saw-tooth location indicated by white arrow in (a-g). This cavitation phenomenon was not observed in the reference fracture in Figure 3-5. 53

Figure 3-7. The photoelastic images of the stress wave propagation in the saw-tooth fracture filled with shampoo. The bright dashed line trend represents direction of the stress wave propagation as in Figure 3-5. Cavitation phenomenon is not observed in this shampoo filled fracture. 55

Figure 3-8. The image sequences the process of bubbles emergence at the fracture tip. These narrow fracture tips were purposely not filled with water to mimic trapped bubbles. The pressure wave in the fluid phase forces the bubble to intrude into the tip, forcing a delamination of the layers of the trilayer model..............................57

Figure 4-1. Trilayer aluminum model. (a) A and B upper and lower plates respectively. The red box indicates the receiver locations respectively. (b) Trilayer from the cross. The crack model is created by placing washers between the two plates. 73

Figure 4-2. Schematic diagram of the data acquisition system. A pressure pulse from source is transmitted to the crack through the conduit on the left side of the model. The receiver acquires data and moves along the plate to obtain the seismic array.......74

Figure 4-3. The source waveform and its amplitude spectra. The single sin-modulated input pulse of a 1000Hz dominant frequency is measured from the source by attaching the receiver to the source. 74

Figure 4-4. a-d the waveforms for the thicknesses of 1.5, 2.5, 4.5 and 8.5 mm, corresponding to crack stiffnesses of 17, 10, 6, and 3 respectively. For each of the fracture models, the first three modes of resonant frequencies can be identified and indicated by the red number. The red arrow follows the propagation direction and is not intended to track any specific arrival. 78

Figure 4-5. The phase velocity of the waveforms in Figure 4-4 for the crack thickness of (a) 1.5, (b) 2.5, (c) 4.5, and (d) 8.5mm. The white-cross markers are the picked values and the black dashed curve are theoretical fittings. 79

Figure 4-6. The overlay plot of the picked dispersion curves for different fracture thickness in Figure 4-5...79

Figure 4-7. The normalized amplitude spectra of the waveforms in Figure 4-4 for the crack thickness of (a) 1.5, (b) 2.5, (c) 4.5, and (d) 8.5mm. The top plot shows the mean spectra of all 15 traces. The mode numbers are indicated at peak resonant frequencies. (d) The high amplitude marked by the red circle represents the antinode pressure. Higher mode resonance shows more antinodes. 82

Figure 4-8. The frequency-wavelength relation calculated from the dispersion curve in Figure 4-5 (c) for the crack of 4.5mm thickness. The red circles indicate the first three modes with frequency and corresponding wavelength in parentheses. The first two modes are not observed in the 2D resonance map in Figure 4-7. 84

Figure 4-9. 4 traces at the trace 8 from the crack thickness of (a) 1.5, (b) 2.5, (c) 4.5, and (d) 8.5mm. The fracture thickness increases, the amplitude of Krauklis wave signal becomes weak. 85

Figure 4-10. The quality factor for the crack thickness of (a) 1.5, (b) 2.5, (c) 4.5, and (d) 8.5mm at trace 8. As the stiffness decreases (thickness increases), the quality factor increases. 86

Figure 4-11. (a) The waveform array of acquired from the fracture filled with viscous oil. (b)The entire waveform of trace 5 comparison from water and oil-filled fracture of 4.5mm thickness fracture. 87

Figure 4-12. The properties of Krauklis waves in oil-filled fracture of 4.5 mm thickness. (a) The 2D map of resonance frequency (b) quality factor (c) phase velocity and (d) Comparison of the Krauklis wave phase velocity in the water−filled and oil−filled fracture of thickness 4.5 mm. All of these values in oil−filled fracture are lower than that in water. 89

Figure 4-13. The fracture roughness model and the wedge shape model in (a) and (b)....90

Figure 4-14. (a) and (b) The waveforms of the Krauklis wave of the rough and wedge fracture models. The red arrows follow the trend of the Krauklis wave propagation. 91

Figure 4-15. The phase velocity of crack wave from fracture roughness model and the wedge shape model in (a) and (b). The dashed black curve is the theoretical crack wave velocity for flat crack using the average thickness of the top and bottom plate 1.05 mm. 92

Figure 4-16. The resonance frequencies of crack wave from fracture roughness model and the wedge shape model in (a) and (b). 92

Figure 4-17. The quality factors obtained for the roughness model at (a) trace 2, (b) trace 8 and (c) trace 12...94

Figure 4-18. The quality factors obtained for the wedge model at (a) trace 2, (b) trace 8 and (c) trace 12. 95

Figure 4-19. Comparison of the resonant frequencies and phase velocity of fractures with different compliance. (a) and (b) are the resonant frequency map and phase velocity of fracture supported by two springs; (b) and (c) by 8 springs; (e) and (f) by 16 springs. The resonant frequencies and phase velocity increased with decreasing compliance. The white crossing markers are the picked dispersion curve to follow the HRLRT calculated trend. 98

Figure 4-20. The quality factors obtained from complaint fractures embedded with springs. (a) fracture with 4 springs. (b) fracture with 8 springs. (c) fracture with 16 springs 99

Figure 4-21. The overlay plot of the picked dispersion curves of Krauklis waves for cracks with different fracture compliance in Figure 4-19. 100

Figure 4-22. The pressure vibration of Krauklis waves in open-end fracture. (a) to (f) represent the fundamental mode to mode 6, respectively. The red points represent the antinodes at the maximum pressure. 101

Figure 4-23. Krauklis waves properties in the closed-end fracture. (a) the 2D seismic array. (b) the resonant frequencies. The red arrows are pointing at different modes. (c) The phase velocity. 102

Figure 4-24. The resonance frequencies and quality factors calculated using Sompi method. The first observed resonant frequency 725 Hz and its corresponding quality factor 50 are used to calculate the fracture length using equation 6. 104

List of tables

Table 2-1. Parameters of the optical components 14

Table 2-2. The physical parameters of the solid medium of the trilayer. 16

Table 2-3. Experiments and major observations. 18

Table 3-1. Six Experiments to Visualize the Fluid-Filled Fracture Dynamics 47

Table 4-1. Physical properties of the aluminum plate. 73

Table 4-2. Theoretical resonance frequencies estimated from cracks with different thicknesses. 81

Table 4-3. Experimental Resonance frequencies from cracks with different thickness. ... 83

Table 4-4. Experimental and theoretical resonance frequencies ratio from cracks with different thickness. 84

Table 4-6. The physical parameters of the conical compression spring. 96

Table 4-7**.** Resonant frequencies of cracks with different compliance 100

Table 4-8. Input parameters for equation 6 to calculate the fracture length. 104

Table 4-9. Experiments in the paper. 105

Preface

Chapter 2. “Experimental observation of Fluid-Filled Fractures Using the Dynamic Photoelasticity Technique” was submitted on 15-Auguest, 2019 to *Geophysics*. As of this writing, it is in the state of minor revision. In this chapter Ezequiel Medici, Haitao Cao and Roohollah Askari contributed to the conception and design of this work. Ezequiel Medici and Haitao Cao carried out the experiment. Haitao Cao wrote the first draft of the manuscript, performed initial data processing for the stress wave images, statistical analysis, and phase velocity extraction. Roohollah Askari and Ezequiel Medici supervised all work, advised Haitao Cao on data processing methods and provided revisions for the manuscript. All authors read and approved the submitted manuscript.

Chapter 3. “Effect of Geometry and Fluid Viscosity on Dynamics of Fluid-Filled Cracks: Insights from Analogue Experimental Observations” was submitted on 02-July 2020 to *Earth and Space Science*. Ezequiel Medici, Haitao Cao and Roohollah Askari contributed to the conception and design of this work. Ezequiel Medici and Haitao Cao carried out the experiment. Haitao Cao wrote the first draft of the manuscript. Gregory Waite strengthen the discussion and provide the implication on the observed experiment result. Roohollah Askari and Ezequiel Medici and Gregory Waite provided revisions for the manuscript. All authors read and approved the submitted manuscript.

Chapter 4. “Laboratory Measurements of the Impact of Fracture and Fluid Properties on the Propagation of Krauklis Waves” is in preparation for submission to the *Journal of Geophysical Research: Solid Earth*. The chapter was written by Haitao Cao under the supervision of Seiji Nakagawa and Roohollah Askari.

Acknowledgements

I am extremely grateful to my advisor Dr. Radwin Askari for his dedicated support and encouragement during my Ph.D. study and research. Whenever I get stuck in research, he always sharing me his experience and help me get out of a rut. His guidance helped me at various stages of research and writing of this thesis. I have been lucky to have a supervisor who cared so much about my work, and who responded to my questions and queries so promptly.

Besides my advisor, I would like to express my deepest appreciation to my committee: Dr. Wayne Pennington for providing me continuous insightful suggestions and encouragement since I was working on my M.S. in Michigan Tech six year ago. Given his busy schedule as a Dean, he is always available to offer help to any of his students. He is the role model that I want to be. I am also very grateful to Dr. Gregory Waite for his scientific advice and many insightful discussions and suggestions. I cannot forget that many of the senior graduate students in our department recommend me to take the most handsome professor's class Earthquake and Seismology.

I am deeply indebted to Dr. Seiji Nakagawa for his help in providing advice many times in this research. Without his help I will be still wandering in the mist. I am very grateful for him providing me the opportunity to visit his lab in the Berkeley and spent the entire afternoon to taking me the laboratory tour and answered my questions. I learnt from him to think more independently about my experiments and results. My thank also goes to Dr. Sriram Malladi for serving as my defense committee. I would also like to extend my deepest gratitude to Dr. Ezequiel Medici for his excellent guidance and collaboration in the optical experiment design and operation, from whom I learnt most of my experiment skills.

I thank Roger Turpening for his acoustic lab instruments support and providing the weekly delicious bakery dessert in SPOT-lab and Scott Wagner for his help in the lab instrument technical support. Thank you to Kelly McLean, Carol Asiala, and Brittany Buschell in our department for taking car the numerous paperwork and documents since I came to MTU.

I would like to express my sincere gratitude to the graduate school for awarding me the Doctoral Finishing fellowship for the summer 2020 to finish writing my dissertation.

Last but most important, I would like to thank my family for their continuous encouragement and support. Words cannot express how grateful I am to my older brother, my mother, my father for all of the sacrifices that you've made on my behalf.

Abstract

Fractures play an important role in the geological related processes such as hydraulic fracturing, water-water disposal, and volcanic earthquake. Seismic waves can provide useful information from fractures at a relatively low cost. In particular, the acoustic property of fractures containing magmatic or hydrothermal fluids can provide useful information about the fracture size and the fluid composition within the fracture. For instance, in volcanology, the resonant frequency of long-period events that are linked to crack interface waves is used to obtain fluid properties of cracks in magmatic systems. However, in order to rely on seismic data, they should be precisely characterized in advance. Experimental studies are one of the most important resources to describe and understand physical systems. They are even used to validate analytical and numerical methods. In this dissertation, I aim to gain more insight into the crack waves that are slow guided waves in fluid-filled fractures and are characterized by their dispersive and resonating nature. We will develop two experimental setups. Using the first apparatus that employs the photoelasticity technique, we will visualize the stress regime of the fracture due to the motion, transmission, and reflection pattern of the crack wave. Using the second apparatus which is an acoustic data acquisition system, we extend the fracture of two parallel plates to a more complex and realistic fracture by modifying the fracture stiffness, saturated fluid and fracture geometry, and fracture surface roughness. We evaluate the dispersion and resonance properties of the crack waves under different environments. In addition, some present analytical and numerical models will be evaluated.

1 Introduction

1.1 The background and motivation

Fractures have a significant influence on the seismic signature of the reflected and transmitted seismic wave and fluid-filled cracks can serve as seismic sources. The complex geometry of fractures can govern the physical properties such as elastic wave velocity, seismic anisotropy, and permeability of formations. Pressure disturbances in a fluid-filled fractures can create a low frequency seismic wave that is called the crack wave (Chouet, 1985). The crack wave is highly dispersed with a low velocity that is much lower than the sound speed in the fluid in the fractures (Krauklis, 1962; Korneev, 2008; Frehner, 2014). The crack wave has back and forth movements and cause the fracture to behave as a resonating source whose signature is recorded as long period (LP) events (Ferrazzini and Aki, 1987; Ferrazzini et al.1990; Frehner and Schmalholz, 2010).

Tary and Van (2012) and Tary et al. (2014) identified the resonance characteristics of the crack waves in fluid-filled cracks which can be used to gain a better understanding of reservoir deformation or dynamic fluid flow perturbation during fluid injection into hydrocarbon and geothermal reservoirs, CO_2 sequestration, or volcanic eruptions. Since crack waves and LP events are generated from fluid-filled fractures, they can reveal crucial information about fractures and their fluid properties (Chouet, 1986, 1988; Kumagai and Chouet, 1999; Taguchi et al., 2018). Chouet (1986, 1988) presented a finite-difference method to model the dynamics of an expanding fluid-filled crack. Chouet (1986, 1988) introduced two dimensionless parameters to characterize the crack waves and LP events. One parameter is the crack stiffness $C=(b/\mu)(L/d)$ and the other viscous damping ratio

$F=12\eta L/\alpha d^2\rho_f$, where b is the bulk modulus of the fluid, μ is the rigidity of the solid, and L and d are the crack length and crack thickness, respectively, η is the viscosity, α is the compressional wave velocity in solid, ρ_f is the fluid density. Chouet (1986, 1988) showed that the crack wave velocity decreases when the crack stiffness increases. In addition, he noted that cracks with a higher damping factors generate crack waves with lower resonant frequencies.

All the published experimental and analytical models have been based on a parallel flat and oversimplified crack as the standard model (Figure 1-1) (Paillet and White, 1982; Tang and Cheng, 1988; Hasson and Nagy, 1997; Kumagai et al., 2005; Nakano and Kumagai, 2005; Nakano et al., 2007; Maeda and Kumagai, 2013; Syahbana et al., 2014; Taguchi et al., 2018). Using this model, all properties regarding fracture size and fluid properties have been inferred from crack wave and LP events. For instance, Taguchi et al. (2018) estimated the size of crack in Kusatsu-Shirane volcano, Japan and Galeras volcano, Colombia. In addition, Taguchi et al. (2018) estimated the volume of mist and dust in those cracks. These estimates are important to understand fluid dynamics and scale of fluid transport in hydrothermal and magmatic systems. Furthermore, the crack waves can obtain important data about the tensile fracture development in the hydraulic fracturing surveys. Hu et al. (2017) developed a method to localize the source locations of LP events from hydraulic fracturing data to obtain tensile fracture development. Recently, *Seismos* that is a consulting company in Austin, TX has developed an industrial platform to characterize fractures from the crack wave data obtained from hydraulic fracturing.

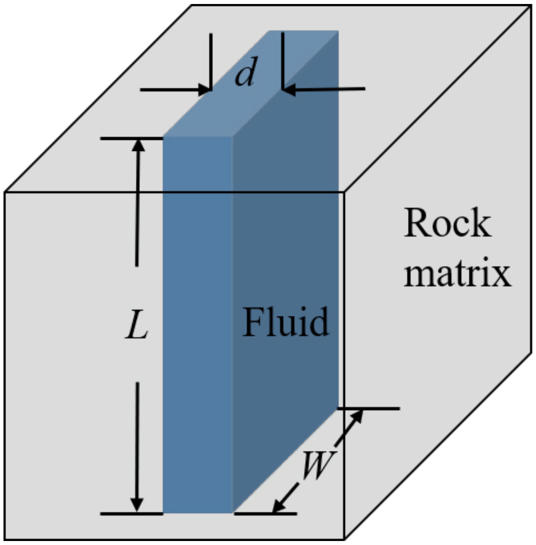

Figure 1-1. Standard crack model. L is the length, W width, d aperture, and α P-wave velocities in the matrix and fluid respectively, and ρ_s and ρ_s the matrix and fluid density respectively.

Although the effects of many parameters including crack length, aperture, and fluid viscosity have been investigated on the characteristics of the crack waves (Korneev, 2008; Kumagai and Chouet 1999, 2001; Groenenboom and Falk, 2000; Frehner and Schmalholz, 2010; Taguchi el al., 2018), to the best of my knowledge, little has been done to investigate the effect of crack geometry on crack wave properties. Real fractures have much more complex geometries in nature. For instance, fractures have roughness and are interconnected through joints. To obtain more realistic estimates about fracture size and fluid properties from crack waves, we have to consider these complexities in our numerical and analytical models. Numerical and analytical studies

Ferrazzini and Aki (1987) derived the equation of dispersion of the slow wave trapped in crack to determine the phase velocity that is inverse proportion to the wavelength. Following the pioneer works of Krauklis (1962) and Lloyd and Redwood (1965), a number of analytical studies have been conducted to characterize the crack waves in fractures with varying degrees of complexity in models. Groenenboom and Fokkema (1998) and Korneev (2008) have reported the high amplitude of the crack waves and their dominant influence on the propagation of waves in a fracture filled with fluids. Laperre and Thys (1994) investigated the elastic wave dispersion in symmetric and asymmetric systems that consist of two solids containing fluid. Coulouvrat et al. (1998) confirmed the low frequency mode that is dependent of the thickness of the fluid layer. Korneev (2008) obtains the analytical solution for phase velocity of crack waves in an infinite fracture filled with viscous fluids suggesting the possibility of differentiating between oil and water at low frequencies. In a system of multiple alternating fluid-solid layers, two waves propagate (Brekhovskikh, 1980); one is associated with the fluid layers exhibiting strong dispersion when propagating as the crack wave and the other with the solid layers that has little dispersion (Korneev, 2011). Korneev et al. (2014) used a fracture filled with a non-viscous fluid to evaluate the low frequency symmetric mode and confirmed the existence of crack in both thin and thick fracture regimes allowing us to study field-scale frequency at laboratory-scale dimensions.

In addition to analytical studies, several numerical studies have been carried out about the crack waves. Aki et al. (1977) numerically investigated the dynamics of cracks filled with fluids. By modeling the dynamic of an expanding fluid-filled crack using finite-difference method, Chouet (1986) found that the crack wave mode propagates slower than that of the acoustic velocity of the fluid. Groenenboom and Falk (2000) numerically modeled hydraulic fractures combining with laboratory data and generated the crack wave with a slow, dispersive property. Yamamoto and Kawakatsu (2008) used a simple and efficient frequency-domain boundary integral method to simulate the fluid motions in a fracture and computed both the frequency and the attenuation quality factor of the resonance for the crack. Frehner and Schmalholz (2010) studied the reflection and radiation of crack waves at the crack tip using two different geometries (elliptical and rectangular) filled with different fluids (oil, water and gas), and obtained numerical results with high resolution. Frehner (2014) showed that these waves can be initiated by the passing body waves in a fluid filled fracture. S-waves generate crack waves with higher amplitudes than those initiated from the P-wave, and the initiation strongly depends on the orientation of the fracture.

1.2 Experimental studies

Following Chouet's numerical simulation of crack wave and their associated resonance property with respect to crack stiffness and viscous damping ratio (Chouet 1986, 1988), Tang and Cheng (1988) first investigated the crack propagation in lab scale using two thick cylinder to mimic two half-space. While Hassan and Nagy (1997) used ultrasonic measurements to study crack waves over a frequency range of 15 kHz – 150 kHz in an aluminum – water – aluminum trilayer model. The results of the phase velocity variation with frequency suitably match with the theoretical prediction of the phase velocity of the crack wave. However, an estimated error ±7% was obtained which was attributed to the spurious interference that coupled the two transducers used in the experiment. Shih and Frehner (2015) observed the resonance effect of the crack wave in their experimental study and verified the laboratory results using an analytical solution. They also found that S-waves can initiate the crack waves with higher amplitudes than the P-wave, which is consistent with the numerical results of Frehner (2014). Nakagawa et al. (2016) carried out an experimental study using frequencies below 1 kHz which is relevant to geophysical fracture characterization in field and observed a very low velocity in a fluid filled fracture. He found that the phase velocity and attenuation measured in the laboratory can be as much as one order of magnitude smaller than in the field observations when the compliance of the fracture is small.

In this dissertation, on one hand I study the propagation of crack waves propagation using the dynamic photoelasticity technique. I will focus on monitoring the stress pattern of the crack wave from which the movement, and transmission pattern of crack waves. In other words, this set up helps to visualize crack wave propagation from which a better understanding about crack wave attenuation and group velocity as important factors can be achieved. On the other hand, an analogue fracture constructed by an aluminum-fluid-aluminum trilayer model is adopted to for acoustic measurement of Krauklis wave dispersion property (the dependency of the velocity on the frequency), attenuation, and resonance frequencies under different conditions such as the variations of the fracture thickness, fluid viscosity, fracture compliance and fracture geometries and roughness.

In this dissertation, by considering different geometries, I will investigate the effect of crack geometry on the resonance, dispersion, and attenuation of the crack wave. This understanding is crucial to further modify the standard rectangular crack model to procure more realistic estimates about crack sizes and fluid properties from the crack waves. In addition, I will explore the effect of temperature on the crack waves. Understanding the effect of temperature on the crack waves might help us to link the temporal variations that we observe on LP events to changes in temperature in hydrothermal and magmatic systems. To this aim, I have developed a rock physics setup. In this set up, using pressure transduces, I record crack waves propagating in lab-scale crack models. These models are made from aluminum in which different crack geometries have been precisely machined.

Apart from the rock physics set up, I will study the crack wave propagation using an optical apparatus that is based on the photo-elasticity technique. This technique has been used to visualize seismic wave propagation. Using this technique, not only will I visualize crack wave propagation, but also I will investigate the effect of fluid viscosity on the attenuation and group velocity of the crack waves. This visualization can help us to better understand the mechanism of attenuation in cracks.

2 Experimental observation of Fluid-Filled Fractures Using the Dynamic Photoelasticity Technique

2.1 Abstract

We have developed an optical apparatus based on the dynamic photoelasticity technique to visualize and analyze the propagation of the Krauklis wave within an analog fluid-filled fracture. Although dynamic photoelasticity has been utilized by others to study seismic wave propagation, this study adds a quantitative analysis addressing dispersion properties. We physically modeled a fluid-filled fracture using transparent photoelastic-sensitive polycarbonate and non-sensitive acrylic plates. Then we used a pixel-based framework to analyze the dispersion of a Krauklis wave excited in the fracture. Through this pixel-based framework, we thus demonstrated that the dynamic photoelasticity technique can quantitively describe seismic wave propagation with a quality similar to experiments using conventional transducers (receivers) while additionally visualizing the seismic stress field. We also showed the capability of the method to analyze seismic data in the case of complex geometry by modeling a saw-tooth fracture. Using the saw-tooth fracture data, we observed that an increase in the fluid viscosity results in a decrease of the velocity of the Krauklis wave. Moreover, the fracture's geometry can strongly affect the characteristics of the Krauklis wave as we noted a higher Krauklis wave velocity for the saw-tooth case, as well as greater perturbation of the stress field.

2.2 Introduction

Fractures contribute significantly to fluid flow in many low-permeability rocks. In exploration for and development of unconventional reservoirs, it is crucial to identify highly fractured zones. Seismic methods provide critical information about subsurface fractures with relatively low cost, and therefore, are widely used for identifying fractures and monitoring their development during hydraulic fracturing. The Krauklis wave is a slow wave that can be initiated in a fluid-filled fracture, with a velocity lower than the speed of sound in the fracture fluid (Krauklis, 1962). Because the Krauklis wave exists only in fluid-filled fractures, it can provide fundamental information about the fracture size and the fluid involved (Lipovsky and Dunham, 2015; Liang et al., 2017; Sicking and Malin, 2019) suggesting that Krauklis wave analysis can be applied to fracture characterization.

The Krauklis wave is dispersive; that is, its velocity is a function of frequency. At low frequency, the phase velocity is near zero, and it increases with frequency to an upper limit close to the speed of sound in the fracture fluid. As a result, the Krauklis-wave group velocity, which is the velocity of a small wave packet spanning a bandwidth of frequencies (Askari and Ferguson, 2012; Askari and Hejazi, 2015), is larger than the phase velocity (velocity of a single frequency component). Because the fracture is, of course, embedded in a medium with higher velocities, the Krauklis wave's low velocity causes the fracture to act as a seismic source within that medium; the far-field signature is recognized in volcanic and hydraulic-fracturing data as long-period events (Chouet, 1986; 1988; Ferrazzini and Aki, 1987).

Tang and Cheng (1988) created an analog fracture using two thick aluminum cylinders as half-spaces, with a narrow flat gap filled with water between them, conclusively verifying the existence of the Krauklis wave. Following that approach, Hasson and Nagy (1997) developed a three-layer aluminum model and demonstrated that the Krauklis wave could also be initiated between two plates of finite thickness. While the frequencies used in the Tang and Cheng (1988) and Hasson and Nagy (1997) studies were on the order of megahertz, Nakagawa et al. (2015) developed an experimental apparatus to study the Krauklis wave at low frequencies (0-200 Hz).

For Krauklis waves to be useful in an exploration and development sense, there must be some method of remotely exciting them in fractures in the earth's crust. Shih and Frehner (2016) showed that the Krauklis wave could be generated from a body wave striking a fracture wall. Frehner and Schmalholz (2010) simulated the Krauklis wave reflection and scattering into the host medium at the tips of fluid-filled fractures using the finite-element method. Note that in all previous laboratory or numerical studies, the Krauklis wave was produced by initiating a pressure disturbance directly on the fracture plane.

In addition to these numerical and experimental studies, significant theoretical advances have been made in recent years. For instance, Korneev (2008) obtained the phase velocity of the Krauklis wave for inviscid and viscous fluids bounded between two half spaces (a thick fracture-wall model). Korneev et al. (2014) derived a phase velocity formulation for a thin fracture-wall model (finite thickness of walls in the host medium) and showed that the velocity of the Krauklis wave in a thin-wall fracture is lower than that in a thick-wall counterpart. Nakagawa and Korneev (2014) obtained the phase velocity of the Krauklis wave for compliant fractures (the clamping force is not infinite) and demonstrated that the phase velocity decreases when the clamping weakens.

However, most of the studies assumed idealized fracture geometry with flat surfaces for modeling convenience. Dynamic photoelasticity is a technique that can be employed to obtain the stress distribution and dynamic response of material to applied forces, and is particularly useful for studying complex geometries. This technique has been utilized to visualize seismic wave propagation, but not for the Krauklis wave. For instance, Riley and Dally (1966) studied seismic wave propagation in layered models and identified different waveforms using photoelastic models. Rossmanith and Shukla (1981) investigated stress wave diffraction at crack-tips to understand the interaction between stress waves and the crack. Shukla and Prakash (1990) measured seismic wave velocity and seismic wave attenuation in porous media as a function of fluid saturation. Xia et al. (2004) developed a photoelastic model to simulate earthquake rupture processes and examined the physical conditions under which ruptures could propagate at speeds greater than the host rock's shear-wave velocity. Namiki et al. (2019) developed a soft-rock analogue to investigate how fractures are developed when high-pressure air is injected into soft rocks. The promising results of these photoelastic studies motivated us to develop a trilayer apparatus to study seismic wave propagation in fluid-filled fractures through the use of photoelasticity. Using a pixel-based framework based on images made during wave propagation, we visualized the stress field of the Krauklis wave and analyzed its dispersive properties.

There are many parameters that likely affect Krauklis wave properties and a number of them have already been investigated (e.g., fracture fluid, fracture width, and fracture compliance; see Bayuk and Goloshubin, 2018 and Nakagawa and Korneev, 2014), but the effect of crack geometry on the Krauklis wave has remained untested. Using our photoelastic setup, we investigated the effects of fluid viscosity and crack geometry on the dispersion properties of Krauklis waves. Our results showed that the Krauklis wave velocity decreases with increasing viscosity, a result consistent with a previous study by Nakagawa et al. (2015) based on conventional transducers. In addition, we noted that fracture geometry could have strong effect on the Krauklis wave using saw-tooth geometry.

2.3 Method

2.3.1 Dynamic photoelasticity technique

Some materials are optically isotropic when they are not under stress yet become optically anisotropic under anisotropic stress (Pandya and Parey, 2013). The induced anisotropy or birefringence is proportional to the stress applied to the object (Pandya and Parey, 2013), and the fringe patterns can be correlated to the stress distribution (Ecault et al., 2013); a denser fringe pattern corresponds to a highly stressed area. To observe the fringe patterns and infer the correlated stress states, a polariscope is needed. As light enters an optically anisotropic material (called birefringent in the literature) it is split into fast and slow components due to the different refractive indexes of the material along the two principal stress directions. When the rays are recombined as they exit the birefringent material, the polarization state changes due to the phase difference resulting from the time delay between the fast and slow arrivals. That time delay is related to the difference in the refractive indices for the fast and slow arrivals, which in turn is proportional to the difference between the principal stresses.

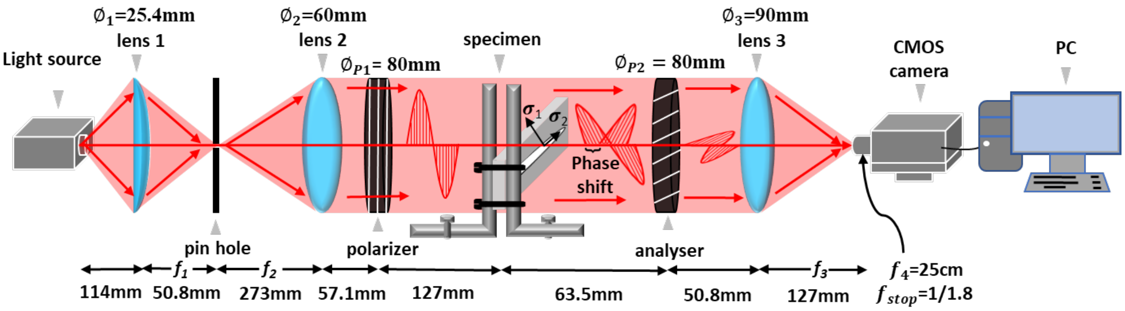

Figure 2-1. Schematic diagram of our optical apparatus. The specimen is placed between two L-shaped steel support brackets mounted on an optical table. The focal lengths *f* of each lens and diameters Ø of each optical component are indicated. σ_1 and σ_2 are two principal stresses of the sample. Details of the lenses are shown in Table 2-1.

We developed a linear polariscope apparatus (Figure 2-1) to visualize the stress field within the fluid-filled fracture. Our linear polariscope is composed of three parts: (i) a collimated light also known as a shadowgraph system, (ii) a linear light polarizer, and (iii) a high-speed camera. We built a custom beam expender that is composed of (i) a 150W 21V halogen light source, (ii) a plano-convex focusing lens with a focal length of 50.8 mm and a diameter of 25.4mm, (iii) a pinhole with adjustable aperture, and (iv) two collimated lenses with focal lengths of 273 mm and 127 mm, respectively (Table 2-1). In the first part, the pin hole after the convex lens (Figure 1) helps to minimize spherical aberration, a major issue in optical setups with spherical lenses (Yoshida, 1982). The second part includes two linear polarizers with the specimen in between. (In the photoelastic literature, the polarizer that is placed after the specimen is called the analyzer, and is labelled as such in Figure 2-1.) The directions of these two polarizers are set perpendicular to each other. In the third part, we used a high-speed camera with a capability of recording up to 250,000 frames per second (fps), but in this study, in order to allow more light flux into the camera for each frame, we selected recordings at 10,000 fps and optimizing spatial resolution. Our entire setup is mounted on a floating table to minimize noise.

Table 2-1. Parameters of the optical components

Lens	**Lens 1 (mm)**	**Lens 2 (mm)**	**Lens 3 (mm)**
Focal length	50.8	273	127
Diameter	25.4	60	90

The current linear polariscope provides a series of sample-wide images of photoelastic fringes over time. The brightness of each fringe is linearly related to the strain in the medium, such that the brighter a pixel is, the stronger the stress to which that element is subjected in each frame (Voloshin and Burger, 1983; Daniels and Hayman, 2008). In digital image processing, the brightness of a grayscale image is represented by pixel intensity values, which for our 8-bit system are integers ranging from 0 (black) to 255 (white). Therefore, the pixel values are qualitatively related in a linear manner to the stress levels at locations within the plate (Tercero et al., 2010). The pixel intensity values extracted from the photoelastic images are therefore adequate to estimate the dispersion properties of the Krauklis waves within the specimen. Quantitative calculation of stress levels requires additional optical components including two quarter-wave plates and one monochromatic filter to build what is called a circular polariscope; this is beyond the scope of this study, and not necessary to achieve our goals.

2.3.2 Trilayer model

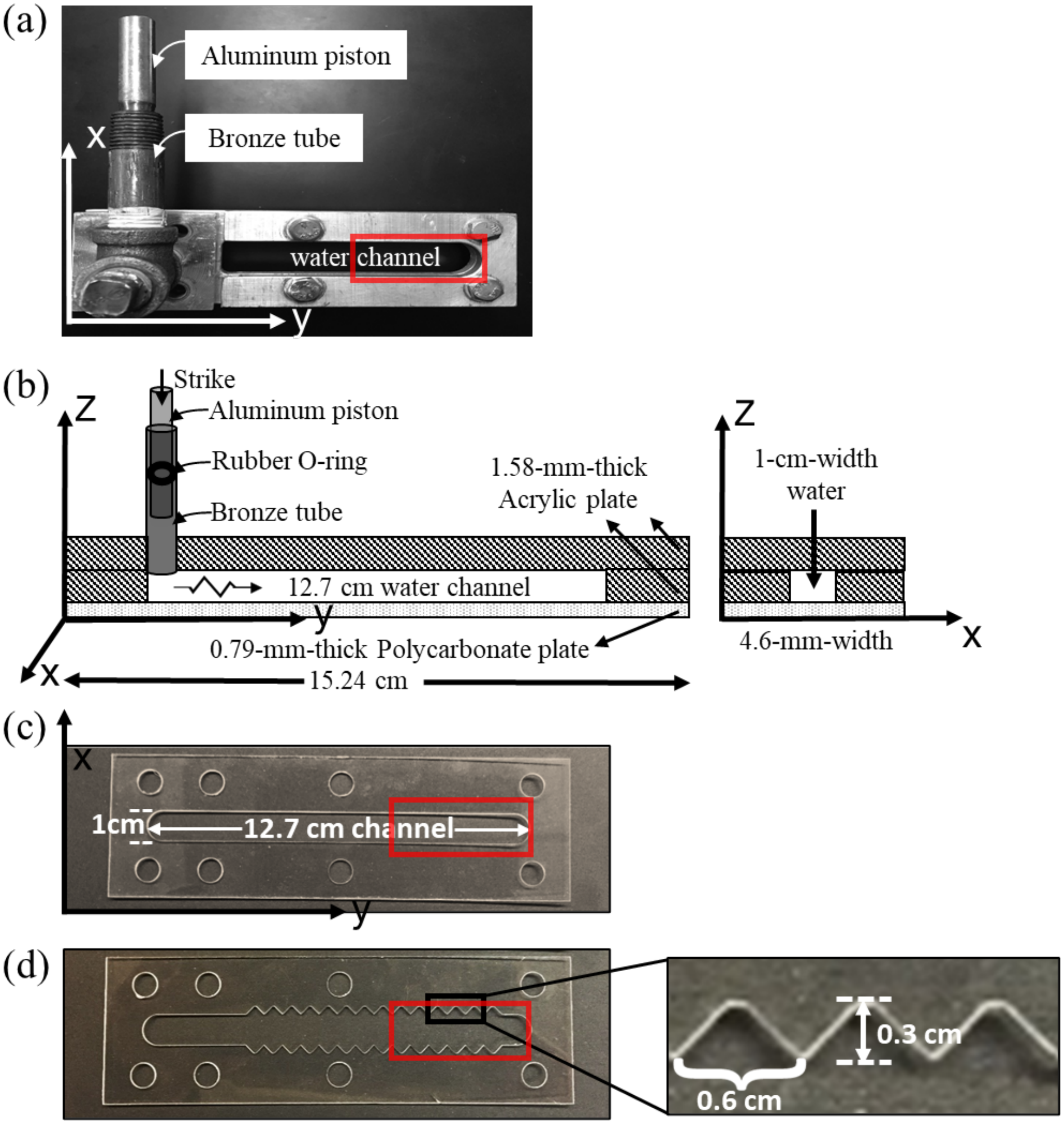

Figure 2-2. The (a) Transparent trilayer held by aluminum plate. (b) and (c) Cross-length and width views of the trilayer. (d) Flat smooth fracture model in the middle layer. (e) Saw-tooth fracture model with enlarged saw-tooth geometry details. In (d) and (e), the circles along the edges of the plates are the locations of screws. The pressure pulse is initiated by striking a hammer to the aluminum piston with a rubber O-ring in a bronze tube. (a) (c) and (d) are the view in *xy* plane. The area in the red rectangular are the locations of images to be analyzed.

In our experiment, we developed a trilayer fracture model by combining two photoelastic insensitive acrylic plates and one photoelastic sensitive polycarbonate plate. Both polycarbonate and acrylic plates are transparent and homogeneous, and the area containing the "fracture" is visible through an opening in the metal housing (Figure 2-2a). The top and middle layers of our model in Figure 2-2(b) are acrylic plates with a dimension of 152.4×47.6×1.58 mm whereas the bottom layer is a polycarbonate plate with a dimension of 152.4×47.6×0.79 mm. Therefore, the trilayer model is not symmetric because of the different layer thickness. The middle layer (acrylic) contains the "fracture." The bottom layer (polycarbonate) provides birefringence when stressed. We choose a thin polycarbonate layer because, according to Dally and Riley (1991), thinner photoelastic materials deform more significantly for a given external load, and thus, they yield a higher phase shift producing larger photoelastic fringes.

Table 2-2. The physical parameters of the solid medium of the trilayer.

Medium	ρ (g/cm^3)	V_p (m/s)	V_s (m/s)	E (Gpa)	Poisson ratio
Acrylic	1.19	2710	1391	2.76	0.32
Polycarbonate	1.19	2106	931	2.20	0.37

The physical properties of the two plates are shown in Table 2-2. In the middle layer, a machined slot is created to be filled by fluid. We considered the flat and saw-tooth slot models (Figure 2-2c,d) in which the slots have a dimension of about 127 mm×10 mm×1.58 mm; however, the saw-tooth crack is 0.3 mm larger in width due to the machined triangles (see Figure 2-2e for more details). The acrylic and polycarbonate plates are held together by two aluminum plates whose thickness is 5 mm (one at the top and the other at the bottom, Figure 2-2a). The two aluminum plates are tightened by eight screws along the edges of the specimen (Figure 2-2a). Compared with the dimension of the fracture length (127 mm), the polycarbonate plate used in our experiment is thin (0.79 mm) reducing the deformation and stress in the plate to a two-dimensional problem (Brown and Srawley. 1966). In addition, the wavelength estimated from the following experimental result is much larger than the plate thickness; this warrants treating the trilayer model with classical plate theory.

2.4 Experiments

To investigate the effects of viscosity and fracture geometry on the Krauklis wave, we performed three experiments, using water as the fracture fluid in the flat fracture model and shampoo in both the flat and saw-tooth models. (In addition, we performed an experiment with water in the saw-tooth fracture; this resulted in strong cavitation effects which overwhelmed the images, precluding an accurate visualization of the stress field associated with the Krauklis wave. Therefore, we present only the results of the three experiments for which the results were interpretable.) Table 2-3 summarizes the experiments and major observations.

Table 2-3. Experiments and major observations.

Experiment	**Fracture**	**Fracture**	**Major Observation**
1	Flat	Water	Highest-frequency spectra and velocity of the Krauklis wave compared to Experiments 2 and 3.
2	Flat	Shampoo	Lowest velocity and lowest frequency spectra of Krauklis wave.
3	Saw-tooth	Shampoo	Higher velocity (almost twice) compared to Experiment 2. High perturbation of the stress field.

To initiate the Krauklis wave, a sharp pressure load was applied by a hammer striking on an aluminum piston, surrounded by a rubber O-ring, in a bronze tube connected perpendicularly to the specimen to the right side of the trilayer (as viewed in Figure 2a). Unfortunately, this source is not repeatable with precision, and as discussed later, it is one of the major issues to be modified for future studies. Some studies of stress wave propagation have, in the past, used small dynamite explosions as a source (Shukla, 1991); however, current lab regulations preclude such use of explosive material. On the other hand, we were able to obtain relatively good-quality data from this source.

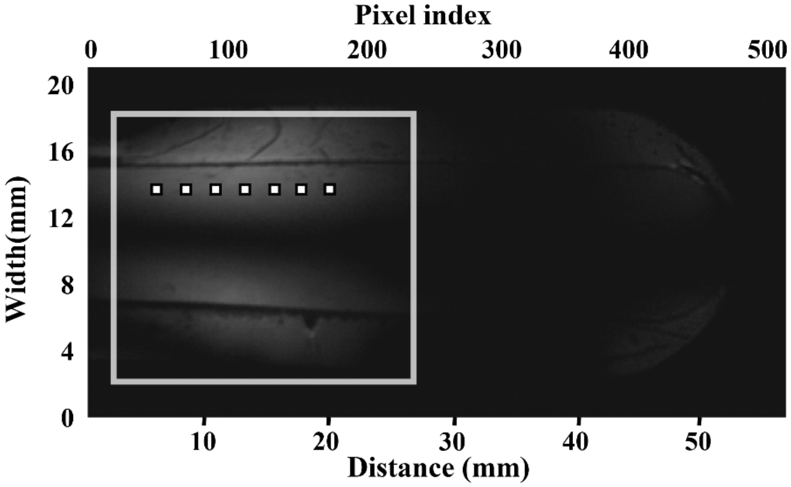

Figure 2-3**.** An example of a photoelastic image from the flat fracture filled with water. Two bright zones (superimpositions of fringes) are noticeable, highlighted by the box. These fringes indicate deformation associated with the Krauklis wave as it travelled along both solid-fluid interfaces from the source out of the image to the right. The points shown as bright squares are "receiver" locations at which we recorded the temporal stress field (waveform) by tracking the pixel values at one point using an image sequence. The overall image length (width) is about 5.715 cm (2.85 cm) and contains 512 pixels (256 pixels) in each dimension for a pixel size of 0.112 mm.

The original photoelastic images are typically displayed in grey scale. Figure 2-3 shows an example photoelastic image from the flat fracture filled with water in which the bright zones are under-stress regions. For our image processing, we use the "imread" command in MATLAB to read each of the raw grayscale images as a 512×256 matrix of unit8 (8-bit) values (integers 0-255). Then, in order to improve visualization, we applied a spline interpolation of 10 points between each neighboring pixel value to smooth the extracted raw waveform; this interpolation requires conversion to double precision. Thus, each image provides a high-resolution "map" of the stresses associated with the Krauklis wave as it propagates along the fracture (and eventually is reflected). These images, from frame to frame, can be used to map the wave's propagation. A trace was extracted by tracking the pixel values over time at one point ("receiver") (see Figure 2-3) for each frame. To obtain the phase velocity dispersion curve of the Krauklis wave, we applied a high-resolution linear Radon transform (HRLRT) to these waveforms (Luo, 2009).

2.5 Results

For ease of visualization, a series of photoelasticity images (512×256) are shown in Figure 2-4, this time in pseudo-color, for Experiment 1 (flat fracture filled with water). We clearly observed the Krauklis wave traveling slowly along the fracture (in the orientation of this image, from left to right). By mapping the locations of the maximum stress and noting their corresponding times, we obtained a group velocity of 34 m/s, which is quite low compared to the speed of sound in water (1500 m/s). We did not observe a “direct” water wave because the thickness of the fracture layer is very small compared with the wavelengths of the spectral components, as will become evident later.

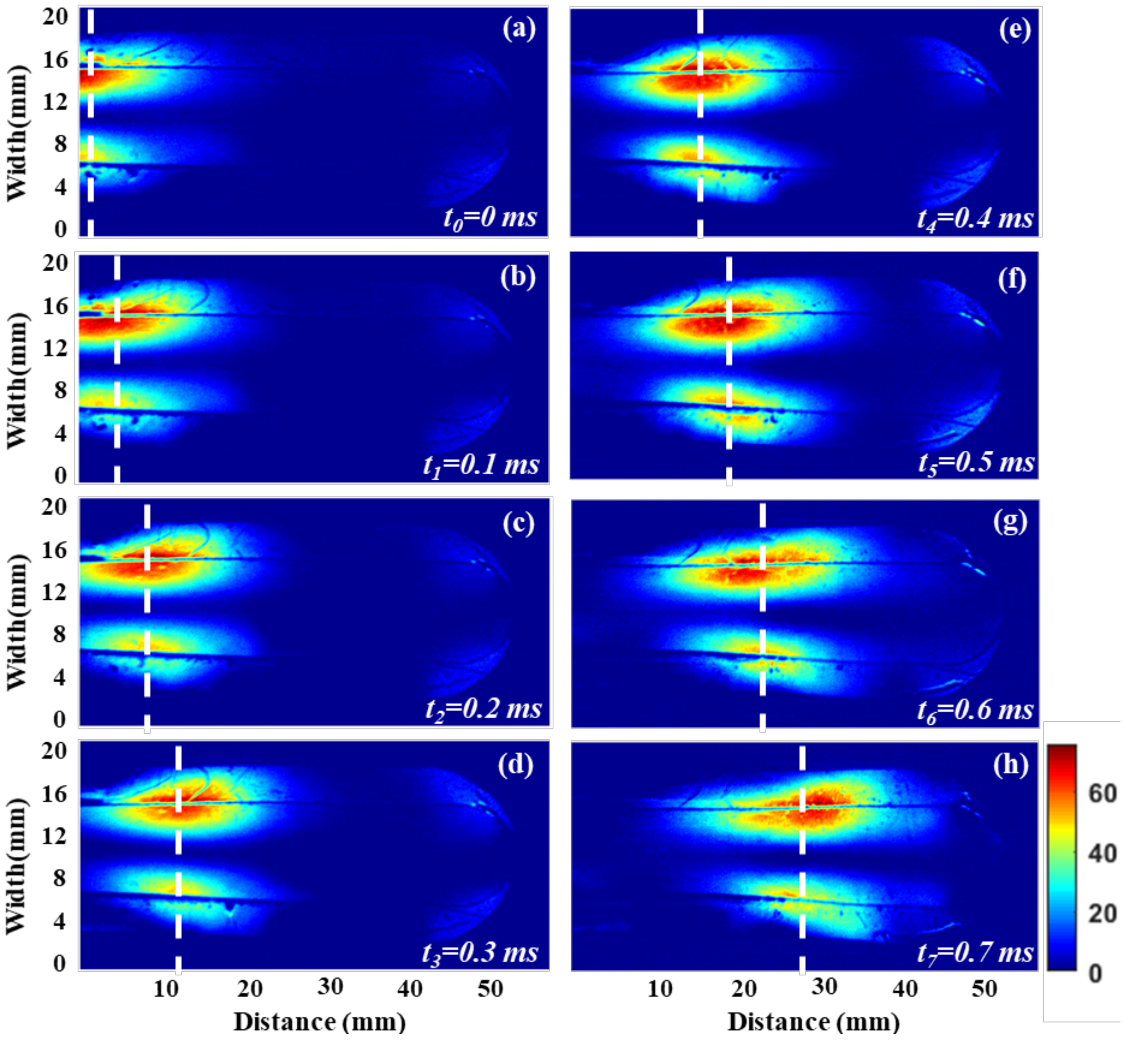

Figure 2-4**.** Pseudo-color photoelastic images of Experiment 1 (flat fracture filled with water), shown every 0.1 ms. The white dashed lines correspond to the areas with the maximum stress of the Krauklis wave. The color bar shows the pixel intensity value.

For Experiments 2 and 3, using a viscous shampoo in both the flat and saw-tooth fractures, we obtained the group velocities of 14.6 m/s and 28.3 m/s from Figure 2-5 and Figure 2-6 respectively. Given the higher viscosity of the shampoo (910 to nearly 9600 mPa·s according to AlQuadeib et al (2018) compared to water 1.0 mPa.s), a lower velocity of the Krauklis wave is expected, according to Korneev (2008). However, the velocity of the Krauklis wave in the saw-tooth fracture (Figure 2-6) is almost double that in the flat fracture (Figure 2-5), which might imply the importance of fracture geometry on the Krauklis wave. We note that the amplitude of the saw-tooth themselves is a significant fraction of the width of the overall fracture, and, as is apparent in Figure 2-6, comparable to the wavelength of the major spectral components of the Krauklis wave. Thus, Experiment 3 appears to demonstrate the effect of large-scale heterogeneous fracture structure, complete with internal reflections.

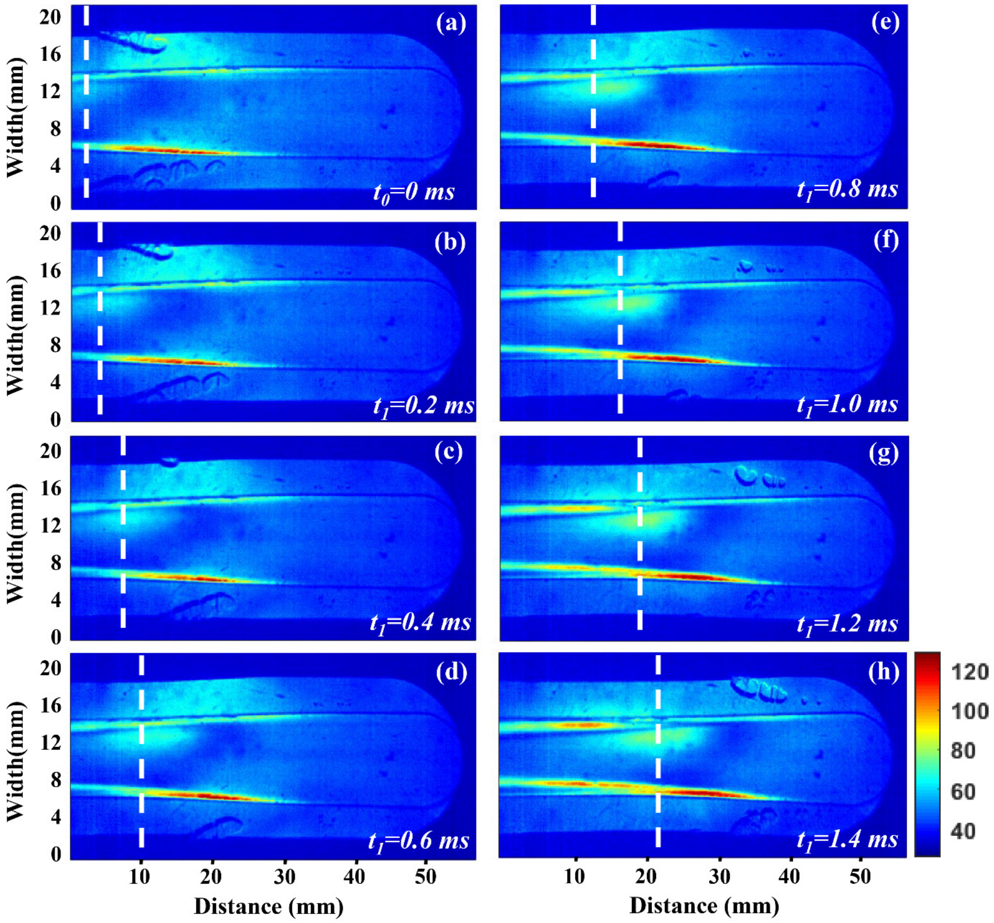

Figure 2-5. Pseudo-color photoelastic images of Experiment 2 (flat fracture filled with viscous shampoo). The stress is more concentrated along the fracture boundary than in Experiment 1. Some residual stress is noticeable at the lower part of the fracture that may be due to some experimental weakness: (i) inadequate or over-tightening of screws or (ii) manufacturing flaws in the fracture model. In spite of that residual stress, the propagation of the Krauklis wave is clearly defined.

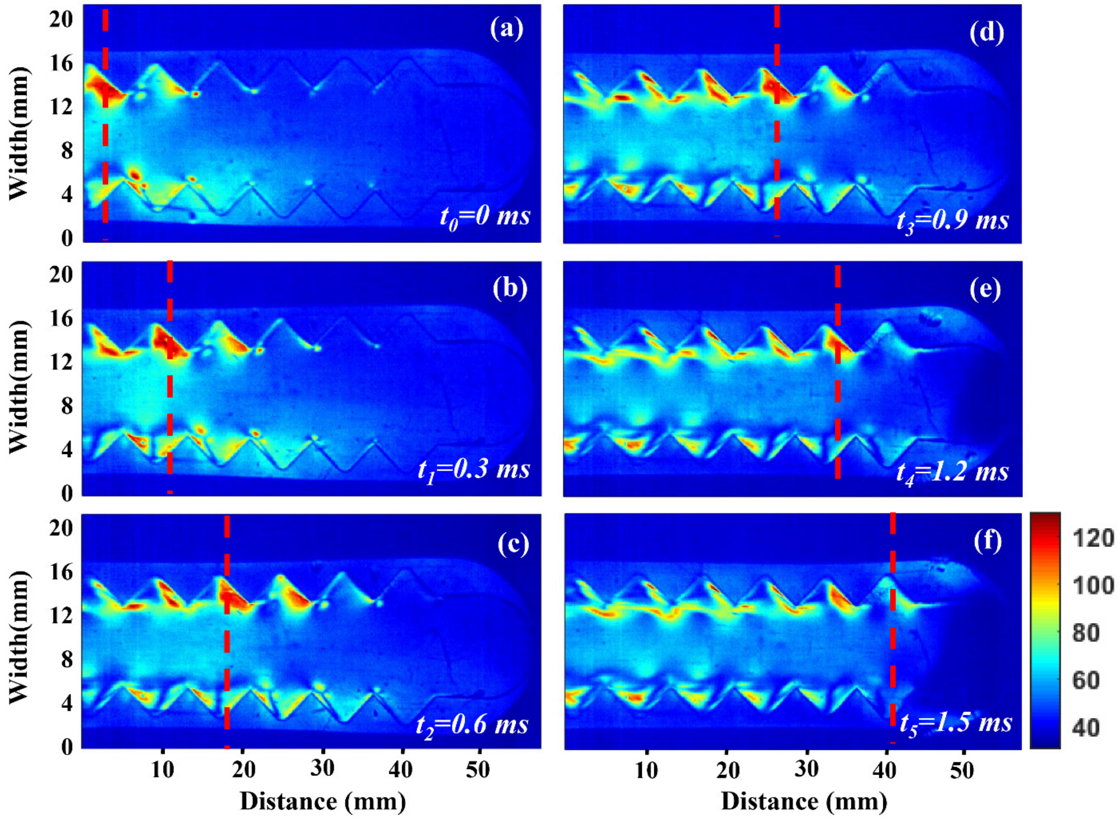

Figure 2-6**.** Pseudo-color photoelastic images of Experiment 3 (saw-tooth fracture filled with shampoo). The red dashed lines correspond to the maximum stress field initiated by the Krauklis waves. Due to the residual stress (either from screwing or manufacturing) at the bottom of the frames, the identification of the stress field of the Krauklis wave at the lower part of the specimen is difficult. Internal reflections of the Krauklis wave are noticeable that cause perturbation in the stress field. It is clear that the wave is strongly disrupted by the saw-tooth nature of the fracture boundary.

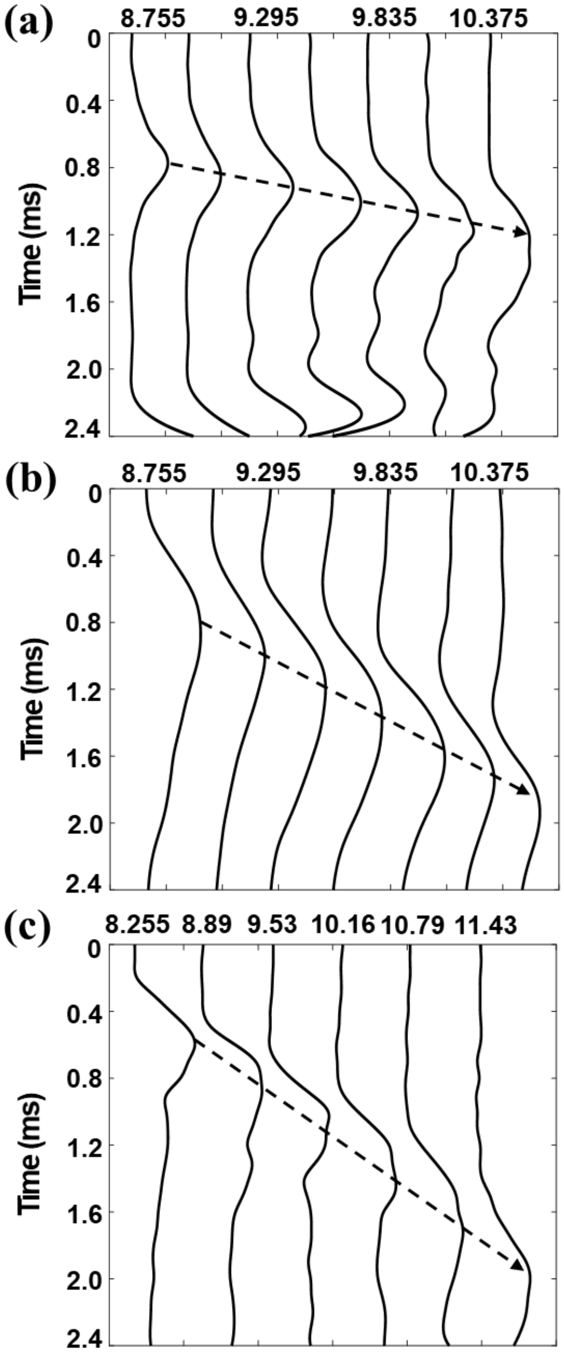

Figure 2-7**.** The temporal stress field of the Krauklis wave of Experiments 1, 2, and 3, in (a), (b) and (c), respectively. The waveforms of Experiments 1 and 2 are obtained from the seven fixed points indicated in Figure 3 whereas those of Experiment 3 are from the six tooth of the saw-tooth fracture. The dashed arrow follows the maximum stress field of the Krauklis wave from which we estimate the group velocity. Comparing the first and last traces, we note that the duration of signals increases as the Krauklis wave travels, implying that the high frequencies are significantly attenuated.

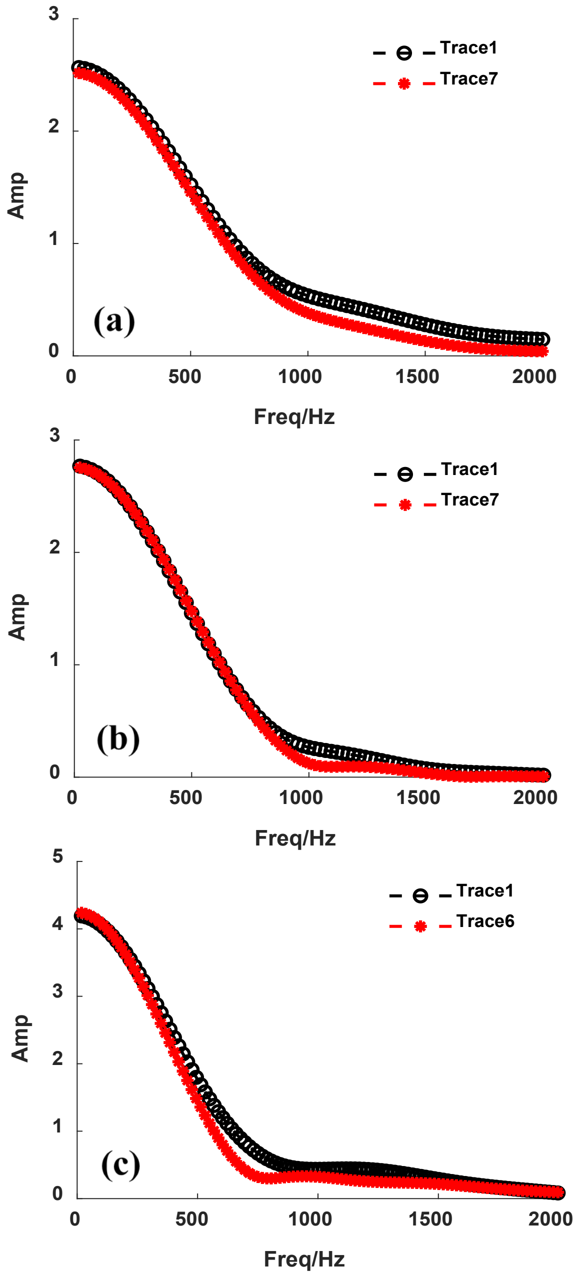

Figure 2-8. The amplitude spectra of the first and last traces of the temporal stress fields of Experiments 1, 2, and 3, shown in (a), (b), and (c), respectively, from the traces in Figures 7a-c. As the Krauklis wave travels, the high frequencies are attenuated. The Krauklis wave from Experiment 1 (a) is richer in high frequencies than Experiments 2 and 3, due to the lower viscosity of water (Experiment 1). Note that the data from Experiment 3 (shampoo in saw-tooth fracture, shown in c) contains higher frequencies (> 1000 Hz) than present in Experiment 2 (shampoo in flat fracture, shown in b), which likely implies the effect of the large-scale geometric heterogeneities.

The waveforms extracted from the images at several points near the fracture boundary are shown (normalized) in Figure 2-7; dispersion is noticeable all three experiments as the waveforms change shape over time. As the Krauklis wave travels, the temporal stress field is stretched out in time, which implies the attenuation of high frequencies, also observable from the amplitude spectra of the first and last traces, shown in Figure 2-8. (To provide high resolution of the amplitude spectra we applied a Hanning window and zero-padded the raw data.) In addition, from Figure 2-8b and c, we note that the frequencies higher than 1000 Hz are better retained in the saw-tooth fracture than in the flat fracture. The waveforms extracted from the data are then used to determine phase velocities from dispersion curves.

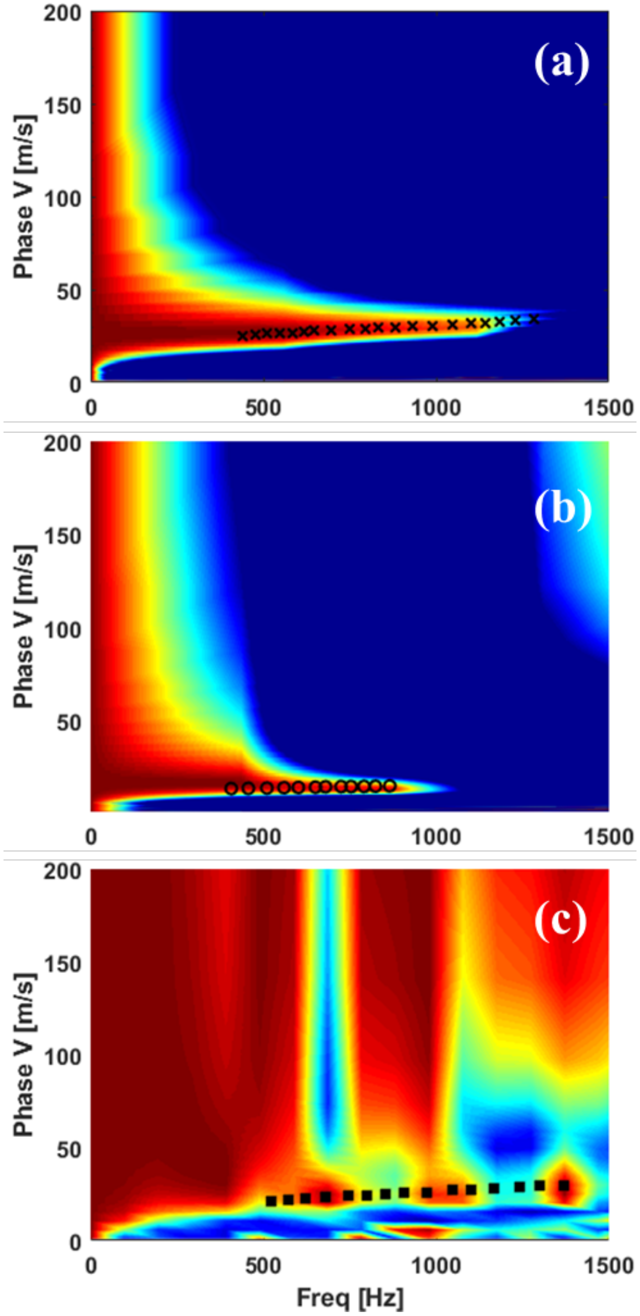

Figure 2-9. Dispersion curves extracted by high-resolution linear Radon transform for Experiments 1, 2, and 3 in (a), (b), and (c), respectively. The black markers represent the picked dispersion curves. The poor resolution at frequencies below 500 Hz is due to the short length of the array over which the dispersion analysis is conducted. In addition, we note that the dispersion curve is not continuous in (c) due to the large-scale perturbation of the stress field in Experiment 3. Due to the lack of high frequencies in Experiment 2 (see Figure 9b), no velocity trend at frequencies higher than 900 Hz was obtained for that experiment.

Dispersion curves of phase velocities are shown in Figure 2-9, where phase velocity trends at frequencies above 500 Hz are recognizable; at frequencies below 500 Hz, the resolution is poor. The primary reason for the poor phase velocity resolution at the low frequencies is the short aperture over which traces were analyzed, therefore only a fraction of a wave cycle across the array is captured, but limited trace numbers and spacing also contribute to the resolution. The dispersion curve is not continuous in Figure 2-9c (viscous shampoo in saw-tooth fracture) because of the perturbation of the stress field, which as mentioned, is due to the internal reflections and scattering of the Krauklis wave within and between each "tooth" of the saw-tooth fracture. To verify this last point, we calculate the spectral decomposition of the series of waveforms (from Figure 2-7c) using the Sparse S transform (see Figure 2-10); highly perturbed energy at the frequencies of 750 Hz and 1100 Hz is noticeable after spectral decomposition on the time-frequency plane.

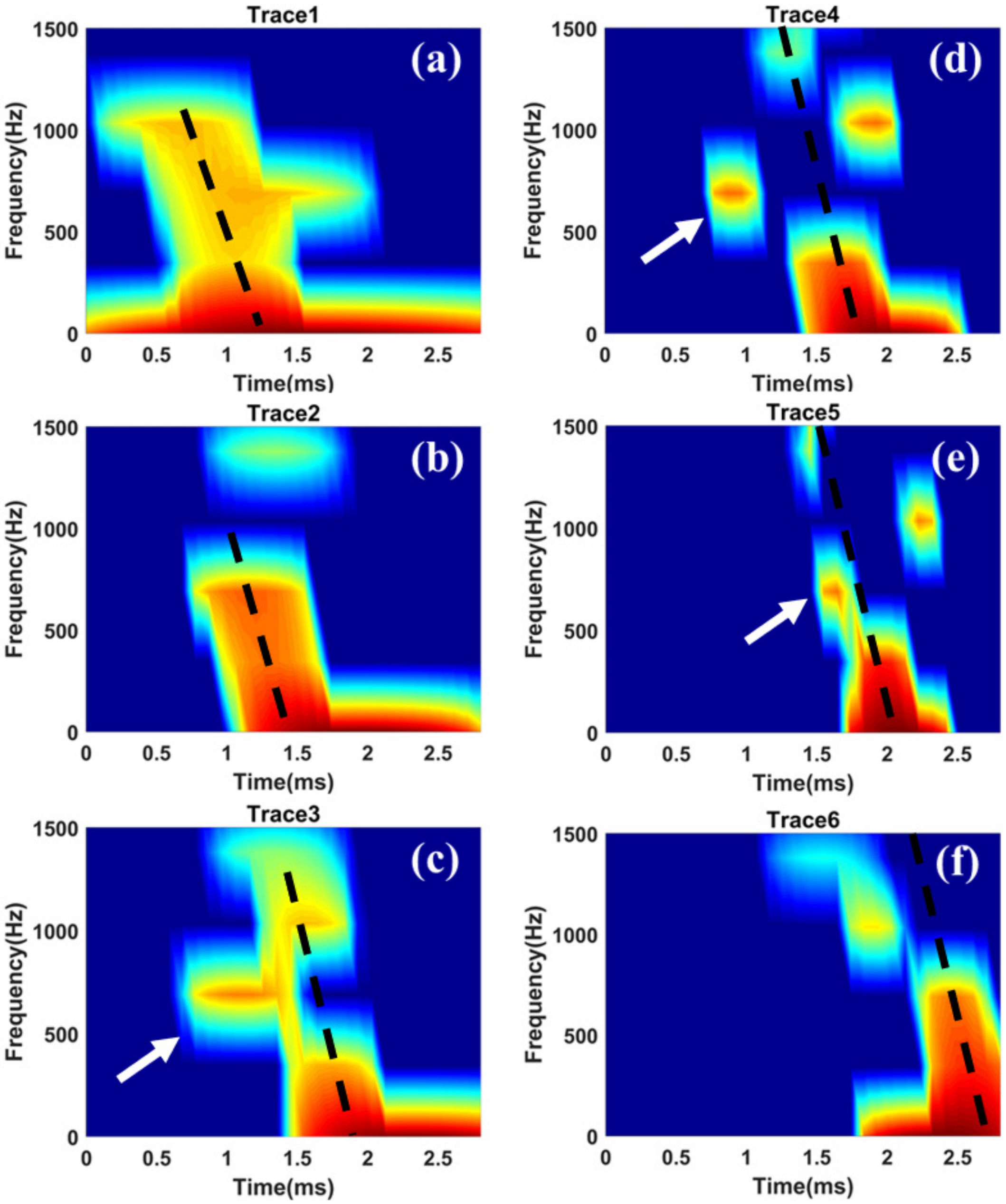

Figure 2-10**.** Spectral decomposition of the waveforms from Experiment 3 as shown in Figure 7c. The dashed lines correspond to the general trend of the stress field of the Krauklis waves. We note that high frequencies arrive earlier, which is consistent with the theory. Some perturbation has been highlighted by arrows. The first three traces show that the high-frequency contents attenuate faster than the low frequency contents.

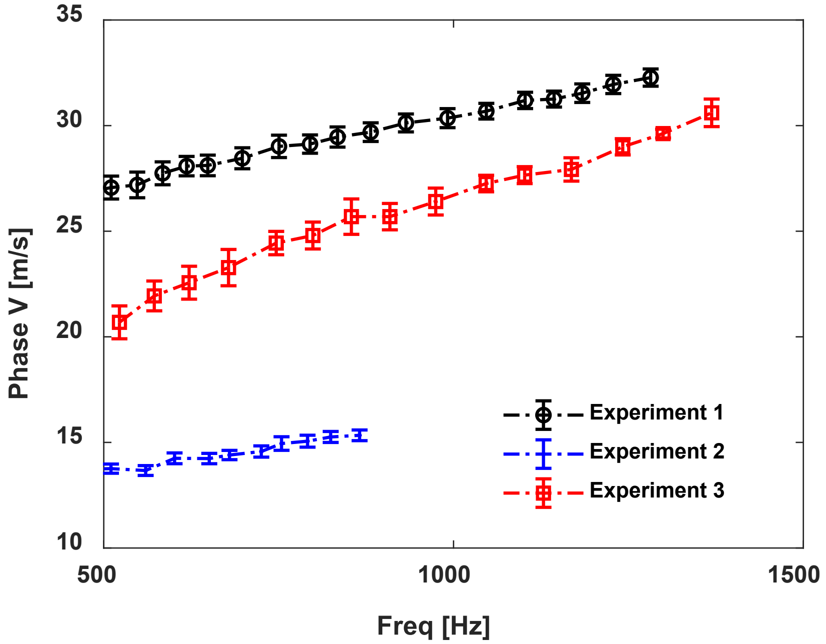

Figure 2-11. The dispersion curve of the Krauklis wave for the three experiments. Note that the flat water filled fracture has the highest velocity. The velocity significantly increased in the saw-tooth fracture filled with shampoo (Experiment 3 compared to Experiment 2), which implies the possible effect of the geometry on the dispersion of the Krauklis wave.

The phase velocities of the three experiments are compared in Figure 2-11. As expected, the highest velocity belongs to the experiment in which the fluid is water, with its low viscosity (Experiment 1). By increasing the viscosity through the use of shampoo, the phase velocity significantly decreased in Experiment 2; in addition, the phase velocity is not estimable at frequencies higher than 900 Hz because those frequencies are highly attenuated in this high-viscosity environment. The most interesting observation is the dramatic increase of the phase velocity in Experiment 3 compared with Experiment 2, in which the same high-viscosity fluid is contained in either a flat fracture (Experiment 2, lower velocity) or a saw-tooth fracture (Experiment 3, higher velocity). Our observation indicates that the fracture geometry is an important factor that should be considered when we interpret the Krauklis wave or long-period (LP) events data.

2.6 Repeatability

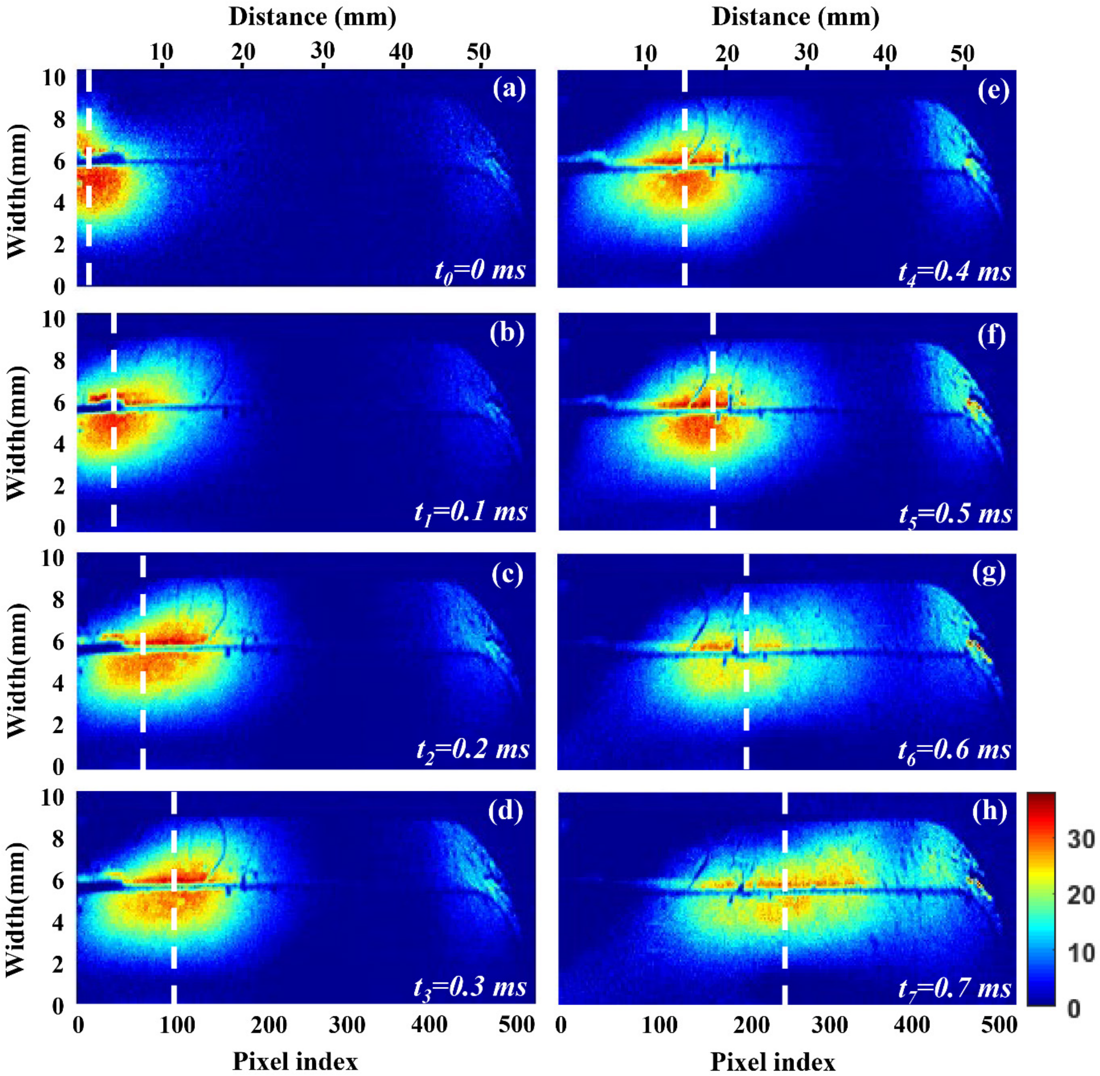

Figure 2-12. The photoelastic images of a manually repeated Experiment 1 (flat fracture filled with water). The white dashed lines correspond to the areas with the maximum stress of the Krauklis wave.

To show the repeatability of our experiment, which depends on manually striking a piston, the procedure was re-applied to the flat fracture filled with water (Experiment 1). Photoelastic images of the Krauklis wave motion on the upper fracture boundary are observed in Figure 2-12, and the extracted temporal waveform and the dispersion curve in Figure 2-13 demonstrate the experiment repeatability. Due to the difficulty of the experiment, multiple repetitions were not deemed worthwhile.

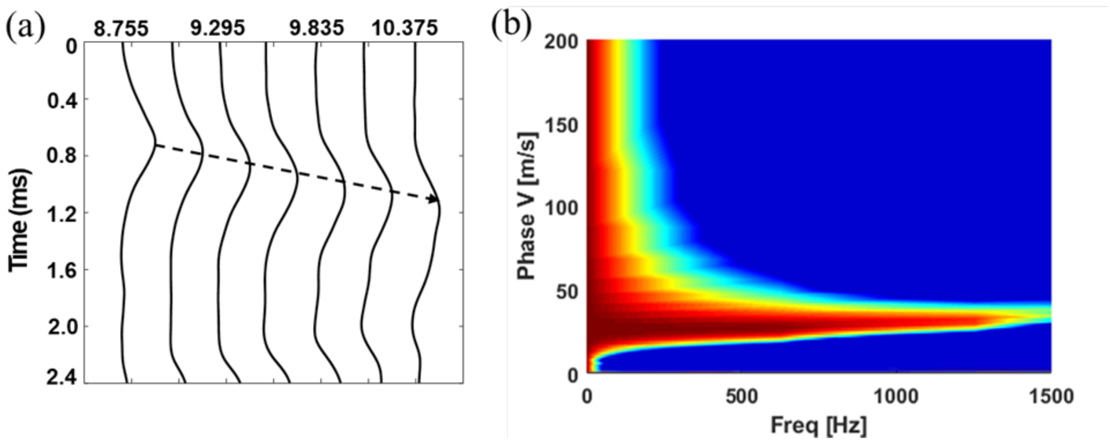

Figure 2-13**.** (a) The temporal waveform of the Krauklis wave of the repeated Experiment 1. The dashed arrow shows the maximum stress field of the Krauklis wave of the image sequence. (b) The dispersion curve extracted by high-resolution linear Radon transform for the repeated Experiment 1.

2.7 Discussion

The phase V_{ph} and group velocities V_{ph} are linked to the frequency (f) and wavenumber (k) respectively by

$$V_{ph} = f/k, \tag{1}$$

and

$$V_g = df/dk. \tag{2}$$

Therefore, the phase velocity is linked to the group velocity (e.g., Askari and Ferguson, 2012) via

$$V_g = \frac{V_{ph}^2}{V_{ph} - f\frac{dV_{ph}}{df}}. \tag{3}$$

Because the phase velocity of the Krauklis wave increases with frequency, $\frac{dV_{ph}}{df} > 0$, the group velocity will be greater than the phase velocity, $V_g > V_{ph}$. This "inverse dispersion" property of the Krauklis wave is consistent with our results as all the experiments noted a higher group velocity than phase velocity for nearly all frequencies; the highest frequencies, at which $V_{ph} > V_g$, are presumably low-enough amplitude that the simple calculation of V_g is not sufficiently weighted to them.

The phase velocity we obtained in Figure 9(a) for the flat fracture filled with inviscid and incompressible water can be validated using the width-averaged theoretical model (Dunham and Ogden, 2012). The polycarbonate plate is subject to internal pressure from the constrained fluid pulse and the coupling effects at the solid-fluid interface cause the polycarbonate plate to bend. The wavelength calculated from the dispersion curve in Figure 9(a) is 25-58 mm, much larger than the plate thickness, allowing us to treat the trilayer model with plate theory. Therefore, the shear stress components within the polycarbonate layer can be neglected. The governing equation for the dynamic deflection of the plates on the two side of the fluid layer (Timoshenko and Woinowsky-Krieger, 1959)

$$P = \frac{-(D_1+D_2)d^4w}{dx^4} \qquad (4)$$

$$D = \frac{Eh^3}{12(1-\nu^2)} \qquad (5)$$

Where ΔP is pressure change in the fluid (normal traction on plate walls), D is bending stiffness (D_1 for polycarbonate plate and D_2 for acrylic plate), w is displacement normal to plate walls, E is Young's modulus, h is plate thickness and ν is Poisson ratio.

The mass and moment balance of an incompressible inviscid fluid is

$$\frac{dw}{dt} + w_0\frac{du}{dx} = 0 \qquad (6)$$

$$\rho\frac{du}{dt} + \frac{dP}{dx} = 0 \qquad (7)$$

where w_0 is thickness of fluid layer and ρ is fluid density.

The complex notation for the fluid velocity is

$$u(x,t) = Ae^{i(kx-\omega t)} \qquad (8)$$

Combining equations from (4) to (7) results in

$$\rho\frac{\partial^2 u}{\partial t^2} + w_0((D_1 + D_2)\frac{\partial^6 u}{\partial x^6} = 0 \qquad (8)$$

And applying the Fourier transform yields the following the dispersion relation

$$\omega^2 = \frac{k^6 w_0 (D_1 + D_2)}{\rho} \qquad (9)$$

Therefore, the phase velocity of the Krauklis wave is

$$V_{ph} = k^2 \sqrt{\frac{w_0 (D_1 + D_2)}{\rho}} \qquad (10)$$

Using an example wavelength of 40 mm at around 700 Hz and reported fluid and solid properties in Table 2, the phase velocity calculated V_{ph}= 32.9 m/s. This result is close to our estimated phase velocity in Experiment 1 (water in a flat fracture) that is about 28.5 m/s.

To summarize our observations, the dispersion properties of the stress fields obtained from our experiments are consistent with the characteristics of the Krauklis wave as (i) the estimated velocities are lower than the speed of sound in the fracture fluid, (ii) the phase velocities increase with increasing frequency, (iii) the group velocities are higher than the phase velocity, and (iv) our estimate of the phase velocity in Experiment 1 is consistent with the theoretical value. Therefore, we conclude that what we have recorded is the Krauklis wave.

The higher phase and group velocities in Experiment 3 (viscous shampoo in a saw-tooth fracture), and the qualitative observation that extremely high strains occurred in an experiment using low-viscosity water in the saw-tooth fracture, require additional explanation. One could look more closely at the stress distributions (Figure 6) and conclude that the Krauklis wave may, in fact, be scattering at each saw-tooth, effectively as body waves propagating in the acrylic saw-tooth bounding the fracture, only to be re-excited at the next saw-tooth, and so on. The phenomenon of Krauklis wave excitation by passing body waves was presented by Frehner (2014). Therefore, the total travel time is significantly reduced due to the presence of the convex saw-tooth allowing the body waves propagation. This explains why the saw-tooth fracture, with its large-scale heterogeneity, results in the nearly doubled group and phase velocities.

Although the major advantage of conventional photoelasticity technique is to measure the stress, particularly for complex objects (Smith, 1980) as we showed in this study, this technique can also be used to study the dispersion properties of the Krauklis wave similarly to studies usually applied to experiments using a series of conventional transducers. Therefore, such physical models as ours can provide additional information about the state of stress of seismic wave within fluid-filled fractures, something difficult to arrange with physical transducers, and can yield additional understanding of the physics of the Krauklis wave.

One could further improve our physical model by addressing some of the issues we have discovered in the current apparatus. One problem is how to screw the aluminum plates (Figure 2a) evenly, in a controlled manner, so that the screws apply a uniform stress to the specimen that warrants the even stiffness throughout the fracture. We should also be able to measure the stress from the screws (for example, using a stress/strain gauge) so that the data could be studied with respect to the theoretical models (e.g., Nakagawa and Korneev, 2014). Using a larger lens and polarizers, one could model larger specimens. This would allow one to obtain the temporal stress fields at more points, and for a greater distance, along the specimens, and thus a higher-resolution of dispersion curves, particularly at low-frequencies, could be achieved. In addition, one could use photoelastic materials with higher stress-optic coefficients and lower manufactured residual stresses to further improve the results.

2.8 Conclusion

We demonstrated the possibility of visualizing the propagation of the Krauklis wave using the dynamic photoelasticity method. Using a pixel-based framework, we quantitatively processed and analysed the dispersion properties (phase and group velocities) of the Krauklis wave. Our results for the dispersion properties of the Krauklis waves are consistent with those studies conducted using conventional transducers. Therefore, we conclude that the dynamic photoelasticity has a potential to be used for more detailed quantitative analyses, particularly if further improvements are applied to the setup introduced in this study, as discussed previously.

Using the saw-tooth fracture, we showed the capacity of the photoelasticity method to analyze seismic wave propagation for complex geometries. In addition, we note that the geometry has a salient effect on the characteristics of the Krauklis wave, as a higher phase velocity compared to Experiment 2 and more perturbations in the stress field were observed.

2.9 Reference

Aki, K., Fehler, M. and Das, S., 1977, Source mechanism of volcanic tremor: Fluid-driven crack models and their application to the 1963 Kilauea eruption: Journal of volcanology and geothermal research, **2**, 259-287.

AlQuadeib, B.T., Eltahir, E.K., Banafa, R.A. and Al-Hadhairi, L.A., 2018, Pharmaceutical evaluation of different shampoo brands in local Saudi market: Saudi pharmaceutical journal, **26**, 98-106.

Askari, R., and R. J. Ferguson, 2012, Dispersion and the dissipative characteristics of surface waves in the generalized S-transform domain dispersion and dissipation of surface waves: Geophysics, **77**, V11-V20.

Askari, R., and S. H. Hejazi, 2015, Estimation of surface-wave group velocity using slant stack in the generalized S-transform domain surface-wave group velocity estimation: Geophysics, **80**, 83-92.

Bayuk, I.O. and Goloshubin, G.M., 2018, Rock physics modelling of viscoelastic properties of fractured reservoir rocks incorporating Krauklis wave: Geophysical Journal International, **215**, 1931-1942.

Brown, W. and Srawley, J., 1966, Plane strain crack toughness testing of high strength metallic materials: ASTM International.

Cao, H., Medici, E. and Askari, R., 2018. Experimental investigation of Krauklis wave propagation velocity in trilayer using dynamic photo-elasticity. 88th Annual International Meeting, SEG, Expanded Abstracts, 5108-5112.

Chouet, B., 1986, Dynamics of a fluid-driven crack in three dimensions by the finite difference method: Journal of Geophysical Research, **91**, 13967–13992.

Chouet, B., 1988, Resonance of a fluid-driven crack: Radiation properties and implications for the source of long-period events and harmonic tremor: Journal of Geophysical Research: Solid Earth, **93**, 4375-4400.

Dally, J.W. and Riley, W.F., 1991. Experimental stress analysis. McGraw and Hill, New York.

Daniels, K.E. and Hayman, N.W., 2008, Force chains in seismogenic faults visualized with photoelastic granular shear experiments: Journal of Geophysical Research: Solid Earth, **113**(11)

Dunham, E.M. and Ogden, D.E., 2012, Guided waves along fluid-filled cracks in elastic solids and instability at high flow rates: Journal of applied mechanics, **79**(3).

Ecault, R., Berthe, L., Boustie, M., Touchard, F., Lescoute, E., Sollier, A., Mercier, P. and Benier, J., 2013, Observation of the shock wave propagation induced by a high-power laser irradiation into an epoxy material: Journal of Physics D: Applied Physics, **46**, 235501.

Esfahani, R. D. D., R. Askari, and A. Gholami, 2018, Sparsity-promoting method to estimate the dispersion curve of surface-wave group velocity: Geophysics, **84**, V33-V43.

Ferrazzini, V. and Aki, K., 1987, Slow waves trapped in a fluid-filled infinite crack: Implication for volcanic tremor. Journal of Geophysical Research: Solid Earth, **92**, 9215-9223.

Frehner, M., and S. Schmalholz, 2010, Finite-element simulations of Stoneley guided wave reflection and scattering at the tips of fluid-filled fractures: Geophysics, **75**, 23-36.

Frehner, M., 2014, Krauklis wave initiation in fluid-filled fractures by seismic body waves. Geophysics: **79**, 27-35.

Hassan, W., and P. E. Nagy, 1997, On the low-frequency oscillation of a fluid layer between two elastic plates: Journal of the Acoustic Society of America, **102**, 3343–3348.

Korneev, V. A., 2008, Slow waves in fractures filled with viscous fluid: Geophysics, **73**, 1–7.

Korneev, V. A., Danilovskaya, L., Nakagawa, S. and Moridis, G., 2014. Krauklis wave in a trilayer: Geophysics, **79**, 33-39.

Krauklis, P.V., 1962, On some low-frequency vibrations of a liquid layer in an elastic medium: Journal of Applied Mathematics and Mechanics, ***26***, 1685-1692.

Liang, C., O'Reilly, O., Dunham, E.M. and Moos, D., 2017, Hydraulic fracture diagnostics from Krauklis-wave resonance and tube-wave reflections: Geophysics, **82**, 171-186.

Lipovsky, B.P. and Dunham, E.M., 2015, Vibrational modes of hydraulic fractures: Inference of fracture geometry from resonant frequencies and attenuation: Journal of Geophysical Research: Solid Earth, **120**, 1080-1107.

Luo, Y., Xia, J., Miller, R.D., Xu, Y., Liu, J. and Liu, Q., 2009, Rayleigh-wave mode separation by high-resolution linear Radon transform: Geophysical Journal International, **179**, 254-264.

Yoshida, A., 1982. Spherical aberration in beam optical systems. Applied optics, **21**, 1812-1816.

Nakagawa, S. and Korneev, V.A., 2014, Effect of fracture compliance on wave propagation within a fluid-filled fracture: The Journal of the Acoustical Society of America, **135**, 3186-3197.

Nakagawa, S., Nakashima S. and Korneev, V.A., 2015, Laboratory measurements of guided-wave propagation within a fluid-saturated fracture: Geophysical Prospecting, **64**, 143-156.

Namiki, A., Takahashi, M. and Tsutsui, R., 2019, A model experiment of fracture induced Long-Period events: Injection of pressurized gas into a viscoelastic rock analog. Geophysical Research Letters, 46(21), 11906-11914.

Pandya, Y. and Parey, A., 2013, Experimental investigation of spur gear tooth mesh stiffness in the presence of crack using photoelasticity technique: Engineering Failure Analysis, **34**, 488-500.

Riley, W.F. and Dally, J.W., 1966, A photoelastic analysis of stress wave propagation in a layered model: Geophysics: **31**, 881-899.

Rossmanith, H.P. and Shukla, A., 1981, Photoelastic investigation of stress wave diffraction about stationary crack-tips: Journal of the Mechanics and Physics of Solids, **29**, 397-412.

Sicking, C. and Malin, P., 2019, Fracture Seismic: Mapping Subsurface Connectivity: Geosciences, **9**, p.508.

Shih, P.J.R. and Frehner, M., 2016, Laboratory evidence for Krauklis-wave resonance in fractures and implications for seismic coda wave analysis: Geophysics, **81**, 285-293.

Shukla, A. and Prakash, V., 1990, Wave propagation in porous media as a function of fluid saturation: Experimental Mechanics, **30**, 80-87.

Shukla, A., 1991, Dynamic photoelastic studies of wave propagation in granular media: Optics and lasers in engineering, **14**, 165-184.

Smith, C.W., 1980, Photoelasticity in fracture mechanics. Experimental Mechanics, **20**, 390-396.

Tada, H., Paris, P. and Irwin, G., 2000, The analysis of cracks handbook. New York: ASME Press, **2**, 1.

Tang, X. M., and C. H. Cheng, 1988, Wave propagation in a fluid-filled fracture - An experimental study: Geophysical Research Letters, **15**, 1463–1466.

Tercero, C.R., Ikeda, S., Matsushima, M., Fukuda, T. and Negoro, M., 2010, Photoelastic stress analysis error quantification in vasculature models for robot feedback control: IEEE/ASME Transactions on Mechatronics, **15**, 520-526.

Timoshenko, S.P. and Woinowsky-Krieger, S., 1959, Theory of plates and shells. McGraw-hill.

Voloshin, A.S. and Burger, C.P., 1983, Half-fringe photoelasticity: a new approach to whole-field stress analysis: Experimental Mechanics, **23**, 304-313.

Xia, K., Rosakis, A.J. and Kanamori, H., 2004, Laboratory earthquakes: The sub-Rayleigh-to-supershear rupture transition: Science, **303**, 1859-1861.

3 Effect of Geometry and Fluid Viscosity on Dynamics of Fluid-Filled Cracks: Insights from Analogue Experimental Observations

3.1 Abstract

Fluid-filled volumes in geological systems can change the local stress field in the host rock, and may induce brittle deformation as well as fracture propagation. Although the mechanisms relating fluid pressure perturbations and seismicity have been widely studied, the fluid-solid interaction inside the fracture of a host rock is still not well understood. An analogue experimental model of fluid intrusion in fractures between planar layers has been developed to study stress conditions at the margins and tips. A combined high-speed shadowgraph and a photoelasticity imaging system is used to visualize the fluid dynamics and induced stresses on the solid matrix. Cavitation, as well as bubble growth and collapse, occur along the saw-tooth fracture margins, which produces a highly localized stress concentration to initiate new sub-fracture systems. The presence of the bubbles at the fracture tip during fluid pressure perturbation can enhance fracture propagation.

3.2 Plain Language Summary

Fractures serve as important fluid pathways in the crust, so their characteristics and density strongly influence fluid flow. At the same time, fracture properties are also affected by fluid flow, as their dimensions and connectivity might change under pressures from fluids. Many analytical and experimental studies have been conducted to investigate the effect of subsurface flow on fracture dynamics. However, some complexities of fracture geometries and fluid properties, in particular when bubbles are present, remain poorly understood. We developed a laboratory analogue experiment using an optical imaging system to visualize the induced stresses on a fracture. Fluid cavitation and collapse occurs at the margins of a rough fracture boundary are observed. In addition, gas bubbles at fracture tips significantly contribute to the fracture opening. Both observations may help explain fracture propagation in underground geological systems.

3.3 Introduction

Understating the dynamics of magmatic crack growth is crucial for estimating magma transport and eruption precursors. Crack propagation is strongly affected by the stress field caused by the external stress and internal pressure (Sahimi, 2003; Watanabe et al., 2002). Through analytical, numerical and experimental studies, researchers have evaluated various factors that contribute to the dynamics of crack growth in magmatic systems. Such factors include fluid buoyancy (Weertman, 1971a, 1971b, 1973), reservoir pressure (Lister & Kerr, 1991), magma compressibility (Dahm, 2000), pre-existing cracks (Dahi-Taleghani & Olson, 2011; Zhang et al., 2009), fluid viscosity (Heimpel & Olson, 1994), rock heterogeneities (Rivalta et al., 2015), layer rigidities (Kavanagh et al., 2006; Maccaferri et al., 2010; Rivalta et al., 2005), free surface (Rivalta & Dahm, 2006), density gradient (Lister & Kerr, 1991), external stress (Acocella & Tibaldi, 2005; Kervyn et al., 2009; Menand et al., 2010; Watanabe et al., 2002), crack–crack interaction (Ito & Martel, 2002; Takada, 1994), and crack–fault interaction (Le Corvec et al., 2013).

Recently, several works have been published to investigate volatile bubble expansion as a major force to drive the magma movement and intrusion (Carey et al., 2012; Chernov et al., 2014; Lyakhovsky et al., 1996; Navon et al., 1998; Nishimura, 2004; Proussevitch & Sahagian, 1998). However, such phenomena as fluid cavitation, which can trigger shock waves to initiate sub-fractures, is yet to be understood. Cavitation is an important phenomenon, which has been extensively studied in the fluid dynamics, e.g., (Brennen, 2014; Moholkar & Pandit, 1997; Singhal et al., 2002; Zarantonello, 1957; Zwart et al., 2004) and its damages to pipelines and hydraulic systems has been frequently reported (Tijsseling, 1996). Cavitation occurs when the pressure in the fluid phase suddenly drops below its vapor pressure forming a vapor bubble. As the pressure on the fluid phase returns to the original state, the bubble collapses abruptly and, hence, shock waves are generated. When the shock wave reaches the solid surface, it can induce high stress that sometimes exceed the material plastic limit and, thus, cause surface damage. Figure 3-1 shows a possible process for the generation of cavity bubbles and consequent shock waves during dike propagation. In confined systems like geological fractures or pores, the direction of the dike and sill propagation might be deflected or altered due to the localized stress concentration stemming from the sudden bubble collapse (Joseph, 1995).

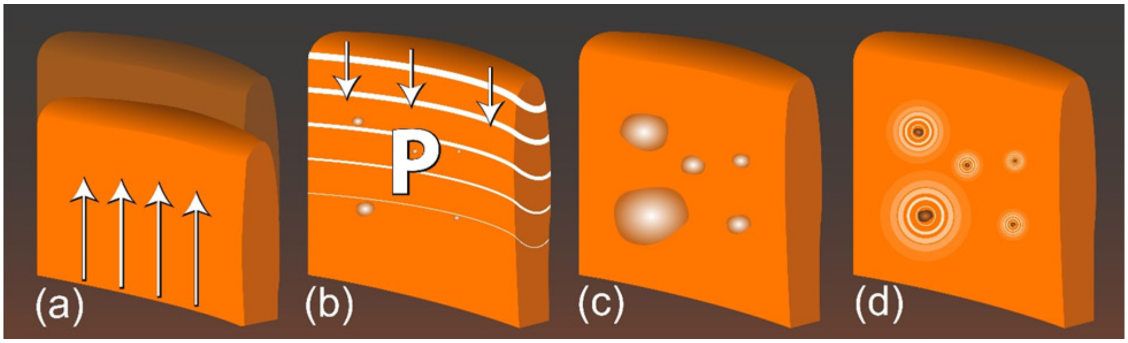

Figure 3-1. Four stages of cavity collapse in a dike. (a) The magma pushes the rock at the tip of the dike. (b) Once the rock is opened, a pressure pulse drop is initiated at the tip and travels down through the dike. The pressure drop creates small cavity bubbles within the dike. (c) The bubbles continue to grow until reaching their maximum sizes, and (d) They collapse quickly, and shock waves are created.

Another important aspect of fluid-driven fractures in geological systems that might affect fracture propagation is the geometry of the fracture and its tip (Desroches et al., 1994; Lenoach, 1995). The shape of the fracture tip influences the stress distribution near the tip and the size of the plastic zone. Therefore, the fluid pressure near the tip region in a fluid-filled fracture varies with respect to the geometry of the tip. This is particularly important since the stress distribution around the fracture highly depends upon the stress condition at the tip, as illustrated in the numerical model of fractures with various geometries, reported by Nilson (1988) and Lecampion et al. (2018). The challenges in modeling fluid-filled fractures include the computational cost and the complexity of mechanisms affecting fracture propagation, which makes their mathematical analyses difficult.

In this experiment, a laboratory analogue experiment is developed to study stress conditions at the margins and tips of two-phase fluid-filled fractures in homogeneous and layered media. We show that fracture geometry and its tip contribute to fracture growth, and that cavitation develops in a fracture with rough margins. Our apparatus visualizes fluid flow and stress distribution on fracture walls simultaneously. Such visualization at the fracture tip and solid-fluid boundary during abrupt pressure changes can improve the current understanding of the dynamic of fracture propagation.

3.4 Method

3.4.1 Experimental Setup

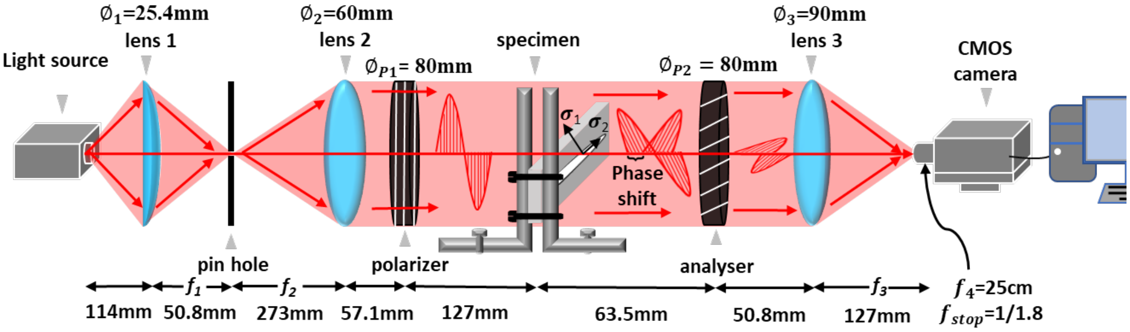

Figure 3-2. Schematic diagram of the combined high-speed shadowgraph imaging system and linear polarizer setup. The specimen is placed between two steel L-shaped support brackets that are mounted on an optical table. Ø is the lens diameter and *f* the focal length. σ_1 and σ_2 are principal stresses of the sample.

A linear (planar) polariscope is used to visualize the dynamics of the liquid-solid interaction in the filled fractures, subject to a pulse pressure wave originated in the liquid phase; see Figure 3-2 for more details. The polariscope measures simultaneously the stress wave velocity on the fracture wall and visualizes the fluid dynamics. The polariscope can be divided into three parts: a collimated light, also known as shadowgraph system; two linear light polarizers, and a high-speed camera. The light collimation was achieved using a 150W 21V halogen light source, followed by a focusing lens with a focal length of 50.8 mm and a diameter of 25.4 mm, a pinhole and two collimated lenses of focal lengths of 273 mm and 127 mm, respectively. Two linear polarizers were used to polarize light in a preferred direction, confined to a single plane of oscillation, while all other light oscillation directions are absorbed by the polarizer. When a pair of polarizers are set at orthogonal angle (90 degrees), no light is transmitted through. Some transparent materials, such as polycarbonate, are photoelastic, meaning that when they are under applied stress, they become optically anisotropic (also called birefringent in the literature) and, hence, light is polarized along the two principal stress directions of the sample. Phase shift of the light rays due to the birefringence is proportional to the applied stress (Tada et al., 2000). If we place the photoelastic material between the two orthogonal polarizers, there will be no orthogonally polarized light until the material is stressed and, thus, we can qualitatively infer the stress level at each point of the sample under load based on the light passing through the system. The fringe envelope that we observe from the linear polariscope is the superposition of the isochromatic and isoclinic fringes. A high-speed camera capable of recording up to 250,000 frames per second (fps) is used to capture the dynamic state of stress in the material, induced by a pressure wave in the liquid phase. In this study we chose to record at 10,000 fps in order to increase the resolution of the individual frames. The high-speed camera was triggered electronically with controlled delay times for taking specific image sequences out of the overall fluid motion.

3.4.2 Analogue Fracture – Trilayer Model

Table 3-1. Six Experiments to Visualize the Fluid-Filled Fracture Dynamics

Experiment	Fracture model	Fluid type
1	Flat	water
2	Saw-tooth	water
3	Saw-tooth	viscous fluid
4	Flat, single narrow tip	water
5	Flat, double narrow tip	water
6	Flat, triangle tip	water

The experimental apparatus was used to visualize the solid-fluid interactions along the fracture main body and at the fracture tips in the following six trilayer models (Table 3-1. Six Experiments to Visualize the Fluid-Filled Fracture Dynamics), each consisting of two photoelastic insensitive acrylic plates and one photoelastic sensitive polycarbonate plate, as shown in Figure 3-3(a). This trilayer fracture model is developed to analogue the sill intrusion where the liquid intrude between parallel geological layers The density of the acrylic is 1190 kg/m^3, with V_p = 2710 m/s and V_s = 1391 m/s, while that of the polycarbonate is 1190 kg/m^3, with V_p = 2106 m/s and V_s = 931 m/s. The two acrylic layers are 152.4×47.6×1.58 mm in size, whereas the polycarbonate plate has a dimension of 152.4×47.6×0.79 mm. The reason we adopt a thinner polycarbonate plate is based on the stress-optic law (Tada, et al., 2000) stating that thinner photoelastic materials possess higher photoelastic sensitivity and, thus, smaller external stress is required to generate photoelastic fringes:

$$\sigma = \frac{N f_\sigma}{h} \qquad (1)$$

where f_σ is a constant material fringe, N is the fringe order that depends on relative retardation, and h is the specimen's thickness.

The three layers are held together by two 5 mm thick aluminum plates and clamped by bolts along the plates' edges (Figure 3-3a). Fractures were machined in the middle acrylic layer. The reference fracture has flat boundaries (sides) with semi-cylindrical tips, as shown in Figure 3-3(b), which was used to study solid-fluid interaction and stress propagation on a smooth fracture surface. The second fracture geometry consists of the same size channel and tips; its boundaries (sides) have, however, a saw-tooth pattern where the bottom and height of a triangle is 0.6 and 0.3 cm, respectively, as shown in Figure 3-3(c). The saw-tooth fracture wall is common in models of fracture morphology that has been used to study fracture toughness and fatigue strength (Carpinteri et al., 2019). This saw-tooth fracture was used as an analogue to study the effect of an irregular fracture surface on the stress propagation.

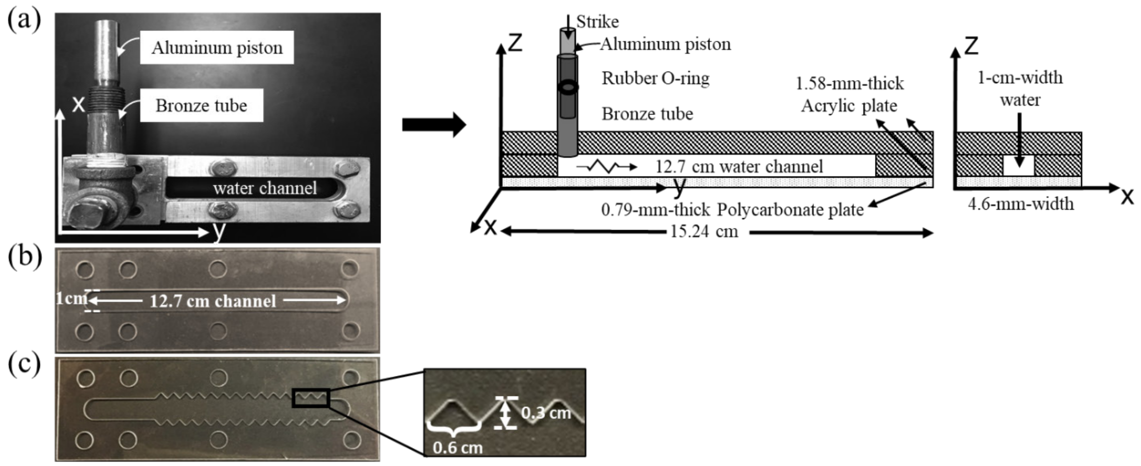

Figure 3-3. (a) The trilayer model and its schematic side view, which consists of one polycarbonate and two acrylic plates, fastened by two aluminum plates. The pressure pulse is produced by applying a sudden load to the aluminum piston. (b) Flat fracture model in the middle layer used as a reference. (c) Saw-tooth fracture model and enlarged details of its geometry. The circles along the edges of plates are the locations for clamping bolts.

Additionally, three types of fracture tips were designed to study the fluid-filled fracture dynamics in its plastic zone: single narrow tip, double parallel narrow tips, and a triangular tip, as shown in Figure 3-4(a), 3(b), and 3(c), respectively. The three fracture models are also made of acrylic in which the dimensions of the main channels are the same as that of the reference flat fracture model. The single narrow and triangle tips shown in Figure 3-4(a) and 1(c), were proposed by Pelloux (1970) and Bowles and Schijve (1983) to study the effect of fatigue in fractures grown for different fracture tip geometries. The double narrow tips in Figure 3-4(b) were analyzed to study bifurcation performance of a complex fracture network in hydraulic fracturing, based on the fractal geometry (Zhou et al., 2017). The analogue fracture model was filled with distilled water. An experimental test was initiated by striking the aluminum piston held by a bronze tube, located at one end of the fracture in Figure 3-4(a). The impulse on the piston triggers a pressure wave in the liquid phase. The pressure pulse propagates through the confined liquid in the fracture and reflects back and forth until it dissipates.

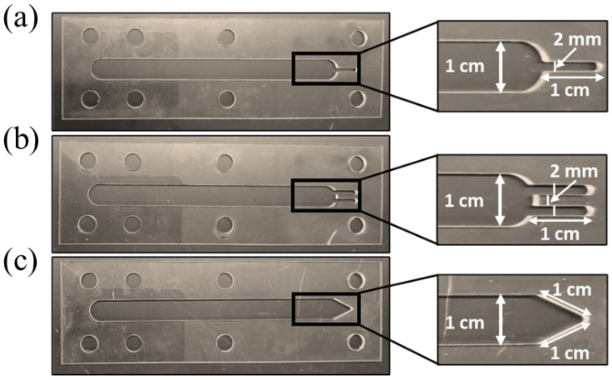

Figure 3-4. The fracture models used to study the fluid-filled fracture dynamics in the plastic zone. (a) Single narrow tip with 1 cm length and 2 mm width. (b) Double narrow tips with 1 cm length and 2 mm width each. (c) Triangle tip with 1 cm side length. In fracture propagation linear elasticity is valid far from the tip, it breaks down near the tip, where one has a highly nonlinear plastic zone.

3.5 Experimental Results

We utilize the reference fracture to investigate how the liquid pressure wave is transferred to the solid walls of the fracture. The stress wave on the fracture walls manifests itself as bright patterns, also known as photoelastic fringes, traveling from one end of the fracture to the other along the solid-fluid interface (Figure 3-5). Due to the limited stress transferred from the stress wave to the polycarbonate plate, the fringe pattern does not manifest a number of well separated fringes. The velocity of the overall envelope of the stress wave's amplitude (group velocity), measured based on the location of peak pixel intensity of the photoelastic fringes, was 33.95m/s. Such wave speed in fluid-driven fractures are commonly observed during hydraulic fracturing and in volcanic tremors known as crack waves (Aki et al., 1977; Chouet, 1986; Lipovsky & Dunham, 2015).

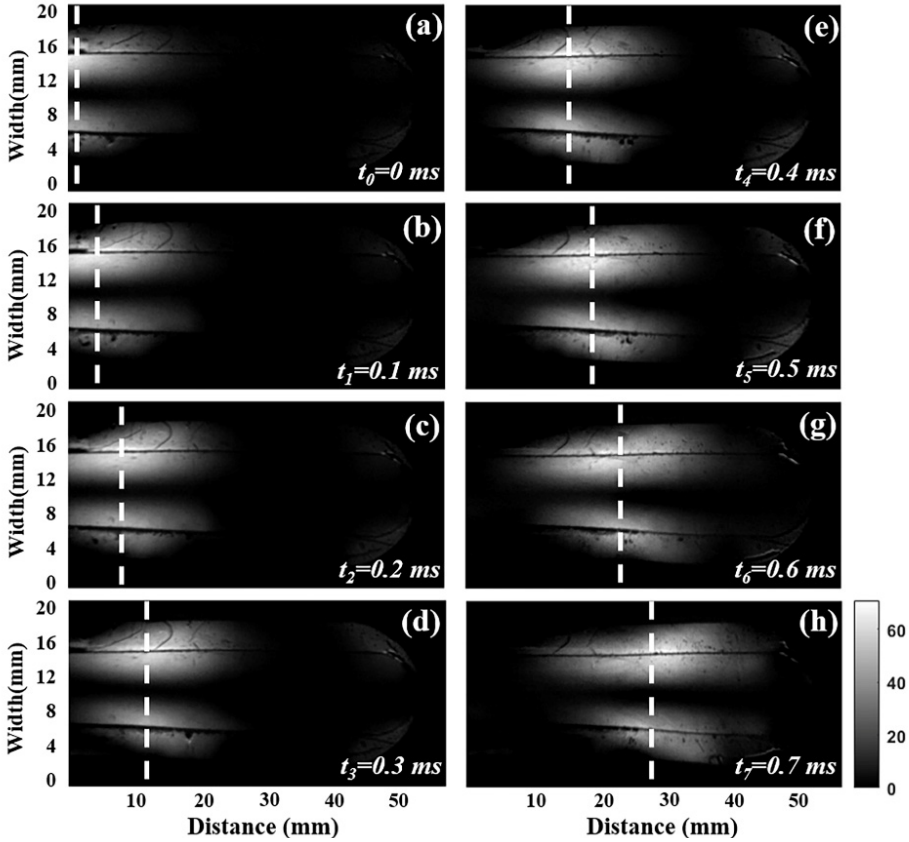

Figure 3-5. The photoelastic image of the reference smooth flat fracture used to show the solid-fluid interaction due to the input pressure pulse on the liquid phase under no surface irregularities. The bright dashed line trend represents direction of the stress wave propagation, which is the result of the photoelastic effect on the polycarbonate layer. The bright patterns near the crack tip are due to the residual stress, caused by clamping bolts. The color bar shows the pixel intensity value of the images. Stressed area is in white and unstress is in black.

In contrast to the idealized smooth fracture surface, experiments considering a fracture with saw-tooth surface representative of fracture surface roughness were conducted. the most striking difference between the smooth and saw- tooth fracture models is the appearance of cavitation in the latter (Figure 3-6). We repeated this experiment three times, each of which produced the cavitation phenomenon. Figure 3-6(h) shows how the pixel values variation at a location in the saw-tooth fracture indicates by the arrow in Figure 3-6 during the cavitation process. The pixel values are qualitatively related to the stress, as a higher pixel value implies greater stress. We observed that before the bubble initiation, there was no photoelastic fringes, meaning no wave-induced stress on the saw-tooth. The images in Figure 3-6 were acquired after the crack wave had decayed so that by 0 ms at T_0 the crack wave-induced strain had diminished. Therefore, the pressure on the liquid decreased and the small-scale bubbles began to expand, photoelastic fringes appeared at the fracture surface. This implies that the fracture surface is subjected to an intense increase in the tensile stress due to the bubble expansion from 0 to around 1.9 ms. The emergence of cavitation might be due to the shape of the solid-liquid interface and can induce surface self-degradation. The initiation of cavitation bubbles within liquid requires the presence of nuclei that in our system can stem from dissolved gases. As the pressure wave in the liquid phase advances, it reaches a peak value and, then, starts to decrease. As the pressure decreases below a certain threshold, the microscopic air bubble due to the dissolved gases expand and bubbles emerge. Then, as the pressure in the liquid increases again, the bubbles collapse violently from around 17.5 to 18 ms, which initiates local shock waves. At the emergence of the bubbles, the stress at the fracture surface increases reaching a maximum. This intense stress increase due to cavitation at saw-tooth fracture surface did not develop at the smooth fracture's wall. The valley of the saw-tooth seems to be of importance to the bubble growth, enhancing the formation of large bubbles and generating a state of stress on the fracture wall. During the bubble collapse, on the other hand, the pressure in the fluid recovers and the associated tensile stress on the fracture surface disappears after 18 ms.

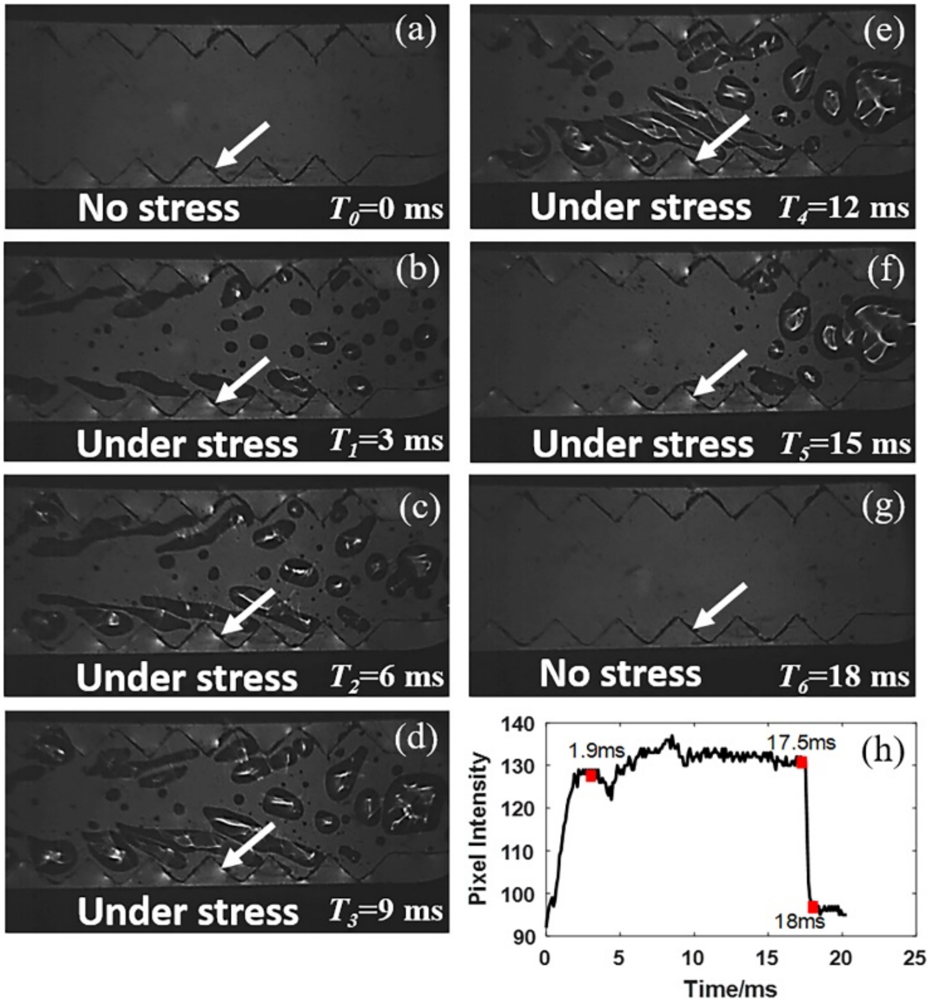

Figure 3-6. Image sequence of the bubbles expansion and collapse for the saw-tooth fracture model. (a) Before the bubble initiation, there is no stress on the saw-tooth. (b-f) As the pressure on the liquid decreases, the small-scale bubbles expand and photoelastic fringes (bright patterns) appear on the fracture surface, implying that the fracture surface is subjected to a tensile stress due to the bubble expansion. (g) The photoelastic fringes and the associated stress on the fracture surface disappear after the pressure in the fluid recovered. (h) The tracked pixel brightness intensity at the saw-tooth location indicated by white arrow in (a-g). This cavitation phenomenon was not observed in the reference fracture in Figure 3-5.

To investigate the effect of viscosity on cavitation, we used transparent viscous shampoo as the crack fluid in the saw-tooth fracture. Note that the shampoo viscosity is 10^3-10^4 higher than water viscosity (1 mPa·s) at room according to AlQuadeib et al (2018). Galland et al. (2006) conducted an analogue experiment to study the low-viscosity basaltic magma intrusion in crust using vegetable oil whose dynamic viscosity is around 20 mPa·s. While most highly mobile magma should have a viscosity ranging from 4×10^{-6} to 75,000 mPa·s (Galland et al., 2006). Figure 3-7 shows the stress wave traveling along the saw tooth fracture filled with shampoo. The stress wave velocity measured in Figure 3-7 is 28.3 m/s which is slightly smaller compared to the wave velocity 33.95m/s in Figure 3-6 due to the viscous effect. No cavitation is observed because the increase of viscosity enhances the intermolecular forces within the fluid and thus prevent the cavitation (Vernès et al., 2020).

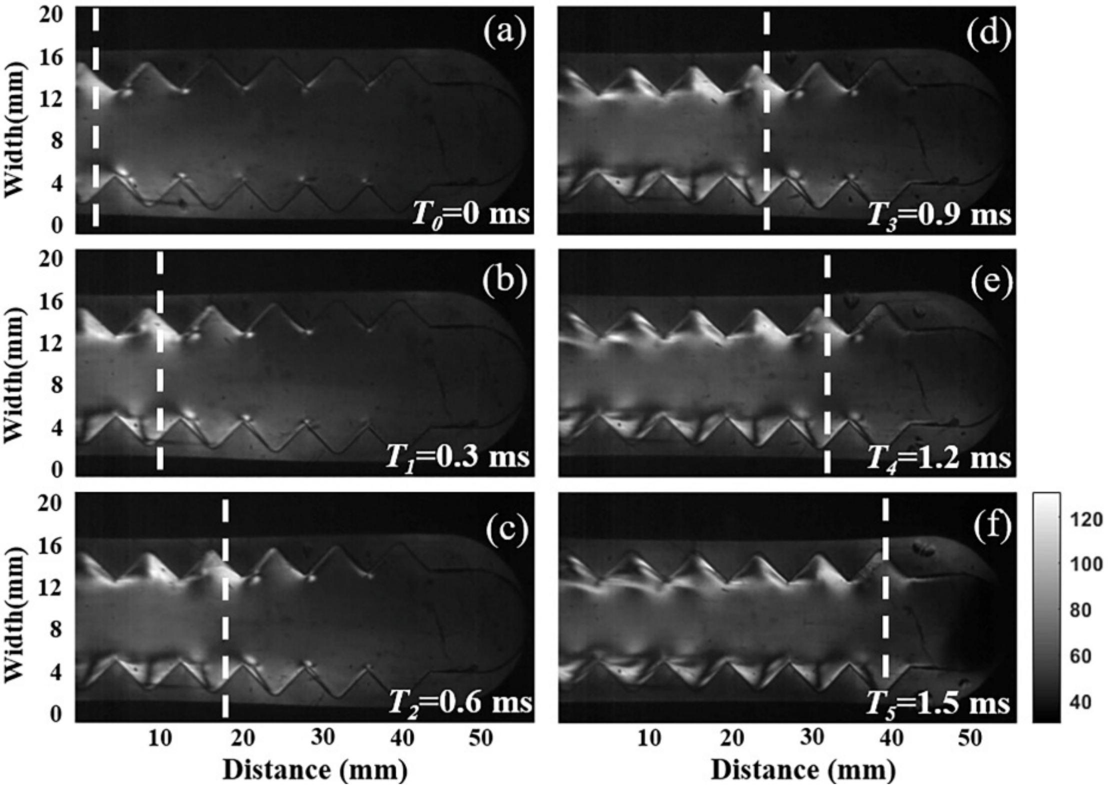

Figure 3-7. The photoelastic images of the stress wave propagation in the saw-tooth fracture filled with shampoo. The bright dashed line trend represents direction of the stress wave propagation as in Figure 3-5. Cavitation phenomenon is not observed in this shampoo filled fracture.

Apart from the expansion and collapse of the bubbles due to the cavitation phenomenon that is likely to produce sub-fractures along solid boundaries, the bubbles can enhance the opening and propagation of fractures through other mechanisms acting at the crack tip. The pressure distribution at the tip of a fracture is a key factor for controlling fracture propagation. For example, in some deep geothermal systems, it is widely accepted that the fracture tip is occupied by magmatic volatiles (Garagash & Detournay, 2000; Rubin, 1993). The typical analytical methods to compute the stress field surrounding the fracture tip are based on solving a system of coupled equations for the elastic deformation of the host rock and the viscous fluid flow within the fracture. However, the behavior of the fracture tip is much more complex due to its geometry (Paskin et al., 1985; Zhou et al., 2017).

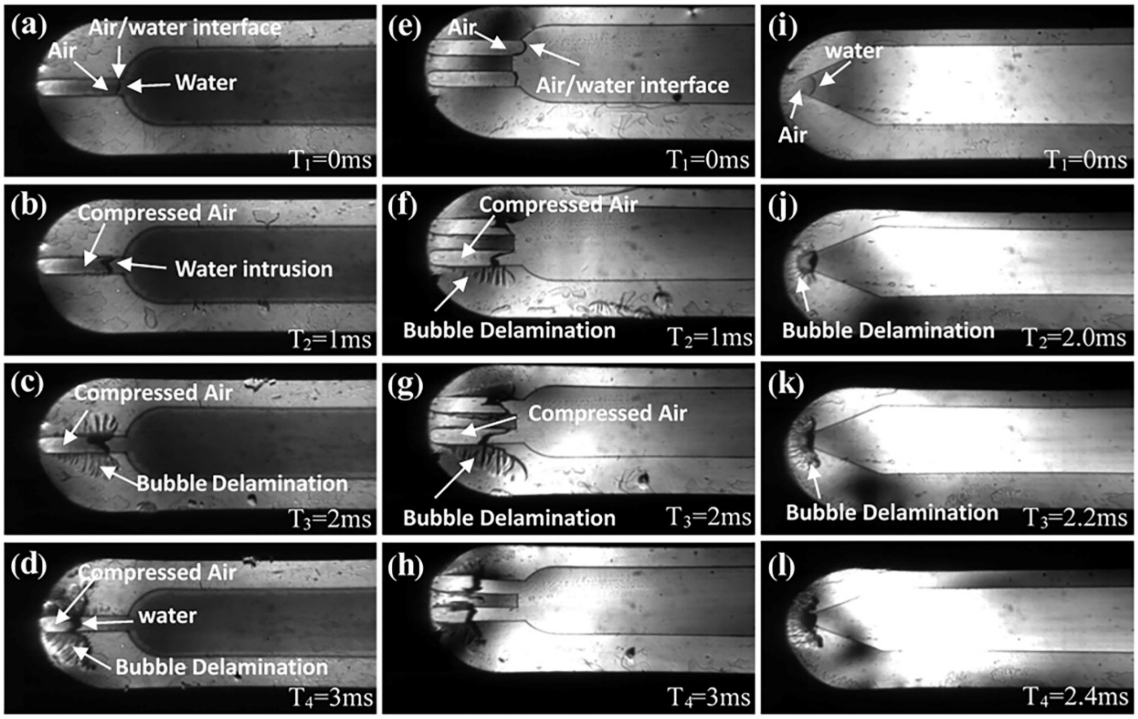

Figure 3-8. The image sequences the process of bubbles emergence at the fracture tip. These narrow fracture tips were purposely not filled with water to mimic trapped bubbles. The pressure wave in the fluid phase forces the bubble to intrude into the tip, forcing a delamination of the layers of the trilayer model.

In order to investigate and visualize the fracturing behavior at the tips for complex geometries when the bubbles are present, the three aforementioned fracture models were used, shown in Figure 3-4(a-c). The tips were purposely not completely filled with water in order to mimic the trapped gas. When the pressure pulse travels through the liquid phase, it compresses and pushes the trapped bubbles forward into the tips. As the bubble pressure increases, the stress on the tip also increases and causes a deformation that resembles a fracture opening and the propagation scenario shown in Figure 3-8. For the single narrow tip in Figure 3-8(a-d), the pressure wave in the fluid phase forces the bubble to intrude into the tip that creates delamination of the layers of the trilayers model (Figure 3-8c, d). This process is dominated by a wedge-like delamination where the largest opening happens at the gas-fluid interface (Figure 3-8c). As the liquid pressure keeps pushing and compressing the bubble, the delamination keeps moving forward together with the bubble, leaving behind some smaller bubbles trapped in between the delaminated layers. This is particularly important because if solid particles were present, they could become trapped between the layers, effectively forcing fracture expansion and propagation. The double narrow fracture tip case shown in Figure 3-8(e-h) shows similar dynamics as the single narrow tip, except that the extent of delamination and, therefore, tip expansion and propagation are significantly enhanced, as indicated by the large lateral opening trailing behind the intruded fluid in Figure 3-8(g).

In the model with the triangular tip, on the other hand, the delamination effect due to the bubble being compressed and pushed by the liquid interface is the least severe of the three cases. This is shown in Figure 3-8(i-l). We attribute this to two factors related to the bubbles. First, the size of the bubble is smaller than in the previous cases, which leads to a lower compressed volume and smaller stress on the tip bubble-solid interface. Second, the triangular shape induces a gradual compression of the bubble as the menisci moves forward, as compared with the piston-like compression of the previous two cases, resulting in a maximum compression when the bubble is reduced to the very end of the tip. This gradual compression is then followed by burst of the bubble through the delaminated layers, as seen in Figure 3-8(k) and Figure 3-8(l). It is important to note that if the bubbles had not been there, the delamination of the trilayer model representing a fracture opening and propagation would not have happened. The gas compression provides the necessary stress concentration to initiate this process.

3.6 Discussion

Here, we present the effects of the geometry of fracture wall (i.e., roughness) and tip on the fracture mechanics of fluid-filled fractures using analogue models. We observed that in a fracture with a rough interface, bubble cavitation occurs when a transient stress passes through, and collapses after an analogue injection. The cavitation yields an extra intense tensile stress on the fracture wall. Because shock waves are commonly generated during bubble collapse within a very short time (in the 10^{-6} second time scale), they can potentially provide sufficient energy to create new sub-fractures (Supponen et al., 2017). Thus, we conclude that not only the state of the stress within the fracture, but also fracture roughness contribute to fracture opening and delamination. The restrictions for capturing the shock waves include the limited number of frames per second (10000 fps in our experiment) captured by the digital camera, and light source. In other words, a more capable digital camera and a stronger light source (laser) that could allow enough light crossing through the sample would be needed for a better resolution of the shock wave.

The fracture in the trilayer model is machined in the brittle acrylic plate which is an isotropic and linear elastic material for which typically linear elastic fracture mechanics (LEFM) is valid except in the small area in vicinity of the crack tip (plastic zone). However, the plastic zone size at the tip can be estimated approximately as (Irwin, 1968):

$$R = \left(\frac{1}{2\pi}\right)\left(\frac{K_{IC}}{\sigma_{ys}}\right)^2 \qquad (2)$$

where the typical critical stress intensity factor K_{Ic} and yield stress σ_{ys} of acrylic is 1.5 MPa·m$^{0.5}$ (Efimov & Sher, 2001) and 64.8 MPa respectively and R is the radial distance ahead of the crack tip.

From equation 2, the plastic zone radius is 0.08 mm which is much smaller compared to the size of the fracture in our case exhibiting the small-scale yielding at the crack tip, therefore LEFM is still applicable if no bubble effect occurs at the crack tip as shown in Figure 3-4. This plastic zone relieves high stress from the fracturing fluid which results in the difficulty in fracturing.

Compared to the fracture length, the polycarbonate used in our experiment were thin, implying the plane stress condition. The typical critical stress intensity factor $\mathrm{K_{Ic}}$ and yield stress σ_{ys} of polycarbonate is 2.24 MPa·m$^{0.5}$ and 68 MPa, respectively (Williams, 1977). According to Brown and Srawley (1966), the critical thickness $\mathrm{T_c}$ of polycarbonate plate for plane stress is given by:

$$\mathrm{T_c} \leq 2.5\left(\frac{\mathrm{K_{Ic}}}{\sigma_{\mathrm{ys}}}\right)^2 \qquad (3)$$

Thus, a thickness less than 3 mm is considered as plane-stress condition. This explains the discrepancy between our measured crack wave group velocity of 33.95 m/s and the theoretical velocity using the formulation of Lipovsky and Dunham (2015), who assumed an idealized plane-strain condition. In addition, the presence of the free surface can partly account for a lower perturbation of the group velocity. Korneev et al. (2014) derived a formula for the velocity of the crack waves from which a velocity of crack wave propagating within such a fluid-filled trilayer is lower than that in the plane-strain condition.

Note that the entire clamped trilayer model may be regarded as real fractures in nature of low conductivity or closed fractures. The reopening of the closed fracture is by the process of delamination of the tight layers, due to the pressure wave and the presence of bubble at the fracture tip.

3.7 Conclusion

An analogue experimental setup combining two distinct optical techniques, shadowgraphy and photoelasticity, were used to visualize the fluid-solid interaction inside fractures with different types of fracture surfaces and tips. Among the most important and striking finding was the occurrence of cavitation when the fracture surface wall has a saw-tooth shape. This phenomenon can be an important mechanism that leads to the fracture surface degradation and growth. The two main causes for the fracture surface degradation and growth are, first, the expansion of the bubbles that causes the tensile stress on the fracture wall to increase and, second, the collapse of the bubble generates a shock wave, which was not observed in our experiment because, generally, shock wave occur very fast and, thus, it is impossible to capture using the current setup. We also note that higher fluid viscosity prevents the formation of cavity bubbles. These findings could be used to explain the possibility of cavitation during the magma propagation. If magma has considerable dissolved gases, i.e., lower viscosity, it is more susceptible to generate cavity bubbles. On the other hand, for magma with a limited amount of dissolved gases, i.e., higher viscosity, cavitation will be unlikely.

While we have focused on magmatic systems, the results are also applicable to other fluid-filled crack systems. The fluid injection in hydraulic fracturing and wastewater disposal or fluid intrusion in natural geothermal systems could also form bubbles that consequently open fractures. The bubbles that can be formed could consequently move to fracture tips and lead to the formation of new fractures. The same analogue experimental setup was used to study the effects of bubbles at the fracture tip using various tip geometries. The pressure wave in the liquid phase compresses and pushes forward the trapped bubbles into the tips. The tensile stress induced by the bubbles at the fracture tip increase as the bubble pressure increases. The rate of strain energy release at the fracture tip increases significantly due to the presence of bubbles, which induce tensile stress. The energy produced by the bubbles overcomes the resistance of the trilayer that results in its delamination, which resembles a fracture opening and propagation. The effect of the bubble effect on the fluid-filled fractures plays an important role in fracture propagation, which should be incorporated in theoretical models to supplement the linear elastic fracture mechanics in the studies of fracture behavior.

3.8 Acknowledgements and Data

The data and related material of this paper are accessible at https://openei.org/datasets/dataset/8aadda44-f712-4f16-a09e-999dc91152fa/resource/d321f63b-b2c6-4735-b8fb-6cde9c10c308/download/data.7z

3.9 Reference

Acocella, V., & Tibaldi, A. (2005). Dike propagation driven by volcano collapse: a general model tested at Stromboli, Italy. *Geophysical Research Letters, 32*(8).

Aki, K., Fehler, M., & Das, S. (1977). Source mechanism of volcanic tremor: Fluid-driven crack models and their application to the 1963 Kilauea eruption. *Journal of Volcanology and Geothermal Research, 2*(3), 259-287.

AlQuadeib, B. T., Eltahir, E. K., Banafa, R. A., & Al-Hadhairi, L. A. (2018). Pharmaceutical evaluation of different shampoo brands in local Saudi market. *Saudi pharmaceutical journal, 26*(1), 98-106.

Bowles, C., & Schijve, J. (1983). Crack tip geometry for fatigue cracks grown in air and vacuum. In *Fatigue Mechanisms: Advances in Quantitative Measurement of Physical Damage*: ASTM International.

Brennen, C. E. (2014). *Cavitation and bubble dynamics*: Cambridge University Press.

Brown, W., & Srawley, J. (1966). Plane strain crack toughness testing of high strength metallic materials. In *Plane strain crack toughness testing of high strength metallic materials*: ASTM International.

Carey, R. J., Manga, M., Degruyter, W., Swanson, D., Houghton, B., Orr, T., & Patrick, M. (2012). Externally triggered renewed bubble nucleation in basaltic magma: The 12 October 2008 eruption at Halema ‘uma ‘u Overlook vent, Kīlauea, Hawai ‘i, USA. Journal of Geophysical Research: Solid Earth, 117(B11).

Carpinteri, A., Spagnoli, A., & Terzano, M. (2019). Crack morphology models for fracture toughness and fatigue strength analysis. *Fatigue & Fracture of Engineering Materials & Structures, 42*(9), 1965-1979.

Chouet, B. (1986). Dynamics of a fluid-driven crack in three dimensions by the finite difference method. *Journal of Geophysical Research: Solid Earth, 91*(B14), 13967-13992.

Chernov, A., Kedrinsky, V., & Pil'nik, A. (2014). Kinetics of gas bubble nucleation and growth in magmatic melt at its rapid decompression. Physics of Fluids, 26(11), 116602.

Dahi-Taleghani, A., & Olson, J. E. (2011). Numerical modeling of multistranded-hydraulic-fracture propagation: accounting for the interaction between induced and natural fractures. *SPE journal, 16*(03), 575-581.

Dahm, T. (2000). Numerical simulations of the propagation path and the arrest of fluid-filled fractures in the Earth. *Geophysical Journal International, 141*(3), 623-638.

Davydov, M., Kedrinskii, V., Chernov, A., & Takayama, K. (2005). Generation and evolution of cavitation in magma under dynamic unloading. *Journal of Applied Mechanics and Technical Physics, 46*(2), 208-215.

Desroches, J., Detournay, E., Lenoach, B., Papanastasiou, P., Pearson, J. R. A., Thiercelin, M., & Cheng, A. (1994). *The crack tip region in hydraulic fracturing.* Paper presented at the Proceedings of the Royal Society of London. Series A: Mathematical and Physical Sciences.

Efimov, V., & Sher, E. (2001). Dynamic crack resistance of acrylic plastic. *Journal of Applied Mechanics and Technical Physics, 42*(5), 918-924.

Galland, O., Cobbold, P. R., Hallot, E., de Bremond d'Ars, J., & Delavaud, G. (2006). Use of vegetable oil and silica powder for scale modelling of magmatic intrusion in a deforming brittle crust. *Earth and Planetary Science Letters, 243*(3-4), 786-804.

Garagash, D., & Detournay, E. (2000). The tip region of a fluid-driven fracture in an elastic medium. *J. Appl. Mech., 67*(1), 183-192.

Heimpel, M., & Olson, P. (1994). Buoyancy-driven fracture and magma transport through the lithosphere: models and experiments. In *International Geophysics* (Vol. 57, pp. 223-240): Elsevier.

Irwin, G. (1968). Linear fracture mechanics, fracture transition, and fracture control. *Engineering Fracture Mechanics, 1*(2), 241-257.

Ito, G., & Martel, S. J. (2002). Focusing of magma in the upper mantle through dike interaction. *Journal of Geophysical Research: Solid Earth, 107*(B10), ECV 6-1-ECV 6-17.

Joseph, D. D. (1995). Cavitation in a flowing liquid. *Physical Review E, 51*(3), R1649.

Kavanagh, J. L., Menand, T., & Sparks, R. S. J. (2006). An experimental investigation of sill formation and propagation in layered elastic media. *Earth and Planetary Science Letters, 245*(3-4), 799-813.

Kervyn, M., Ernst, G., van Wyk de Vries, B., Mathieu, L., & Jacobs, P. (2009). Volcano load control on dyke propagation and vent distribution: Insights from analogue modeling. *Journal of Geophysical Research: Solid Earth, 114*(B3).

Korneev, V., Danilovskaya, L., Nakagawa, S., & Moridis, G. (2014). Krauklis wave in a trilayer. *Geophysics, 79*(4), L33-L39.

Le Corvec, N., Menand, T., & Lindsay, J. (2013). Interaction of ascending magma with pre-existing crustal fractures in monogenetic basaltic volcanism: an experimental approach. *Journal of Geophysical Research: Solid Earth, 118*(3), 968-984.

Lecampion, B., Bunger, A., & Zhang, X. (2018). Numerical methods for hydraulic fracture propagation: a review of recent trends. *Journal of natural gas science and engineering, 49*, 66-83.

Lenoach, B. (1995). The crack tip solution for hydraulic fracturing in a permeable solid. *Journal of the Mechanics and Physics of Solids, 43*(7), 1025-1043.

Lipovsky, B. P., & Dunham, E. M. (2015). Vibrational modes of hydraulic fractures: Inference of fracture geometry from resonant frequencies and attenuation. *Journal of Geophysical Research: Solid Earth, 120*(2), 1080-1107.

Lister, J. R., & Kerr, R. C. (1991). Fluid-mechanical models of crack propagation and their application to magma transport in dykes. *Journal of Geophysical Research: Solid Earth, 96*(B6), 10049-10077.

Lyakhovsky, V., Hurwitz, S., & Navon, O. (1996). Bubble growth in rhyolitic melts: experimental and numerical investigation. Bulletin of Volcanology, 58(1), 19-32.

Maccaferri, F., Bonafede, M., & Rivalta, E. (2010). A numerical model of dyke propagation in layered elastic media. *Geophysical Journal International, 180*(3), 1107-1123.

Menand, T., Daniels, K., & Benghiat, P. (2010). Dyke propagation and sill formation in a compressive tectonic environment. *Journal of Geophysical Research: Solid Earth, 115*(B8).

Moholkar, V. S., & Pandit, A. B. (1997). Bubble behavior in hydrodynamic cavitation: effect of turbulence. *AIChE Journal, 43*(6), 1641-1648.

Navon, O., Chekhmir, A., & Lyakhovsky, V. (1998). Bubble growth in highly viscous melts: theory, experiments, and autoexplosivity of dome lavas. Earth and Planetary Science Letters, 160(3-4), 763-776.

Nilson, R. (1988). Similarity solutions for wedge-shaped hydraulic fractures driven into a permeable medium by a constant inlet pressure. *International Journal for Numerical and Analytical Methods in Geomechanics, 12*(5), 477-495.

Nishimura, T. (2004). Pressure recovery in magma due to bubble growth. Geophysical Research Letters, 31(12).

Paskin, A., Massoumzadeh, B., Shukla, K., Sieradzki, K., & Dienes, G. (1985). Effect of atomic crack tip geometry on local stresses. *Acta Metallurgica, 33*(11), 1987-1996.

Pelloux, R. M. N. (1970). Crack extension by alternating shear. *Engineering Fracture Mechanics, 1*(4), 697-704.

Proussevitch, A., & Sahagian, D. L. (1998). Dynamics and energetics of bubble growth in magmas: Analytical formulation and numerical modeling. *Journal of Geophysical Research: Solid Earth, 103*(B8), 18223-18251.

Rivalta, E., Böttinger, M., & Dahm, T. (2005). Buoyancy-driven fracture ascent: Experiments in layered gelatine. *Journal of Volcanology and Geothermal Research, 144*(1-4), 273-285.

Rivalta, E., & Dahm, T. (2006). Acceleration of buoyancy-driven fractures and magmatic dikes beneath the free surface. *Geophysical Journal International, 166*(3), 1424-1439.

Rivalta, E., Taisne, B., Bunger, A., & Katz, R. (2015). A review of mechanical models of dike propagation: Schools of thought, results and future directions. *Tectonophysics, 638*, 1-42.

Rubin, A. M. (1993). On the thermal viability of dikes leaving magma chambers. *Geophysical Research Letters, 20*(4), 257-260.

Sahimi, M. (2003). *Heterogeneous Materials: Nonlinear and breakdown properties and atomistic modeling* (Vol. 2): Springer Science & Business Media.

Singhal, A. K., Athavale, M. M., Li, H., & Jiang, Y. (2002). Mathematical basis and validation of the full cavitation model. *J. Fluids Eng., 124*(3), 617-624.

Supponen, O., Obreschkow, D., Kobel, P., Tinguely, M., Dorsaz, N., & Farhat, M. (2017). Shock waves from nonspherical cavitation bubbles. *Physical Review Fluids, 2*(9), 093601.

Tada, H., Paris, P., & Irwin, G. (2000). The analysis of cracks handbook. *New York: ASME Press, 2*, 1.

Takada, A. (1994). Development of a subvolcanic structure by the interaction of liquid-filled cracks. *Journal of Volcanology and Geothermal Research, 61*(3-4), 207-224.

Tijsseling, A. (1996). Fluid-structure interaction in liquid-filled pipe systems: a review. *Journal of Fluids and Structures, 10*(2), 109-146.

Vernès, L., Vian, M., & Chemat, F. (2020). Ultrasound and Microwave as Green Tools for Solid-Liquid Extraction. In *Liquid-Phase Extraction* (pp. 355-374): Elsevier.

Watanabe, T., Masuyama, T., Nagaoka, K., & Tahara, T. (2002). Analog experiments on magma-filled cracks. *Earth, planets and space, 54*(12), 1247-1261.

Weertman, J. (1971a). Theory of water-filled crevasses in glaciers applied to vertical magma transport beneath oceanic ridges. *Journal of Geophysical Research, 76*(5), 1171-1183.

Weertman, J. (1971b). Velocity at which liquid-filled cracks move in the Earth's crust or in glaciers. *Journal of Geophysical Research, 76*(35), 8544-8553.

Weertman, J. (1973). Can a water-filled crevasse reach the bottom surface of a glacier. *IASH publ, 95*, 139-145.

Williams, J. (1977). Fracture mechanics of polymers. *Polymer Engineering & Science, 17*(3), 144-149.

Zarantonello, E. H. (1957). *Jets, wakes, and cavities*: Academic Press.

Zhang, X., Jeffrey, R. G., & Thiercelin, M. (2009). Mechanics of fluid-driven fracture growth in naturally fractured reservoirs with simple network geometries. *Journal of Geophysical Research: Solid Earth, 114*(B12).

Zhou, Z., Su, Y., Wang, W., & Yan, Y. (2017). Application of the fractal geometry theory on fracture network simulation. *Journal of Petroleum Exploration and Production Technology, 7*(2), 487-496.

Zwart, P. J., Gerber, A. G., & Belamri, T. (2004). *A two-phase flow model for predicting cavitation dynamics.* Paper presented at the Fifth international conference on multiphase flow, Yokohama, Japan.

4 Laboratory Measurements of the Impact of Fracture and Fluid Properties on the Propagation of Krauklis Waves

4.1 Abstract

Krauklis waves are commonly observed in fluid filled fractures and are considered to be a tool to study the physical properties of fractures due to their strong dispersion and resonant vibration natures. By analyzing the resonant frequency and quality factor of the seismic signals, the fracture dimension and fluid properties can be estimated. However, the accuracy of those estimations is highly depended on the many factors which have not been well studied. In this paper, we conducted laboratory experiments using a piezoelectric source (dominant frequency 1000 Hz) and miniature pressure transducers to investigate Krauklis wave propagation inside an a trilayer model that consists of two aluminum plates and a fluid layer in middle. We vary the fracture thickness from 1.5, 2.5, 4.5, and 8.5 mm for fracture with length of 30.38 mm to mimic the fracture opening process in different stages. In addition, we extend the fracture of two parallel plates to more complex and realistic fracture by modifying the fracture stiffness, saturated fluid and fracture geometry and fracture surface roughness. We observed that the phase velocity, resonant frequencies and quality factors: (1) increase with the increase of the fracture thickness; (2) decrease with the increase of the fluid viscosity; (3) decrease with the increase of mechanical compliance. In addition, an increase in the roughness of fracture surface and a change from

a rectangular to wedge shaped fracture both result in decreased phase velocity and resonant frequencies.

4.2 Introduction

Most of the seismicity worldwide stems from the brittle failure of rock due to tectonic forces. However other types of seismicity are also common in environments such as glaciers, geothermal systems, and active volcanoes. While brittle failure earthquakes occur in these areas, pressure changes in fluid-filled cavities can produce other types of signals. At volcanoes, where they have been studied extensively, we can consider two of these seismic sources: long-period (LP) events and tremor signals (Chouet & Matoza, 2013). LP events and tremor are generally attributed to oscillations of fluid-filled cavities (Chouet, 1986, 1988). LP seismicity can dominate during fluid transport, and therefore, it serves as an important eruption precursor.

Most interpretations of LP events have employed a model of oscillations in a fluid-filled crack based on Chouet's seminal work (1986; 1988). He demonstrated numerically that a pressure disturbance on the crack initiates a slow dispersive wave called the crack wave that propagates slower than the acoustic velocity of the fluid within the crack. Because the theory of the crack wave was first introduced by Krauklis in 1962, the crack wave is also called the "Krauklis wave" in the literature (Korneev, 2008). As a consequence of the low speed of the Krauklis wave, the frequency characteristics of LP events are explained by resonance without the need for an unrealistically large magma reservoir (Ferrazzini & Aki, 1987). The Krauklis waves represent a gradual amplitude decay in the wave train

(Kumagai & Chouet, 1999, 2000, 2001; Lipovsky & Dunham, 2015). The physical origin of such amplitude decay lies in two mechanisms of attenuation: intrinsic absorption due to the fluid viscosity and seismic radiation (Aki, 1984). The quality factor Q describes the acoustic damping of the resonator system, which can be measured from the width of a spectra peak (Tary et al., 2014).

Following Chouet (1996 and 1998), many researchers have been focused on the analytical developments of the Krauklis wave. For instance, Korneev (2008) derived the phase velocity of the Krauklis wave for a crack model with inviscid fluid bounded between two half-spaces (thick fracture wall model), c_I,

$$c_I(f) = \left(\frac{\omega d\mu}{\rho_f}\left(1 - \left(\frac{\beta}{\alpha}\right)^2\right)\right)^{\frac{1}{3}}, \tag{1}$$

where β is the shear wave velocity in the matrix, α P-wave velocity in the matrix, μ matrix rigidity, d crack thickness, ρ_f fluid density, and ω the angular frequency. He also investigated the effects of viscosity on the Krauklis wave velocity and showed that the phase velocity decreases with the increase of the viscosity. Korneev et al. (2014) analytically obtained the phase velocity, c_F, for trilayer crack models

$$c_F(f) = \left(\frac{1}{6}\right)^{\frac{1}{6}}\sqrt{\omega H c_I(f)} \tag{2}$$

where H is the thickness of the fracture wall.

In addition to the analytical developments, extensive research has been conducted to understand the effects of the crack and fluid properties on the characteristics of the Krauklis waves. Through such understanding, by analyzing the Krauklis waves, we might obtain valuable information about the crack and the fluid involved (e.g., crack size or fluid type). Chouet (1986) introduced two dimensionless parameters that are called the crack stiffness (CS) and viscous damping (VD) given by

$$CS = \frac{b}{\mu}\frac{L}{d} \tag{3}$$

$$VD = \frac{12\eta L}{\rho_f d^2 \alpha} \tag{4}$$

where b is the fluid bulk modulus, L crack length, and η fluid viscosity. The crack stiffness and viscous damping respectively characterize the dynamic response of the crack and attenuation due to the fluid viscosity. Chouet (1988) shows that for a crack with high stiffness, the resonant frequencies of the crack wave shift toward low frequencies whereas for a low stiffness crack, the resonant frequencies become higher. In addition, Chouet (1988) shows how fluid viscosity yields the attenuation of higher frequencies.

Nakagawa & Korneev (2014) investigated the phase velocity of the Krauklis wave when the clamping force between two plates is not infinite, which called the compliant crack model. They theoretically showed that the phase velocity increases when the clamping becomes stronger. Nakagawa et al. (2015) presented a glass-made trilayer experiment to investigate the propagation of Krauklis waves in the frequency range of 0 to 1000 Hz. In their experiment, Nakagawa et al. (2015) observed the effect of the fracture compliance, which was due to the unexpected damage of the gasket seal between the plates contact, on the Krauklis waves.

We note that there has been a great interest to understand the effect of various fluid and crack properties of the characteristics of the Krauklis waves. In this experimental study, we investigated the effects of important factors on the dissipative and dispersive characteristics of the Krauklis wave, including crack stiffness, viscous damping, compliance, and geometry. Although some parameters such as crack stiffness, viscous damping and compliance or have been analytically or numerically investigated in previous studies, no comprehensive experimental study has been conducted to test those parameters. In addition, compared to the experimental study of Nakagawa et al. (2015), we investigate the effect of fracture compliance in a controlled condition by embedding different numbers of conical compression springs between the two fracture planes. Besides, to the best of our knowledge, no previous work has been conducted yet on the effect of the geometry.

4.3 Method

4.3.1 Experimental Setup

Our trilayer model was composed of two aluminum plates each of which has a dimension of 30.18 *cm* × 7.62 *cm* × 1.27 *cm*. The upper plate was used to position a source and pressure transducer. Since we had just two pressure transducers, the experiment was repeated multiple times with one pressure transducer was moved along the crack to a new location each time (the red box in Fig. 1a). The remaining holes were plugged. The other transducer was placed at the end of the plate to assess the data quality. To emulate a crack model, the two plates were set parallel to each other; washers with specified thickness were positioned between them to create a gap; and then, the plates were clamped together (Fig. 1b). We confirmed that the gap (crack thickness) is almost equal to the washers' thicknesses after clamping the plates. The physical properties of the aluminum plate are shown in Table 4-1.

Table 4-1. Physical properties of the aluminum plate.

Thickness (**H**)	Width (**w**)	Length (**L**)	Shear modulus ($\boldsymbol{\mu}$)	Vp ($\boldsymbol{\alpha}$)	Vs ($\boldsymbol{\beta}$)
12.7 cm	7.62 cm	30.48 cm	24 GPa	5587 m/s	2670 m/s

The source was a MULTICOMP piezoelectric element with a resonant frequency of 4.2 kHz that was affixed to a circular brass diagram and positioned on the edge of the crack (indicate by the red arrow in Figure 4-1a). The receiver transducer was positioned along the length of the crack in the plugs to record the Krauklis wave (Figure 4-1c). The receiver is a PCB Model 113B21 dynamic pressure transducer that has a low-frequency response of 0.5 Hz, the sensitivity of 100mV/kPa, and a resonant frequency of 500 kHz. To saturate the crack model, the entire apparatus was placed in a tank of fluid (e.g., water or oil, Figure 4-2). The water tank is placed on a soft foam to avoid environmental vibration noise.

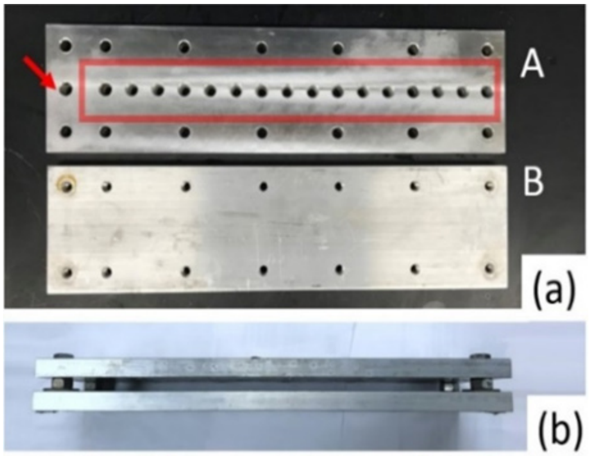

Figure 4-1. Trilayer aluminum model. (a) A and B upper and lower plates respectively. The red box indicates the receiver locations respectively. (b) Trilayer from the cross. The crack model is created by placing washers between the two plates.

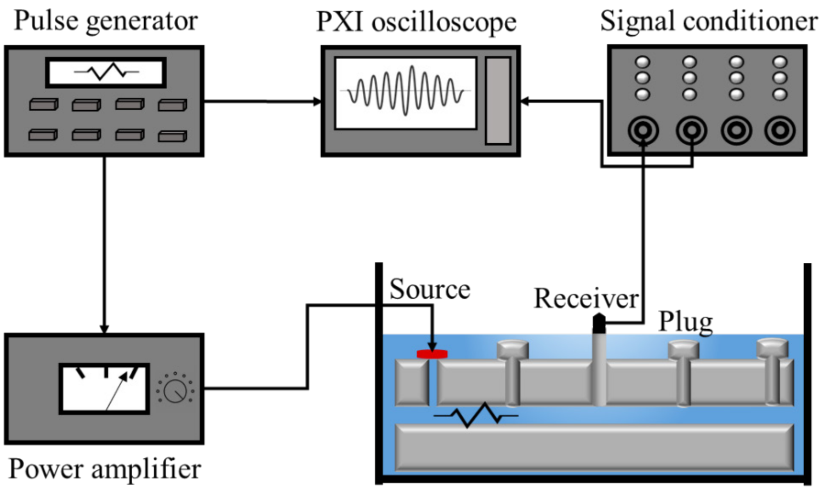

Figure 4-2. Schematic diagram of the data acquisition system. A pressure pulse from source is transmitted to the crack through the conduit on the left side of the model. The receiver acquires data and moves along the plate to obtain the seismic array.

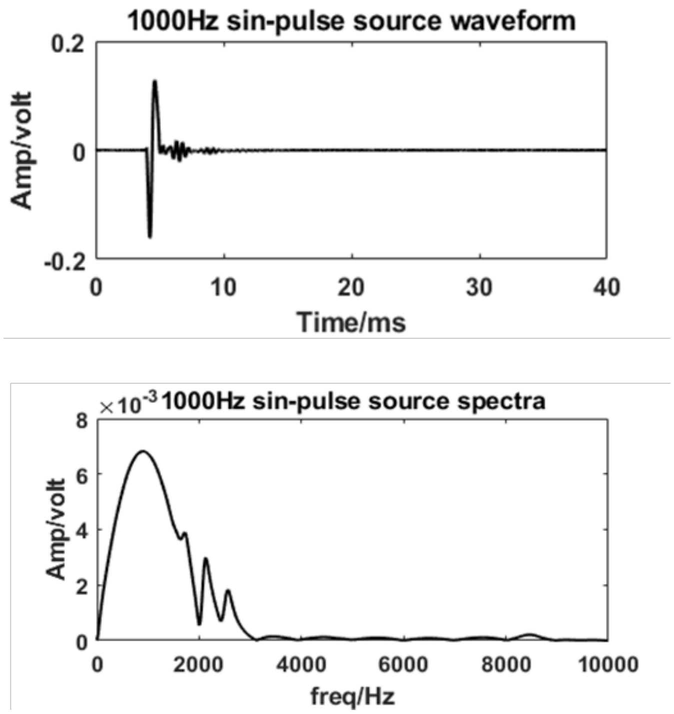
1000Hz sin-pulse source waveform

1000Hz sin-pulse source spectra

Figure 4-3. The source waveform and its amplitude spectra. The single sin-modulated input pulse of a 1000Hz dominant frequency is measured from the source by attaching the receiver to the source.

4.3.2 Processing

We applied different transformations to our data to characterize the Krauklis wave. First, for a given receiver location, we repeated data acquisition 25 times. Thereafter, the generated 25 traces were stacked to suppress any random or incoherent noise. Once we acquired data at different locations over the trilayer model, we estimated the phase velocity of the Krauklis waves. To obtain the phase velocity of the Krauklis wave, we utilized the high-resolution linear Radon transform (HRLRT), which is advantageous over the conventional transformations such as the phase shift method (Park et al., 1998) as it provides a higher resolution of dispersion curve images particularly when there is a limited number of traces (Trad et al., 2003). This method has been used in surface wave studies to obtain the phase velocities of Rayleigh and Love waves (Jeng et al., 2020).

In addition, we calculated the amplitude spectra of the signals at each receiver location, normalized them, and put them together to obtain a 2D amplitude spectra map as a function of distance from the source (see Figure 4-10 as an example). Using this 2D map, not only can we identify resonance frequencies more easily, but also, we can investigate the dependency of resonance frequencies on location.

We applied the Sompi method to our Krauklis wave data. The Sompi method is a high-resolution spectral analysis method based on a homogeneous autoregressive (AR) equation. The complex frequencies are defined as $f + ig$ where $i = \sqrt{-1}$ and g are linked to the quality factor by $Q = -f/(2g)$. Therefore, the outputs of the Sompi method are the frequencies and quality factors of the Krauklis waves. This method has been widely used to analyse LP events from a volcano and hydraulic fracturing data (Kumagai & Chouet, 2000; Lesage et al., 2002; Nakano et al., 1998; Tary et al., 2014).

4.3.3 Boundary Conditions

The Krauklis waves propagating along the model are both reflected and transmitted at the sides of the crack which are exposed to the fluid in the bath. Considering the relatively low frequencies (<~5 kHz) of the waves used in the experiment, the longest wavelength in the bulk fluid (oil or water), which is ~0.3 m for 5 kHz in water, is approximately the maximum dimension of the trilayer model (30.18 cm). Because the distance between the free surface of the fluid bath and the crack model is much smaller than 0.3m, the boundary condition along the sides can be approximated by an open-end (wave-induced pressure is zero). In contrast, within the crack model, the wavelengths are much shorter because of the small phase velocities of Krauklis waves, which allows us to generate finite-amplitude waves using a pressure source near the edge of the model. The wavelengths in our experiment are much larger than the crack width.

4.4 Experimental Results

4.4.1 Crack Stiffness (Thickness)

4.4.1.1 Phase velocity

To investigate the effect of the crack stiffness on the Krauklis wave, we consider four thicknesses of 1.5 mm, 2.5 mm, 4.5 mm, and 8.5 mm. If we assume the aluminum rigidity (μ) 26 GPa, these thicknesses respectively yield crack stiffnesses of C =17, 10, 6, and 3. The waveforms of the Krauklis waves are shown in Figure 4-4. One important observation of the waveforms is the dependency of the amplitudes of the Krauklis waves to the receiver location as we note in some offsets, for example, geophone numbers 5 and 11 in Figure 4-4(a), the amplitudes are very weak. This can be due to the destructive interferences of direct and reflected Krauklis waves. The Krauklis waves are highly dispersive because the waves propagate in the elastic hydraulic fracture walls serving as the waveguide (Ferrazzini & Aki, 1987; Krauklis, 1962; Paillet & White, 1982). Therefore, we calculate the dispersion curves of the frequency-dependent wave velocity of the Krauklis wave using the HRLRT method in Figure 4-5, in which the solid curves correspond to the theoretical phase velocity of the Krauklis wave obtained from Equation 4. We note that our estimated phase velocities agree with the theoretical model. To compare the phase velocities, the picked phase velocities from the dispersion curves in Figure 4-5 are shown in Figure 4-6 from which we note that the phase velocity increases with decreasing crack stiffness (increasing crack thickness).

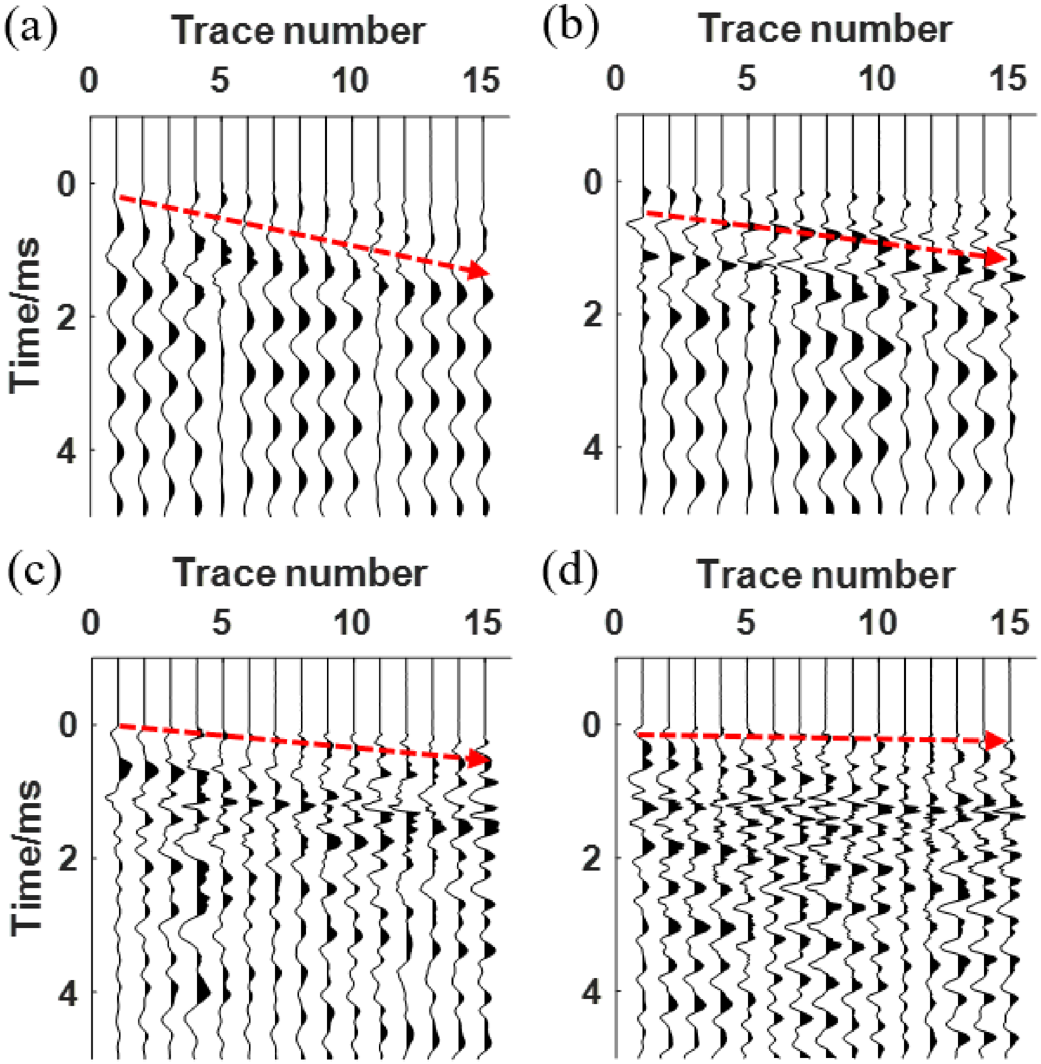

Figure 4-4. a-d the waveforms for the thicknesses of 1.5, 2.5, 4.5 and 8.5 mm, corresponding to crack stiffnesses of 17, 10, 6, and 3 respectively. For each of the fracture models, the first three modes of resonant frequencies can be identified and indicated by the red number. The red arrow follows the propagation direction and is not intended to track any specific arrival.

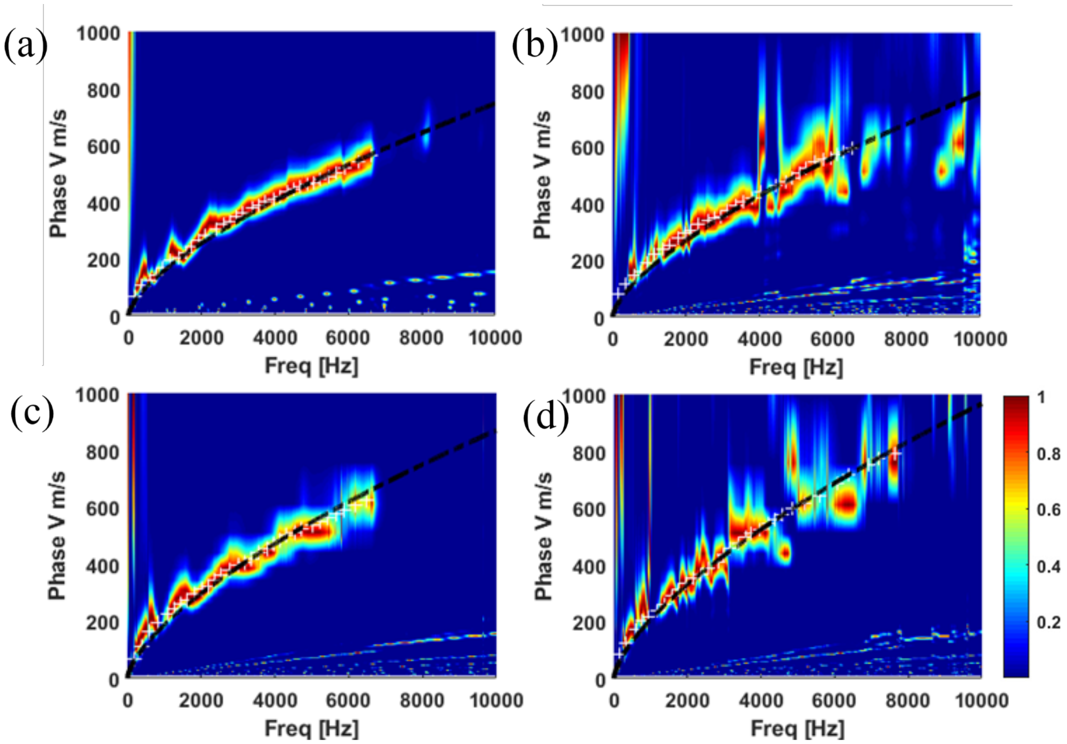

Figure 4-5. The phase velocity of the waveforms in Figure 4-4 for the crack thickness of (a) 1.5, (b) 2.5, (c) 4.5, and (d) 8.5mm. The white-cross markers are the picked values and the black dashed curve are theoretical fittings.

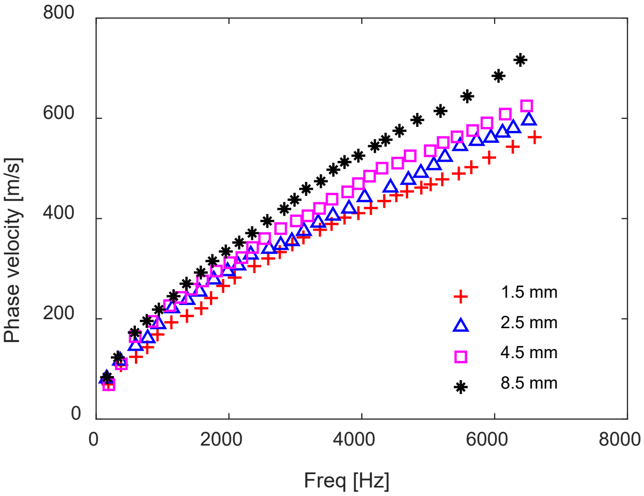

Figure 4-6. The overlay plot of the picked dispersion curves for different fracture thickness in Figure 4-5.

4.4.1.2 Resonant frequencies

The resonance is another important property of the Krauklis waves resulted from the constructive interferences of counterpropagating waves along the fracture conduit (Frehner, 2014; Korneev, 2008; Liang et al., 2017; Lipovsky & Dunham, 2015). The finite length of the crack in our experiment allows investigating the effect of crack stiffness on the resonant frequencies. Nondispersive waves have resonance frequencies of $\mathrm{f_n = nf_1}$, while the resonance frequency spacing between successive modes of Krauklis waves is a non-integer multiple of the fundamental (n=1) mode. This characteristic could be used to verify if some observed resonances are indeed associated with fluid-filled cracks (Gräff et al., 2019; Lipovsky & Dunham, 2015). Consider the rigid fracture with the finite length of L, resonance behavior requires the wavelength λ satisfy:

$$L = \frac{n\lambda}{2}, (n = 1,2,3 \ldots) \qquad (5)$$

$$f = \frac{nc_F(f)}{2L} \qquad (6)$$

Where $\mathrm{c_F(f)}$ is the Krauklis wave phase velocity in Equation 2. Therefore, the resonance frequency estimated is

$$f = \frac{1}{2}\pi^2\left(\frac{n}{L}\right)^3\sqrt{\frac{H^3 d\mu\left(1-\left(\frac{\beta}{\alpha}\right)^2\right)}{6\rho}}, \qquad (n = 1,2,3 \ldots) \qquad (7)$$

and the theoretical resonant frequencies obtained from Equation 7 is shown in Table 4-2. We observed that in Table 4-2 the frequency of the first mode in each experiment is less than 50 Hz and the second mode is below 400Hz.

Table 4-2. Theoretical resonance frequencies estimated from cracks with different thicknesses.

Crack thickness (mm)	F1(Hz)	F2 (Hz)	F3 (Hz)	F4 (Hz)	F5 (Hz)
d_1=1.5	17	134	452	1073	2096
d_2=2.5	21	173	584	1385	2705
d_3=4.5	29	232	784	1858	3630
d_4=8.5	40	319	1077	2554	4989

In our experiments, we applied the fast Fourier transform to the signals recorded at all the 15 receivers in each of the experiments; and the 2D map of the amplitude spectra and the average amplitude spectra of all the 15 traces are shown on top of each panel in Figure 4-7. The first three observed frequencies of the Krauklis waves for different stiffnesses are presented in Table 4-3. We observe that by decreasing the crack stiffness (i.e., increasing thickness), the resonance frequencies shift to higher frequencies.

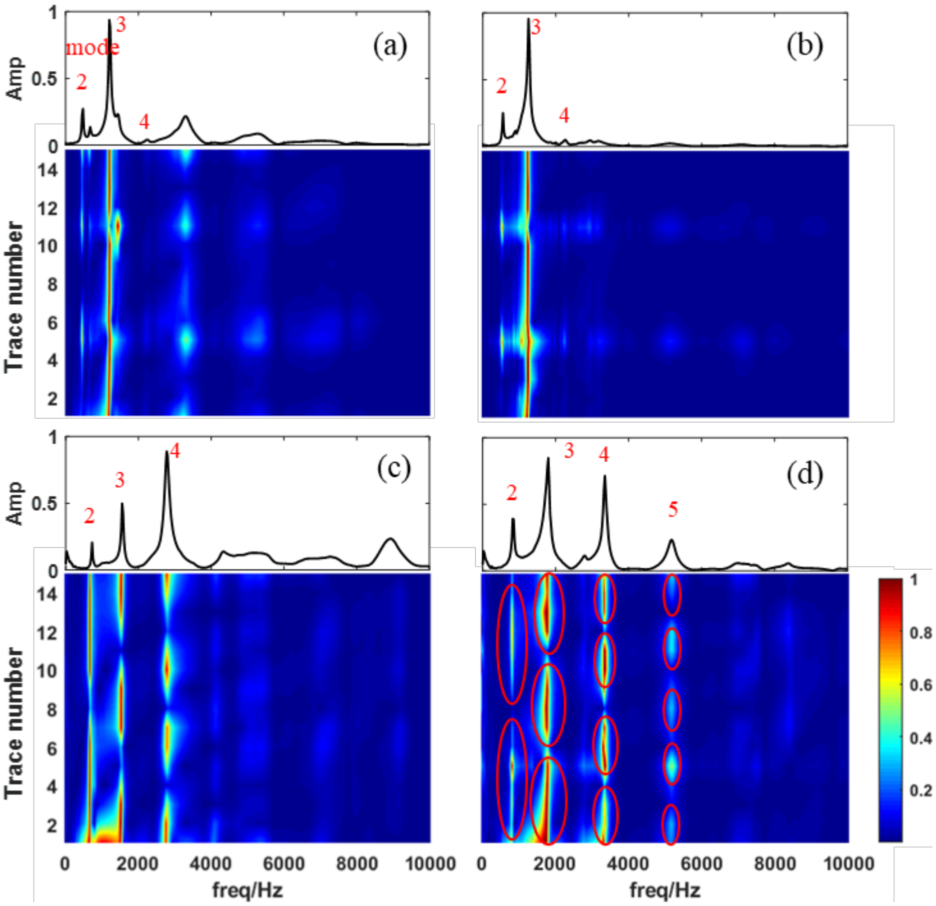

Figure 4-7. The normalized amplitude spectra of the waveforms in Figure 4-4 for the crack thickness of (a) 1.5, (b) 2.5, (c) 4.5, and (d) 8.5mm. The top plot shows the mean spectra of all 15 traces. The mode numbers are indicated at peak resonant frequencies. (d) The high amplitude marked by the red circle represents the antinode pressure. Higher mode resonance shows more antinodes.

Table 4-3. Experimental Resonance frequencies from cracks with different thickness.

Crack thickness (mm)	f1(Hz)	f2(Hz)	f3 (Hz)	f4(Hz)	f5(Hz)
d_1=1.5	–	475	1200	2225	–
d_2=2.5	–	575	1250	2250	–
d_3=4.5	–	725	1525	2775	–
d_4=8.5	–	875	1800	3350	–

However, we note that the theoretical first mode *F1* in Table 4-2 are not observed in the experimentally measured resonant frequencies in Table 4-3. This is due to the natural limitation of our finite length fracture that works poorly in low-frequency band because the fracture cannot accommodate the long wavelength of the lower modes. In addition, the source does not produce strong low frequency bandwidth to support the excitation of low frequencies. For the fracture of thickness 4.5mm, we calculated the frequency-wavelength relation (Figure 4-8) based on the experimental dispersion curved extracted from Figure 4-5 (c). With respect to equation 3, the wavelength of the first mode is λ_1=2L=0.604 m where its corresponding frequency estimated from Figure 4-8 is 30 Hz that is very close to the theoretical values 29 Hz in Table 4-2. Therefore, the first observed peaked frequencies measured in our experiments in Figure 4-7 are the second modes.

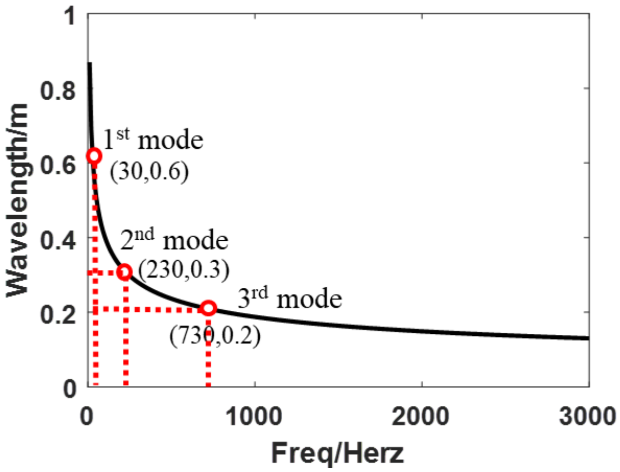

Figure 4-8. The frequency-wavelength relation calculated from the dispersion curve in Figure 4-5 (c) for the crack of 4.5mm thickness. The red circles indicate the first three modes with frequency and corresponding wavelength in parentheses. The first two modes are not observed in the 2D resonance map in Figure 4-7.

In addition, we calculated the resonant frequency ratio between different crack thicknesses to avoid parameter errors for both the experimental theoretical frequencies in Table 4-4 to analyze the discrepancy. We observe that the frequency ratios between the experimental and theoretical frequencies are stable at different crack thicknesses with an average error discrepancy around 0.1. These discrepancies might be caused by the fracture compliance variations in fractures with different thickness.

Table 4-4. Experimental and theoretical resonance frequencies ratio from cracks with different thickness.

Frequency ratio	Experimental frequency ratio			Theoretical frequency ratio		
$f(d_2)/f(d_1)$	1.21	1.04	1.01	1.29	1.29	1.29
$f(d_3)/f(d_2)$	1.26	1.22	1.23	1.34	1.34	1.34
$f(d_4)/f(d_3)$	1.21	1.18	1.20	1.37	1.37	1.37

4.4.1.3 Quality factor

The Sompi analysis was applied to the middle traces (8^{th} receiver location) in Figure 4-9 of four crack models in the form of frequency-growth rate on the (*f-g*) diagrams (Figure 4-10). In Figure 4-10, the dense clusters correspond to the resonant components of the coherent signal that are stably calculated from different AR orders. Whereas the scattered points represent incoherent noise. We note that the crack thicknesses increase, the quality factor increase. In other words, the intrinsic absorption is higher in thinner (stiffer) cracks (Liang et al., 2017).

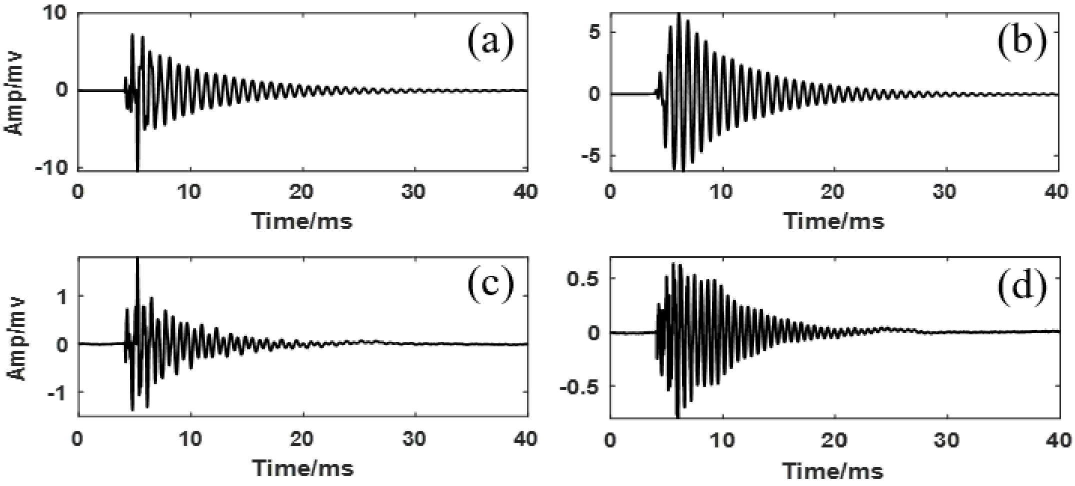

Figure 4-9. 4 traces at the trace 8 from the crack thickness of (a) 1.5, (b) 2.5, (c) 4.5, and (d) 8.5mm. The fracture thickness increases, the amplitude of Krauklis wave signal becomes weak.

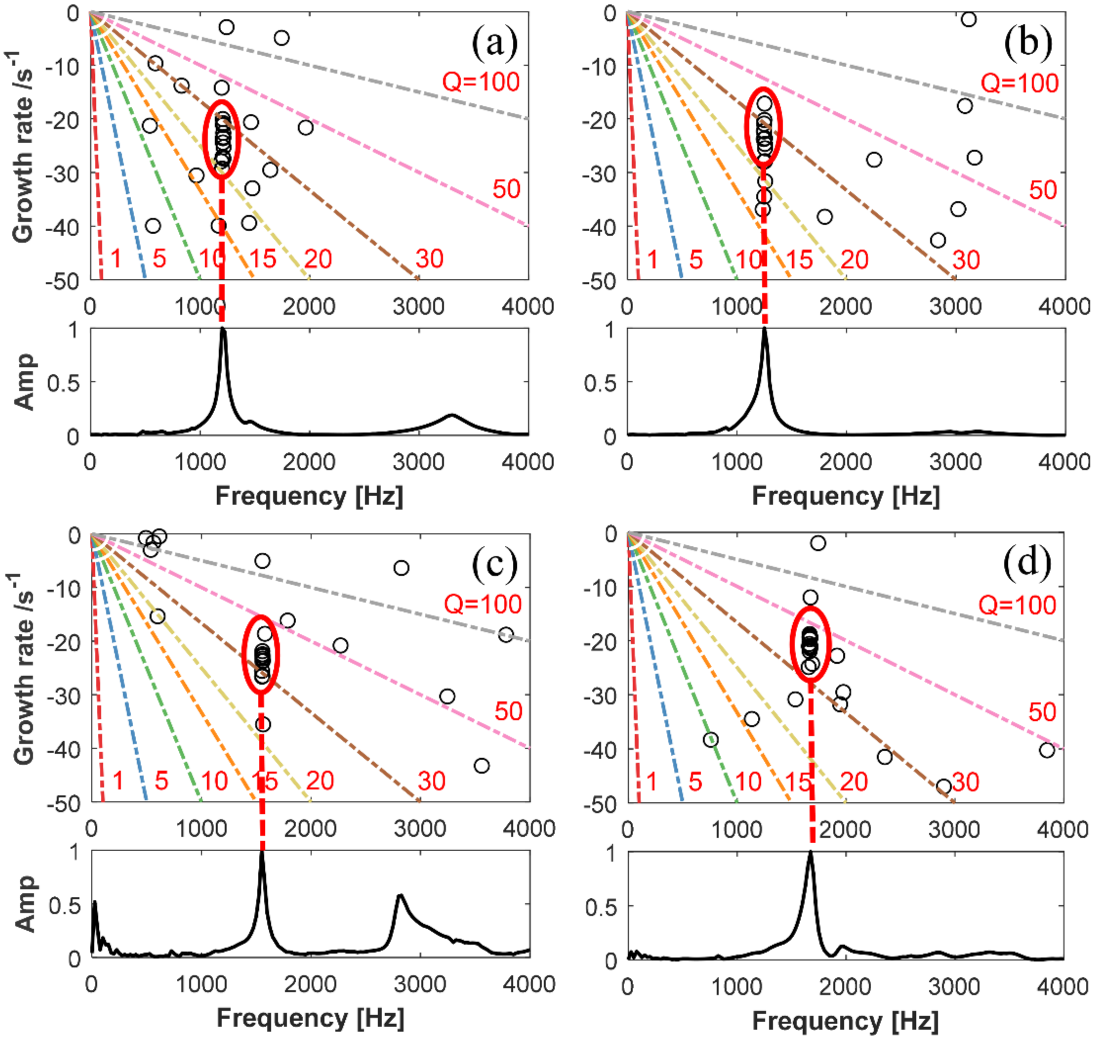

Figure 4-10. The quality factor for the crack thickness of (a) 1.5, (b) 2.5, (c) 4.5, and (d) 8.5mm at trace 8. As the stiffness decreases (thickness increases), the quality factor increases.

4.4.2 Viscous fluid

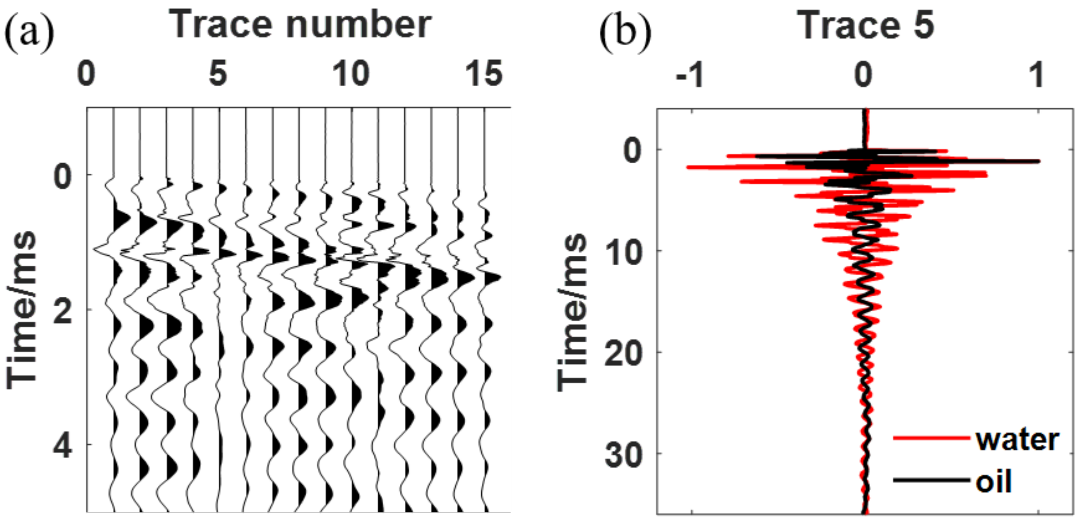

Figure 4-11. (a) The waveform array of acquired from the fracture filled with viscous oil. (b)The entire waveform of trace 5 comparison from water and oil-filled fracture of 4.5mm thickness fracture.

To investigate the effect of viscous damping on the Krauklis waves, we used vegetable oil as the fluid in the 4.5 mm thickness fracture. Galland et al. (2006) used the vegetable oil as magma analogue to study the magma injection in the upper crust. In Figure 4-11, trace 5 of the Krauklis waves from the 4.5 mm-thick fracture filled water and oil are presented showing that Krauklis waves sustain longer in water-filled fracture. The dynamic viscosity of water and oil are approximately 1.0 and 20 mPa·s, and density of 1000 and 920 kg/m^3 at room environment (Galland et al., 2006). Therefore, the dimensionless viscous damping factors VD defined in Equation (4) for water and oil are 0.032 and 1.61, respectively. The fracture stiffness CS of the oil-filled fracture obtained by Equation (3) is 4.2. Figure 4-12(a) shows the amplitude spectra of the entire data in which only two peaks at the frequencies of 625 and 1400 Hz are observable. Higher modes in the viscous oil are highly attenuated. Figure 4-12(b) shows the results of the Sompi analysis from which we note that the quality factor has significantly decreased in the case of the viscous fluid (Q=15) compared to the quality factor of 32 for the water-filled experiment. The phase velocity, however, (see Figure 4-12(c) and Figure 4-12(d)) shows a slight decrease at high frequency compared with that of the water-filled fracture. Such a small difference in the phase velocity can be explained by Chouet model (1986). While the analytical models (Korneev, 2008) suggest a significant decrease of the phase velocity for the case of infinite fractures, the crack stiffness mitigates the velocity drop for finite fractures. Note that although the oil filled fracture has a much higher viscous damping compared to the water filled one, it has a lower crack stiffness that according to Chouet's model should increase the velocity, and thus, moderates the velocity drop.

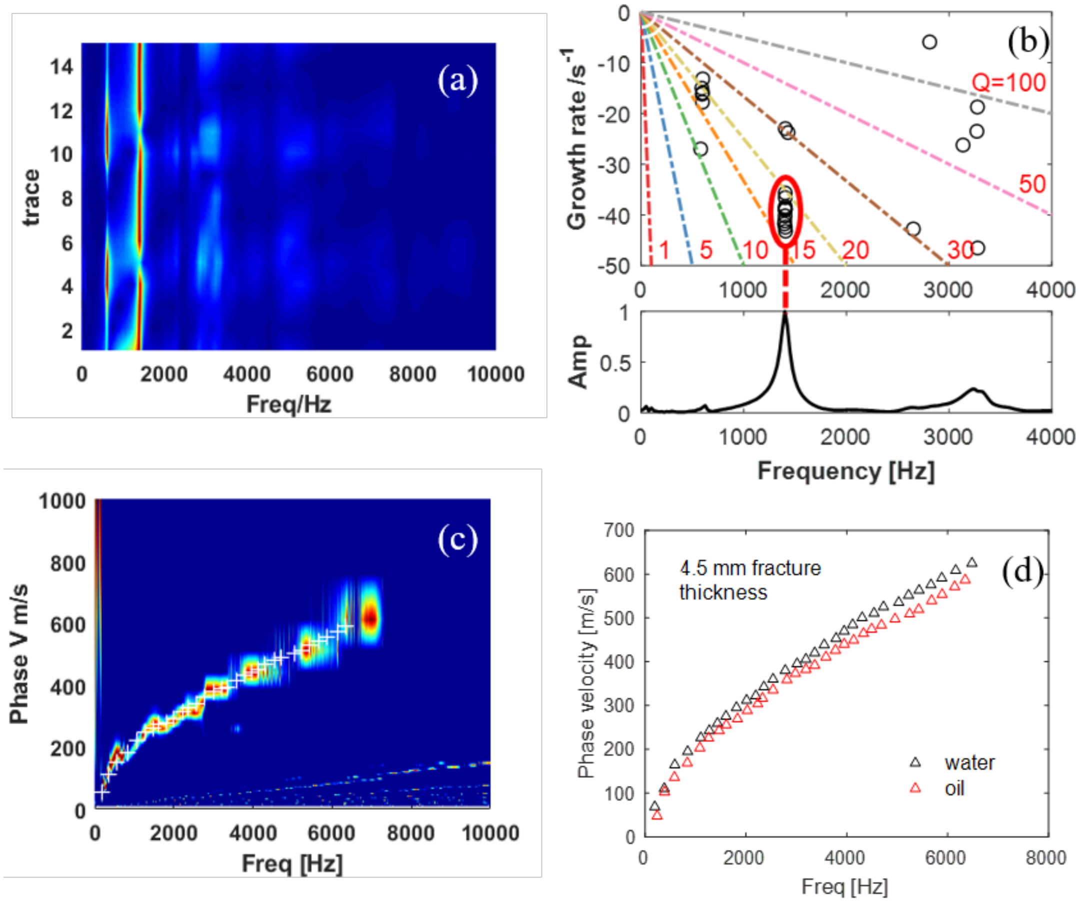

Figure 4-12. The properties of Krauklis waves in oil-filled fracture of 4.5 mm thickness. (a) The 2D map of resonance frequency (b) quality factor (c) phase velocity and (d) Comparison of the Krauklis wave phase velocity in the water−filled and oil−filled fracture of thickness 4.5 mm. All of these values in oil−filled fracture are lower than that in water.

4.4.3 Crack roughness and geometry

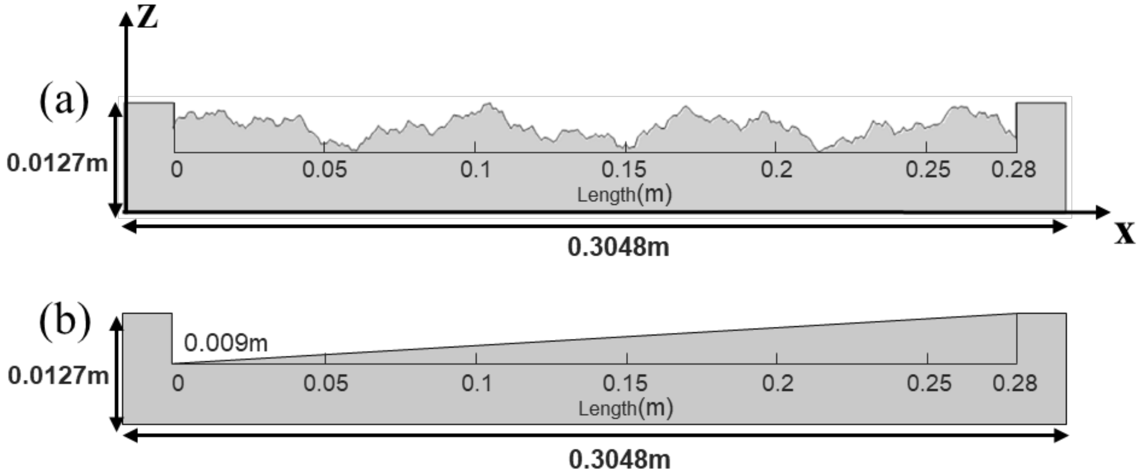

Figure 4-13. The fracture roughness model and the wedge shape model in (a) and (b).

Real fractures have much more complex geometries. For instance, fracture geometries might be rough and wedge shape with a pinch out tip. Such complex geometries can affect the fluid-solid interaction, and thus the seismic wave properties (Petrovitch et al., 2013).

To simulate roughness, we used the classical Weierstrass-Mandelbrot model (Askari et al., 2018; Lu et al., 2013; Mehrabi et al., 1997), where the height of the rough surface z as a function of distance x is given by

$$z(x) = \mathcal{L}\left(\frac{G}{\mathcal{L}}\right)^{D-1} \sum_{n=0}^{\infty} \frac{cos2\pi v^{n} x/\mathcal{L}}{v^{(2D)/n}} \qquad (8)$$

where $\mathcal{L}$ is the sample's length that depends on the scanning device, *D* is the fractal dimension, and *G* is the fractal roughness parameter that for a given *D* controls the amplitude of the roughness, and *v* >1 is a scaling parameter. To simulate roghness, we assumed *D* = 1.4 that has been reported for natural rocks (Lee et al. 1990), $\mathcal{L}$ =4 cm and

$G = 1.2 \times 10^{-6}$. The values of $\mathcal{L}$ and G yield the maximum roughness of 0.61 cm. Figure 4-13(a) and (b) respectively show the rough and wedge fracture models.

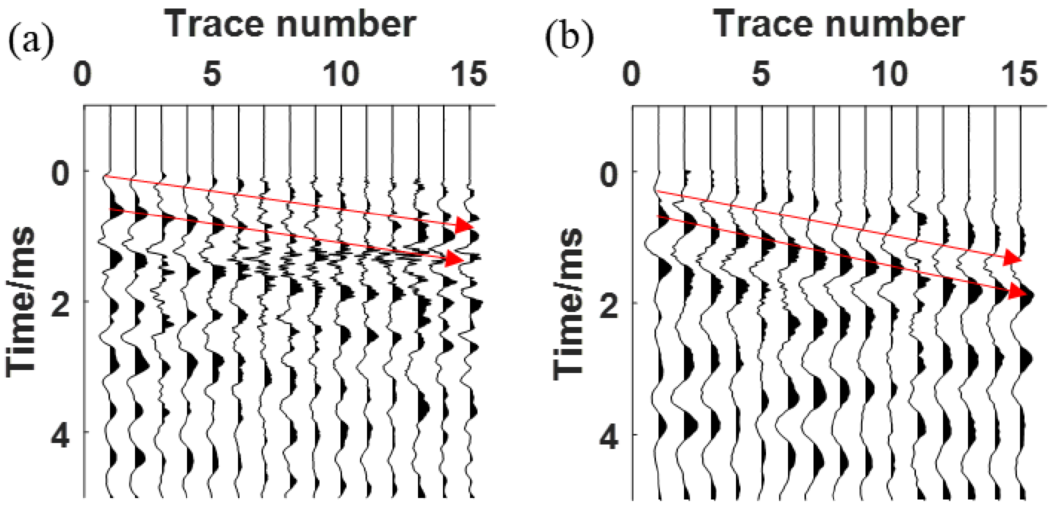

Figure 4-14. (a) and (b) The waveforms of the Krauklis wave of the rough and wedge fracture models. The red arrows follow the trend of the Krauklis wave propagation.

Figure 4-14 (a) and (b) show the waveform of the Krauklis waves from the rough and wedge fracture models respectively. We note that in Figure 4-14(a) the waveforms after trace 6 become noisy due to the wave scattering along the rough surface. Figure 4-15(a) and (b) show the phase velocities of the Krauklis waves for the rough and wedge fracture models respectively. In Figure 4-15(a), the black dashed line is the theoretical dispersion curves of a flat crack model (Equation 2) calculated using the average thickness of the top and bottom plate 10.45 mm. We note the both geometries have resulted decreased phase velocity from which it might be concluded that the low thickness areas on the rough and wedge fracture models significantly contribute to the decrease of the velocity. In addition, at high frequency around from 4000-6000 Hz, the phase velocity of the wedge fracture model significantly deviates from the theoretical curve. This might be explained by the extreme narrow fracture aperture at the pinch out tip.

The resonant frequencies of the rough fracture (Figure 4-16(a)) are 650, 1350 and 2950 Hz, and the wedge crack (Figure 4-16(b)) 425, 925, 1350, 1675 and 2950 Hz respectively. We note that the wedge fracture has a lower resonant frequency that is constant with its lower phase velocity.

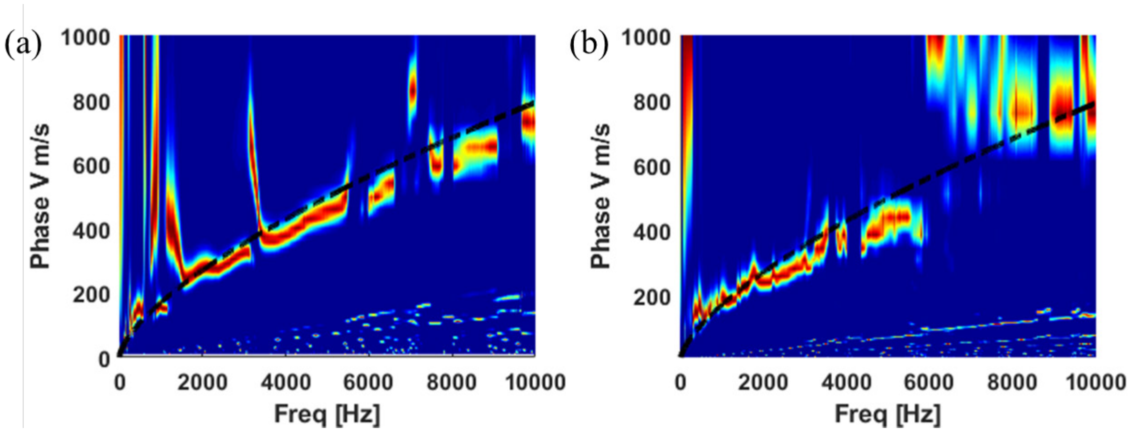

Figure 4-15. The phase velocity of crack wave from fracture roughness model and the wedge shape model in (a) and (b). The dashed black curve is the theoretical crack wave velocity for flat crack using the average thickness of the top and bottom plate 1.05 mm.

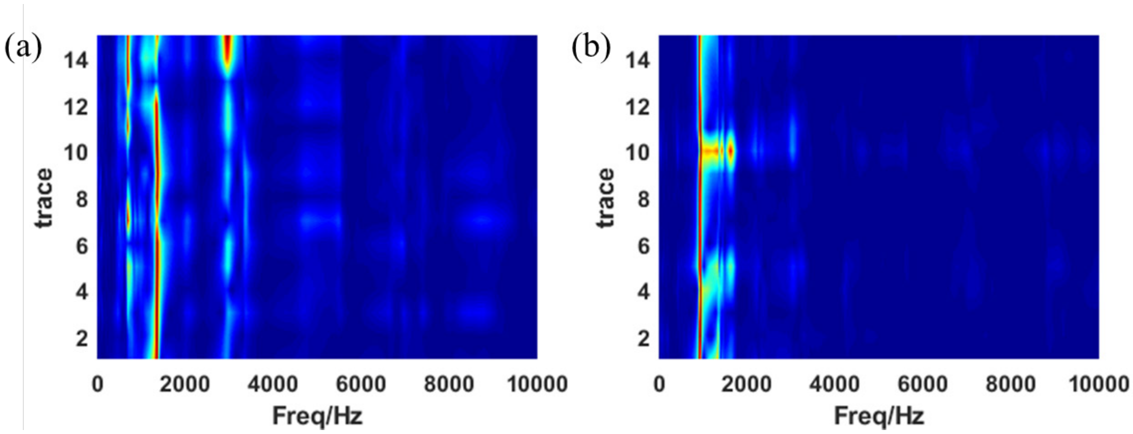

Figure 4-16. The resonance frequencies of crack wave from fracture roughness model and the wedge shape model in (a) and (b).

Considering the inhomogeneous fracture surface, we also apply the Sompi method to three traces which are well separated in offset. Trace 2 trace 8 and trace 12 are selected to compare the quality factors for roughness and wedge model in Figure 4-17 and Figure 4-18 respectively. On one hand in the roughness model in Figure 4-17(a) and (b) the quality factors in trace 2 and trace 8 are similar, while in trace 12 the quality factor increases. On the other hand, in the wedge fracture model in Figure 4-18, the quality factor in trace 2 is higher than that in trace 8 and 12. Overall, the dependency of the quality factors on the transducers location is noticeable in the both fracture models that can be due to the inhomogeneous surfaces of the two fractures.

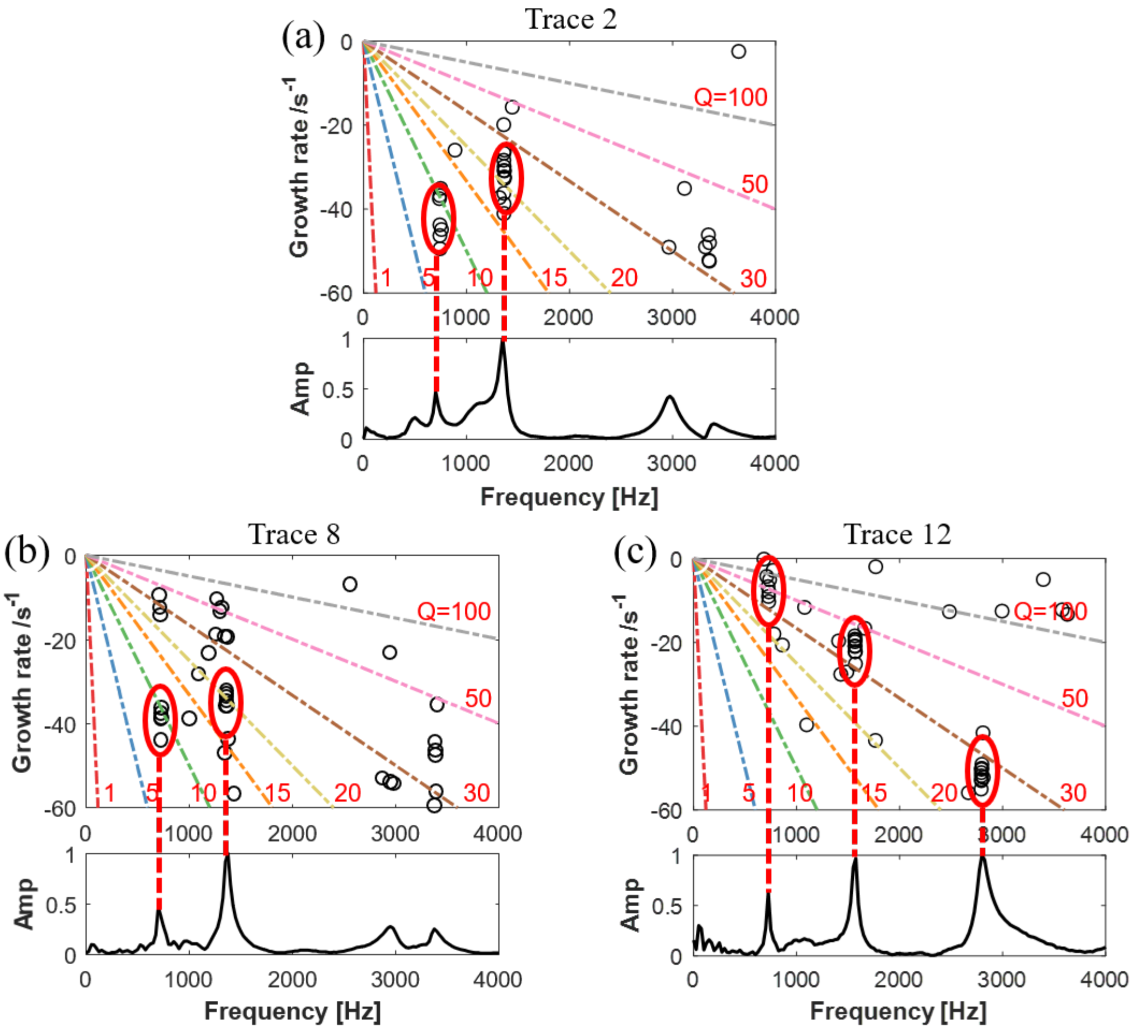

Figure 4-17. The quality factors obtained for the roughness model at (a) trace 2, (b) trace 8 and (c) trace 12.

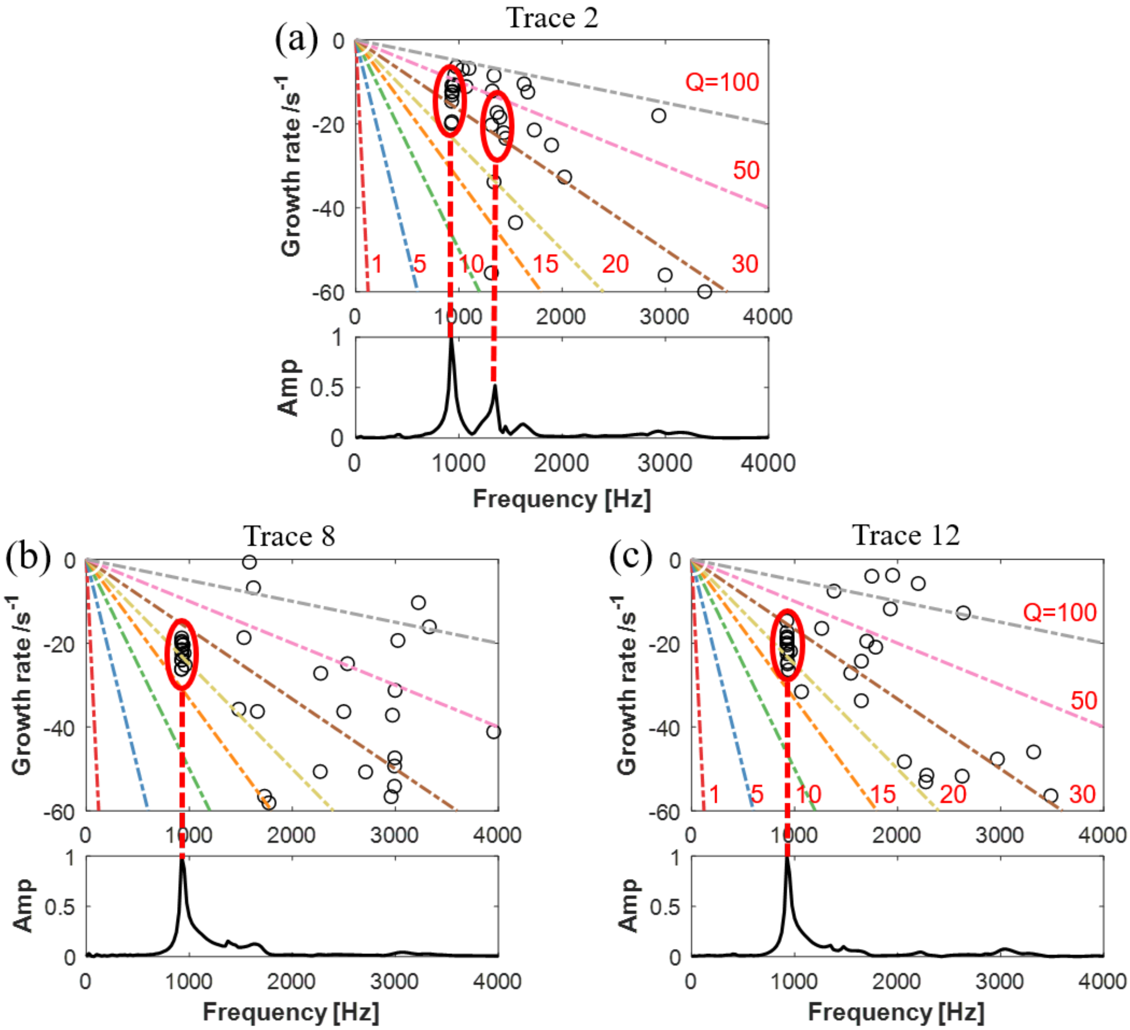

Figure 4-18. The quality factors obtained for the wedge model at (a) trace 2, (b) trace 8 and (c) trace 12.

4.4.4 Fracture compliance

In fracture mechanics, an open fracture that is under uniaxial compression σ deforms along the fracture length. A parameter that is commonly used to describe the properties of fracture surfaces is called fracture compliance Z_N (Liu, 2005) (or more commonly used in engineering, its inverse K_N=1/Z_N, the fracture stiffness), which is defined as

$$Z_N = \frac{1}{K_N} = \frac{\Delta h}{\Delta \sigma} \qquad (9)$$

A fracture with a higher number of asperities contact is less compliant than a fracture with sparsely spaced asperities (Brown & Scholz, 1985; Cook & Liniger, 1992; Hopkins et al., 1987). For example, if the contact points of the fracture planes are damaged (e.g., due to the fluid pressure), it will be more compliant (Nakagawa and Korneev, 2014). It has been observed that the magnitude of fracture compliance controls the velocity of fracture interface waves (Gu et al., 1996; Nakagawa et al., 2015; Pyrak-Nolte et al., 1990). In the following experiment, we investigate the effect of the fracture compliance on the Krauklis waves by embedding several conical compression springs between the two plates in Figure 4-1b .

Table 4-5. The physical parameters of the conical compression spring.

Diameter of spring wire	0.16 cm
Large end	2.22 cm
Small end	0.95 cm
Free height	1.27 cm
Number of active coils	7
Shear modulus	77.2 GPa
Spring rate	7763 N/m

The fracture compliance is modeled by using 4, 8, and 16 springs. The conical compression spring physical parameters are shown in Table 4-5. The resonant frequencies and phase velocities of the Krauklis wave from different compliant crack models are shown in Figure 4-19 from which we note both the resonant frequency and velocity increase with decreasing fracture compliance. The resonant frequencies of different modes are shown in Table 4-6. And the quality factors at the trace 8 for each case are calculated in Figure 4-20 from which we observed that the quality factor for 8 springs fracture Figure 4-20(b) is the lowest compare to the others due to the uneven compliance. The fractures embedded with 8 and 16 springs in Figure 4-19(d) are stiffer, especially at the locations of the springs. The uneven stiffness over the plates might results in the mismatch dispersion at low frequencies less than 3000 Hz in Figure 4-19(d) and (f). The dispersion curves in Figure 4-19 are picked indicated by white crossings markers and plot in for comparison in Figure 4-21.

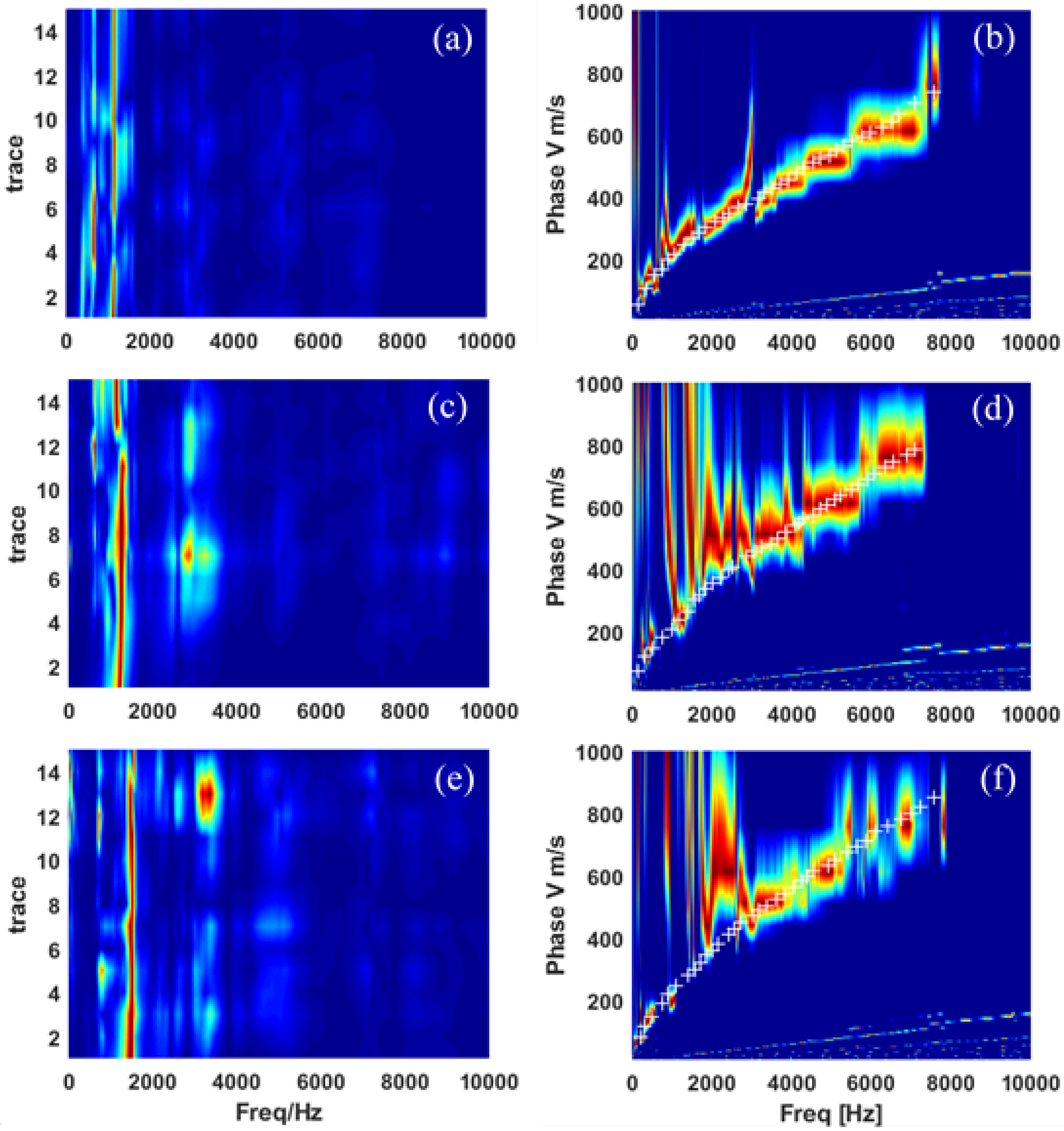

Figure 4-19. Comparison of the resonant frequencies and phase velocity of fractures with different compliance. (a) and (b) are the resonant frequency map and phase velocity of fracture supported by two springs; (b) and (c) by 8 springs; (e) and (f) by 16 springs. The resonant frequencies and phase velocity increased with decreasing compliance. The white crossing markers are the picked dispersion curve to follow the HRLRT calculated trend.

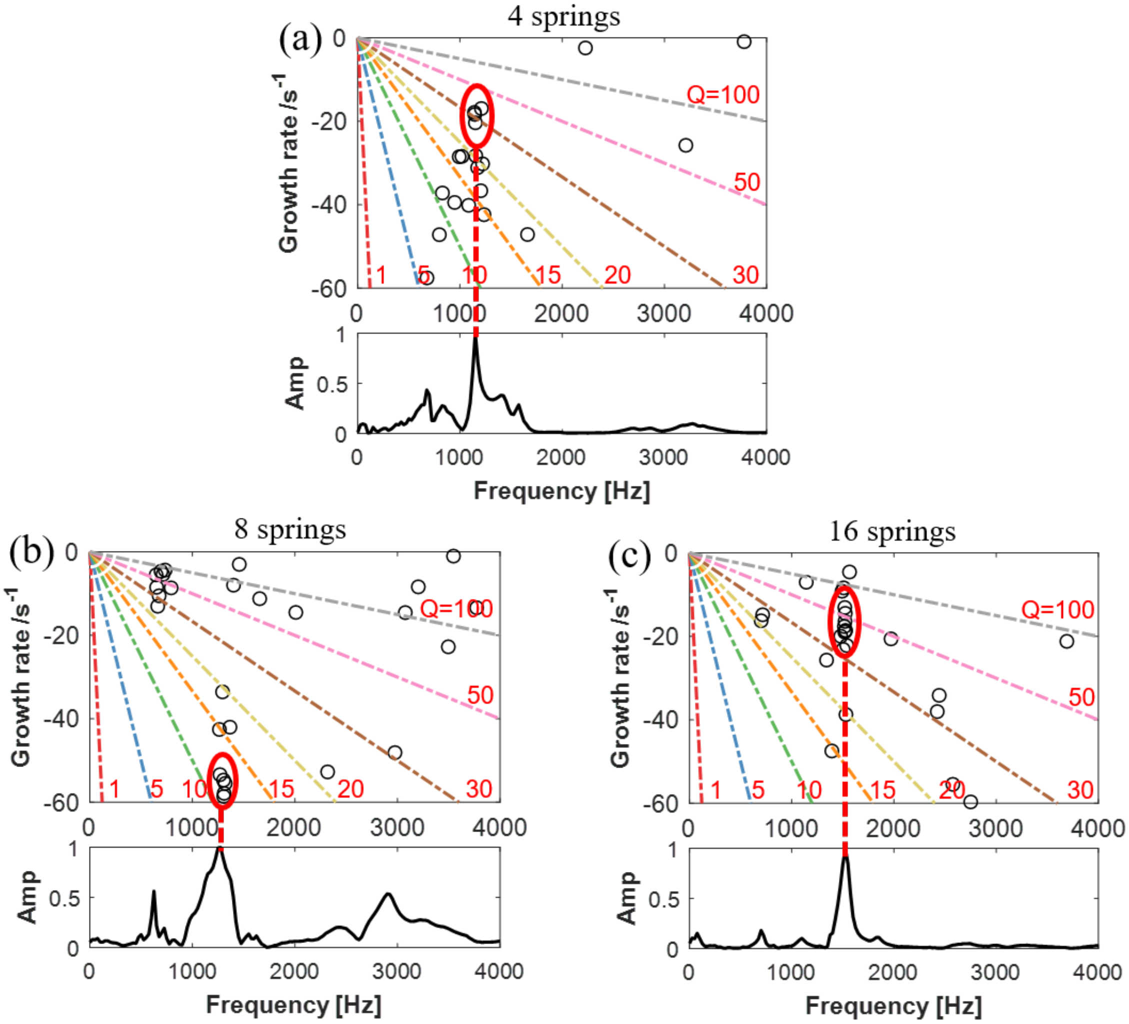

Figure 4-20. The quality factors obtained from complaint fractures embedded with springs. (a) fracture with 4 springs. (b) fracture with 8 springs. (c) fracture with 16 springs

Table 4-6. Resonant frequencies of cracks with different compliance

Spring numbers	f3(Hz)	f4(Hz)	f5(Hz)
4	400	675	1150
8	625	1250	2900
16	725	1500	3425

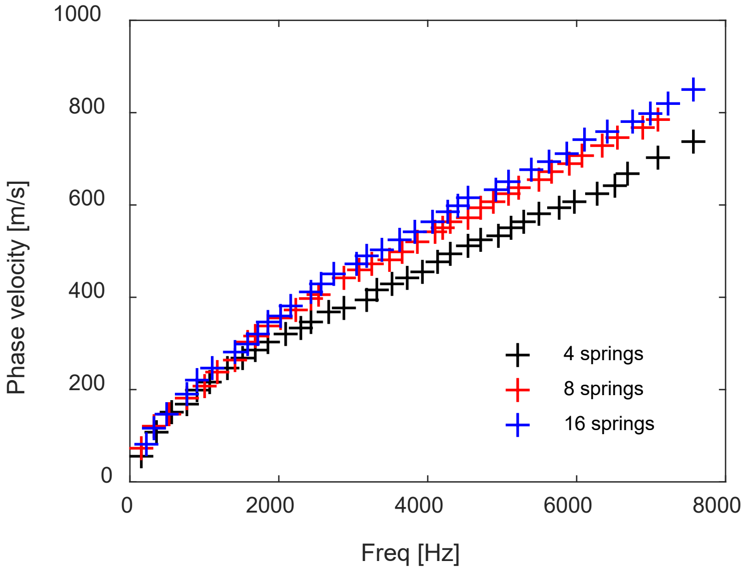

Figure 4-21. The overlay plot of the picked dispersion curves of Krauklis waves for cracks with different fracture compliance in Figure 4-19.

4.5 Discussion

4.5.1 Open-end fracture

All the fracture models presented are subjected to open-end vibration condition which means the standing waves have displacement antinodes (maximum displacement) at the ends of the fracture. If we ignore complex solid-fluid interactions and just focus on the fluid wave propagation in a 2D system. The mode analysis for the fluid pressure vibration in open-end fracture in Figure 4-22 also proves our mode identification in Figure 4-7. This also explains some weak signals recorded due to destructive wave interferences for example in Figure 4-4(a) trace 5 and trace 11.

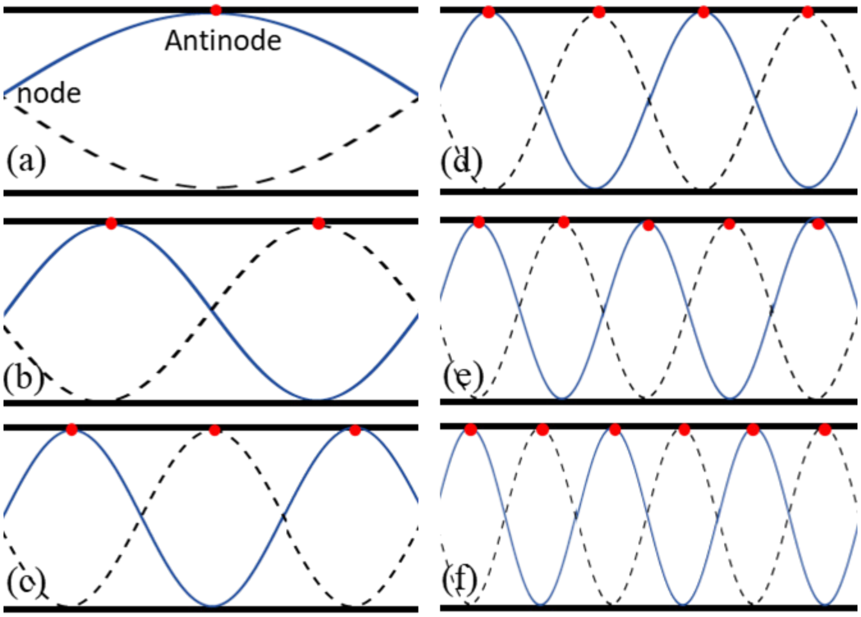

Figure 4-22. The pressure vibration of Krauklis waves in open-end fracture. (a) to (f) represent the fundamental mode to mode 6, respectively. The red points represent the antinodes at the maximum pressure.

4.5.2 Closed-end fracture

To compare with the open-end fracture, we also conducted the experiment for flat fracture with closed-end fracture for 4.5 mm thickness. In Figure 4-23(a), instead of some deconstructive traces observed in an open-end fracture in Figure 4-4, all the traces constructively interfered. The resonant frequencies in Figure 4-23(b) indicated by red arrows are 650, 1425 and 2750 Hz which are slightly less than the open-end fracture case 725, 1525 and 2775 Hz.

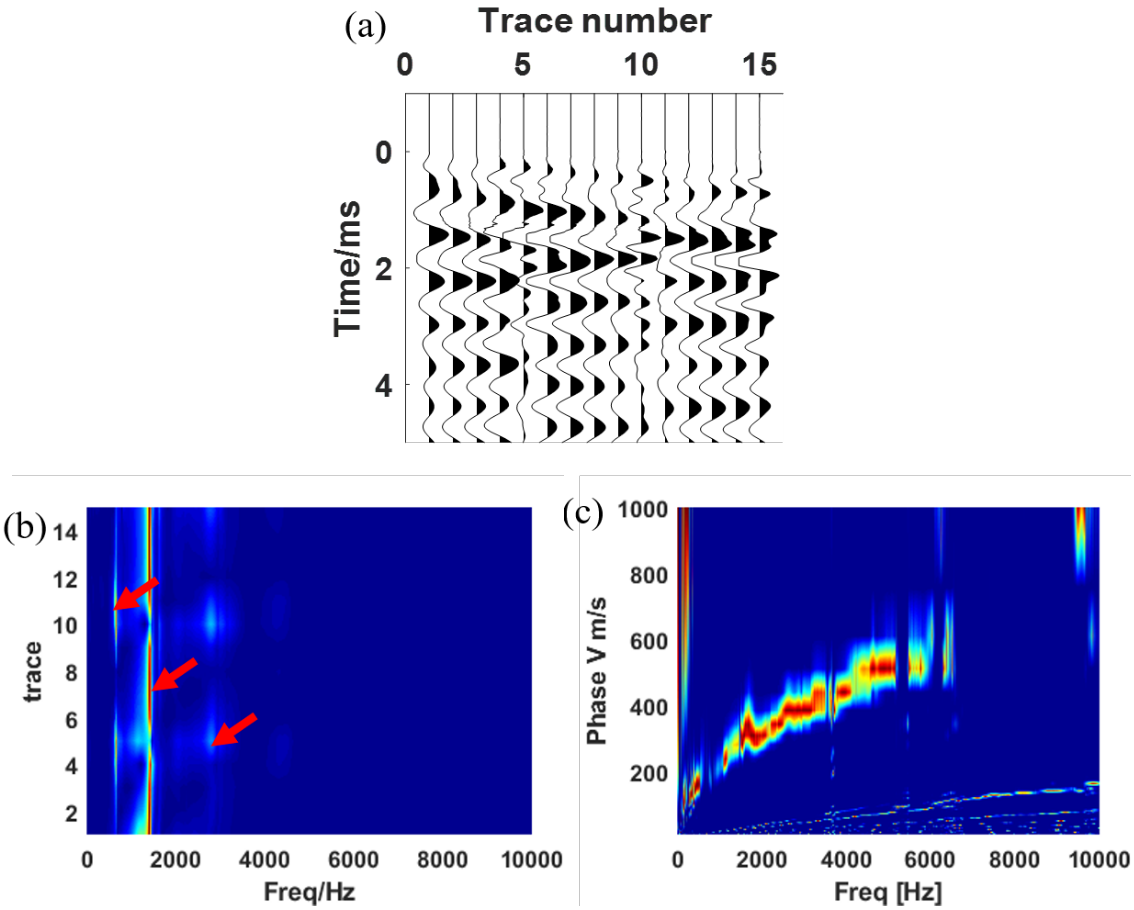

Figure 4-23. Krauklis waves properties in the closed-end fracture. (a) the 2D seismic array. (b) the resonant frequencies. The red arrows are pointing at different modes. (c) The phase velocity.

4.5.3 Application

One of the applications of the Krauklis wave is to determine the fracture size. Lipovsky & Dunham (2015) presented a method to estimate the aperture and length of a resonating hydraulic fracture using both the seismically observed quality factor and characteristic resonant frequency.

$$L = \frac{1}{2}\left[\pi\nu\left(\frac{G_S}{(1-\upsilon_s)\rho}\right)^2\left(\frac{Q_r^2}{f_r^5}\right)\right]^{1/6} \tag{10}$$

$$2w_0 = Q_r\sqrt{\frac{\nu}{\pi f_r}}. \tag{11}$$

where ν is the fluid kinematic viscosity, G_S is the shear modulus of the aluminum plate, υ_s is the Poisson's ratio, ρ is the fluid density, Q_r is the quality factor at the resonant frequency, f_r is the resonant frequency, w_0 is the half-width of the fracture aperture.

The solid and fluid parameters to calculate the fracture geometry using equations 10 and 11 are shown in Table 4-7. Take the 4.5 mm thickness fracture filled with water for example to test the feasibility of the equations (10) and (11). We calculate the quality factor and resonant frequency from the trace 12 from which we can observe all the three modes at the antinode location using Sompi method (Figure 4-24). Using the first observed peak frequency 725 Hz and quality factor 50 observed in Figure 4-24 and parameters in Table 4-7, the fracture length calculated is 32.5 cm which is very close to the fracture model 30.48 cm.

Table 4-7. Input parameters for equation 6 to calculate the fracture length.

$\boldsymbol{\nu}$ (m^2/s)	$\boldsymbol{G_s}$ (Gpa)	$\boldsymbol{\upsilon_s}$	$\boldsymbol{\rho}$ (kg/m^3)	$\boldsymbol{Q_r}$	$\boldsymbol{f_r}$ (Hz)
1.5×10^{-6}	24	0.33	1000	50	725

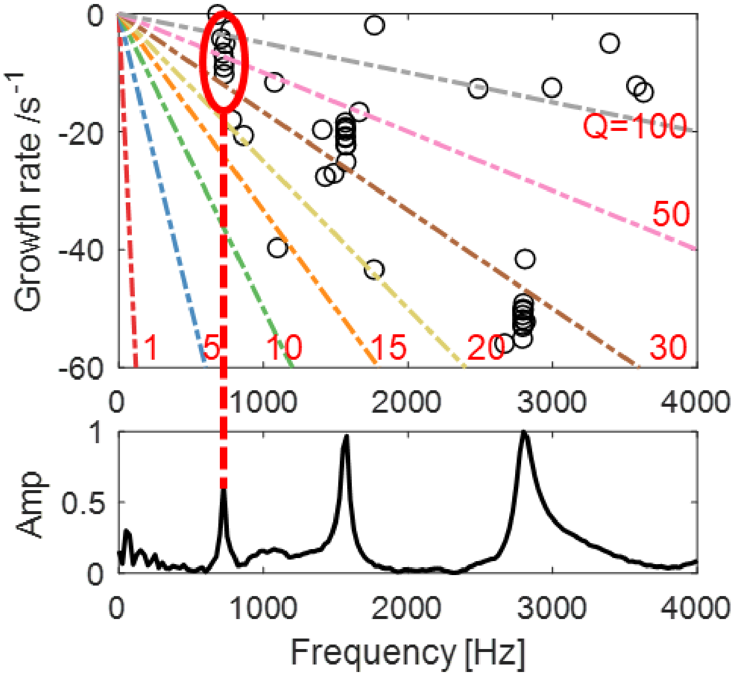

Figure 4-24. The resonance frequencies and quality factors calculated using Sompi method. The first observed resonant frequency 725 Hz and its corresponding quality factor 50 are used to calculate the fracture length using equation 6.

4.6 Conclusion

We conducted numerous experiments to investigate the effects of the crack stiffness, viscous damping, compliance and geometry on the resonance, dissipative and dispersion characteristics of the Krauklis waves. Therefore, we divide our experiments into four categories where our major results are shown in Table 4-8.

Our results in terms of the effect of the crack stiffness and viscous damping on the dispersion and resonance of the Krauklis wave are consistent with Chouet's numerical model. In addition, we note that geometry significantly contribute to the dispersion and dissipative properties of the Krauklis waves. In addition, we found that that higher complaint fractures result in slower wave velocity and resonant frequencies. To validate the experimental result, we compared it to existed theoretical equations, which showed good agreement between them for Krauklis waves in flat fractures.

Table 4-8. Experiments in the paper.

Exp	**Objective**	**Major Observation**
1	Stiffness	Phase velocity and resonant frequencies increase with decreasing the stiffness.
2	Viscous Damping	Phase velocity and resonant frequencies decrease with increasing damping factor.
3	Mechanical Compliance	Phase velocity and resonant frequencies increase with decreasing compliance.
4 (1)	Geometry (Roughness)	Phase velocity and resonant frequencies decrease comparing to Exp 1, 4.5mm.
4 (2)	Geometry (Wedge shape)	Phase velocity close to roughness model.

4.7 Reference

Aki, K. (1984). Evidence for magma intrusion during the Mammoth Lakes earthquakes of May 1980 and implications of the absence of volcanic (harmonic) tremor. *Journal of Geophysical Research: Solid Earth, 89*(B9), 7689-7696.

Askari, R., Hejazi, S. H., & Sahimi, M. (2018). Thermal conduction in deforming isotropic and anisotropic granular porous media with rough grain surface. *Transport in Porous Media, 124*(1), 221-236.

Brown, S. R., & Scholz, C. H. (1985). Broad bandwidth study of the topography of natural rock surfaces. *Journal of Geophysical Research: Solid Earth, 90*(B14), 12575-12582.

Chouet, B. (1986). Dynamics of a fluid-driven crack in three dimensions by the finite difference method. *Journal of Geophysical Research: Solid Earth, 91*(B14), 13967-13992.

Chouet, B. (1988). Resonance of a fluid-driven crack: Radiation properties and implications for the source of long-period events and harmonic tremor. *Journal of Geophysical Research: Solid Earth, 93*(B5), 4375-4400.

Chouet, B. A., & Matoza, R. S. (2013). A multi-decadal view of seismic methods for detecting precursors of magma movement and eruption. *Journal of Volcanology and Geothermal Research, 252*, 108-175.

Cook, R., & Liniger, E. (1992). Grain-size effects in the indentation fracture of MgO. *Journal of materials science, 27*(17), 4751-4761.

Ferrazzini, V., & Aki, K. (1987). Slow waves trapped in a fluid-filled infinite crack: Implication for volcanic tremor. *Journal of Geophysical Research: Solid Earth, 92*(B9), 9215-9223.

Ferrazzini, V., Chouet, B., Fehler, M., & Aki, K. (1990). Quantitative analysis of long-period events recorded during hydrofracture experiments at Fenton Hill, New Mexico. *Journal of Geophysical Research: Solid Earth, 95*(B13), 21871-21884.

Frehner, M. (2014). Krauklis wave initiation in fluid-filled fractures by seismic body waves. *Geophysics, 79*(1), T27-T35.

Frehner, M., & Schmalholz, S. M. (2010). Finite-element simulations of Stoneley guided-wave reflection and scattering at the tips of fluid-filled fractures. *Geophysics, 75*(2), T23-T36.

Galland, O., Cobbold, P. R., Hallot, E., de Bremond d'Ars, J., & Delavaud, G. (2006). Use of vegetable oil and silica powder for scale modelling of magmatic intrusion in a deforming brittle crust. *Earth and Planetary Science Letters, 243*(3-4), 786-804.

Gräff, D., Walter, F., & Lipovsky, B. P. (2019). Crack wave resonances within the basal water layer. *Annals of Glaciology, 60*(79), 158-166.

Gu, B., Nihei, K. T., Myer, L. R., & Pyrak-Nolte, L. J. (1996). Fracture interface waves. *Journal of Geophysical Research: Solid Earth, 101*(B1), 827-835.

Hassan, W., & Nagy, P. B. (1997). On the low-frequency oscillation of a fluid layer between two elastic plates. *The Journal of the Acoustical Society of America, 102*(6), 3343-3348.

Hopkins, D. L., Cook, N. G., & Myer, L. R. (1987). *Fracture stiffness and aperture as a function of applied stress and contact geometry.* Paper presented at the The 28th US Symposium on Rock Mechanics (USRMS).

Jeng, J.-Y., Askari, R., & Chatterjee, S. (2020). Correlation of near surface fractures with seismic radial anisotropy: An approach for near surface fracture identification. *Journal of Applied Geophysics, 173*, 103925.

Korneev, V. (2008). Slow waves in fractures filled with viscous fluid. *Geophysics, 73*(1), N1-N7.

Korneev, V., Danilovskaya, L., Nakagawa, S., & Moridis, G. (2014). Krauklis wave in a trilayer. *Geophysics, 79*(4), L33-L39.

Krauklis, P. (1962). On some low-frequency vibrations of a liquid layer in an elastic medium. *Journal of Applied Mathematics and Mechanics, 26*(6), 1685-1692.

Kumagai, H., & Chouet, B. A. (1999). The complex frequencies of long-period seismic events as probes of fluid composition beneath volcanoes. *Geophysical Journal International, 138*(2), F7-F12.

Kumagai, H., & Chouet, B. A. (2000). Acoustic properties of a crack containing magmatic or hydrothermal fluids. *Journal of Geophysical Research: Solid Earth, 105*(B11), 25493-25512.

Kumagai, H., & Chouet, B. A. (2001). The dependence of acoustic properties of a crack on the resonance mode and geometry. *Geophysical Research Letters, 28*(17), 3325-3328.

Lesage, P., Glangeaud, F., & Mars, J. (2002). Applications of autoregressive models and time–frequency analysis to the study of volcanic tremor and long-period events. *Journal of Volcanology and Geothermal Research, 114*(3-4), 391-417.

Liang, C., O'Reilly, O., Dunham, E. M., & Moos, D. (2017). Hydraulic fracture diagnostics from Krauklis-wave resonance and tube-wave reflections. *Geophysics, 82*(3), D171-D186.

Lipovsky, B. P., & Dunham, E. M. (2015). Vibrational modes of hydraulic fractures: Inference of fracture geometry from resonant frequencies and attenuation. *Journal of Geophysical Research: Solid Earth, 120*(2), 1080-1107.

Lee, Y. Carr, J. Barr, D. & Haas, C. (1990). The fractal dimension as a measure of the roughness of rock discontinuity profiles. *Int J Rock Mech Min Sci Geomech Abstr. 27*, 453-464

Liu, E. (2005). Effects of fracture aperture and roughness on hydraulic and mechanical properties of rocks: implication of seismic characterization of fractured reservoirs. *Journal of Geophysics and Engineering, 2*(1), 38-47.

Lu, Y., Elsworth, D., & Wang, L. (2013). Microcrack-based coupled damage and flow modeling of fracturing evolution in permeable brittle rocks. *Computers and Geotechnics, 49*, 226-244.

Mehrabi, A. R., Rassamdana, H., & Sahimi, M. (1997). Characterization of long-range correlations in complex distributions and profiles. *Physical Review E, 56*(1), 712.

Nakagawa, S., & Korneev, V. A. (2014). Effect of fracture compliance on wave propagation within a fluid-filled fracture. *The Journal of the Acoustical Society of America, 135*(6), 3186-3197.

Nakagawa, S., Nakashima, S., & Korneev, V. A. (2015). Laboratory measurements of guided-wave propagation within a fluid-saturated fracture. *Geophysical Prospecting, 64*(1), 143-156.

Nakano, M., Kumagai, H., Kumazawa, M., Yamaoka, K., & Chouet, B. A. (1998). The excitation and characteristic frequency of the long-period volcanic event: An approach based on an inhomogeneous autoregressive model of a linear dynamic system. *Journal of Geophysical Research: Solid Earth, 103*(B5), 10031-10046.

Paillet, F., & White, J. (1982). Acoustic modes of propagation in the borehole and their relationship to rock properties. *Geophysics, 47*(8), 1215-1228.

Park, C. B., Miller, R. D., & Xia, J. (1998). Imaging dispersion curves of surface waves on multi-channel record. In *SEG Technical Program Expanded Abstracts 1998* (pp. 1377-1380): Society of Exploration Geophysicists.

Petrovitch, C. L., Nolte, D. D., & Pyrak-Nolte, L. J. (2013). Scaling of fluid flow versus fracture stiffness. *Geophysical Research Letters, 40*(10), 2076-2080.

Pyrak-Nolte, L. J., Myer, L. R., & Cook, N. G. (1990). Transmission of seismic waves across single natural fractures. *Journal of Geophysical Research: Solid Earth, 95*(B6), 8617-8638.

Tary, J.-B., Van der Baan, M., & Eaton, D. W. (2014). Interpretation of resonance frequencies recorded during hydraulic fracturing treatments. *Journal of Geophysical Research: Solid Earth, 119*(2), 1295-1315.

Trad, D., Ulrych, T., & Sacchi, M. (2003). Latest views of the sparse Radon transform. *Geophysics, 68*(1), 386-399.

5 Conclusion

In this study we conducted laboratory experiments to investigate the properties of fluid-filled fractures and the Krauklis waves propagate in it. Optical and acoustic experiments are combined to visualize the fluid dynamic with the fluid-filled fractures and analyze the Krauklis wave dispersion, resonance, and attenuation properties qualitatively and quantitatively in fluid fracture under different environments.

Chapter two shows the ability of the dynamic photoelasticity technique to analyze the dispersion of Krauklis waves trapped in fluid-filled fractures based on a pixel-based framework. We performed a series of signal analysis on the waveform extracted from images sequences by tracking the pixel variations induced by the stress wave. The optic experimental dispersion curve calculated using the high-resolution Radon transform is proved to be consistent with the theoretical dispersion equation derived from the plate theory. We also showed the capability of the method to analyze the Krauklis wave in the case of complex geometry with fluid of different viscosity by modeling a saw-tooth fracture. We observe that higher viscous fluid results in a lower Krauklis wave group and phase velocity. In addition, the complex fracture geometry leads to a greater perturbation of the Krauklis wave and a higher velocity compared to the flat fracture.

Apart from the Krauklis wave we visualized and analyzed in the Chapter two, we also visualize the fluid-solid interaction inside fractures with different types of fracture surfaces and tips using a combination of the photoelasticity and shadowgraph technique in chapter 3. The most striking observation is the occurrence of the cavitation and bubble collapse in the fracture with complex surface (saw-tooth shape). The phenomenon is an important mechanism that can contribute to the hydraulic fracture growth and propagation. The two main causes for the fracture surface degradation and growth are, first, the expansion of the bubbles that causes the tensile stress on the fracture wall to increase and, second, the collapse of the bubble generates a shock wave. This phenomenon can be used to explain a variety of geological related fractures growth such as the hydraulic fracturing, deep well waste-water disposal, and dike propagation during magmatic intrusion. In addition, a shadowgraph technique is used to study the effects of bubbles at the fracture tip using various tip geometries. The pressure wave in the liquid phase compresses and pushes forward the trapped bubbles into the tips. The tensile stress induced by the bubbles at the fracture tip increase as the bubble pressure increases. The rate of strain energy release at the fracture tip increases significantly due to the presence of bubbles. The energy produced by the bubbles overcomes the resistance of the trilayer that results in its delamination, which resembles a fracture opening and propagation.

To further understand the Krauklis waves properties and the vibration of the fluid-filled fractures, in addition to the optical experiment, we conducted numerous acoustic experiments to elaborate the study of the effect of the fracture stiffness (Chouet's model, 1988) by changing the fracture thickness, fluid damping, fracture roughness and geometry, and fracture mechanical compliance on the resonant frequencies, quality factor, and dispersion properties. We observe that the phase velocity, resonant frequencies and quality factors: (1) increase with the increase of the fracture thickness; (2) decrease with the increase of the fluid viscosity; (3) decrease with the increase of mechanical compliance. In addition, an increase in the roughness of fracture surface and a change from a rectangular to wedge shaped fracture both result in decreased phase velocity and resonant frequencies. These experimental findings are important to be incorporated into numerical modeling and theoretical derivations.